ALGORITHM DEVELOPMENT
FOR ON-LINE CONTROL OF THE
AIRBORNE LASER

DISSERTATION

Michael W. Oppenheimer, DAGSI

AFIT/DS/ENG/00-02

20010612 121

ALGORITHM DEVELOPMENT FOR ON-LINE
CONTROL OF THE AIRBORNE LASER

DISSERTATION
Michael William Oppenheimer
DAGSI

AFIT/DS/ENG/00-02

.

AFIT/DS/ENG/00-02

ALGORITHM DEVELOPMENT FOR ON-LINE
CONTROL OF THE AIRBORNE LASER

DISSERTATION

Presented to the Faculty

Graduate School of Engineering and Management

Air Force Institute of Technology

Air University

Air Education and Training Command

in Partial Fulfillment of the Requirements for the

Degree of Doctor of Philosophy

Michael William Oppenheimer, B.S., M.S.

DAGSI

September, 2000

ALGORITHM DEVELOPMENT FOR ON-LINE
CONTROL OF THE AIRBORNE LASER

Michael William Oppenheimer, B.S., M.S.

DAGSI
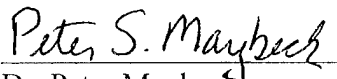
Approved:

_____   _____
Dr. Meir Pachter   Aug 20, 2000
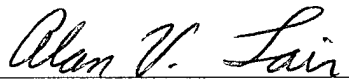Chairman, Advisory Committee   Date

_____   _____
Dr. Peter Maybeck   36 August 2000
Member, Advisory Committee   Date

_____   _____
Dr. Alan Lair   30 Aug 2000
Member, Advisory Committee   Date
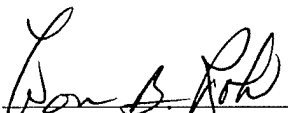
_____   _____
Dr. Won Roh   30 Aug 2000
Dean's Representative   Date

Accepted:

_____
Robert A. Calico, Jr.
Dean, Graduate School of Engineering and Management

Acknowledgments

The most rewarding part of my tenure at AFIT have been the people that have shaped this great experience. Special thanks to Dr. Meir Pachter, my research advisor, for his help and many stimulating conversations over the past few years. Thanks also to Dr. Peter Maybeck and Dr. Alan Lair, my committee members, who provided much of my learning through the rewarding courses that they taught. Every aspect of the AFIT community has been helpful. At AFIT, it truly seems that everyone is there for the benefit of the students. It has been an honor to attend the Air Force Institute of Technology.

On a personal level, I would like to thank my parents for their help and support throughout the years. Mom and dad, I love both of you with all of my heart, thanks for everything. Finally, for the most important person in my life, my wife. Without you, none of this would have been possible. You are my best friend-thanks for always being there for me.

<div align="right">Michael William Oppenheimer</div>

Table of Contents

List of Figures

List of Tables

Table   Page

List of Symbols

Symbol	Page
$n_1(\vec{r}, t)$ = randomly fluctuating index of refraction	17
$\vec{r}$ = three-dimensional position vector	17
$W_{n_1}^K(\kappa, \zeta), W_{n_1}^V(\kappa, \zeta)$ = Kolmogorov and von Karman spectra	17
κ = spatial wavenumber	17
ζ = altitude	17
$\kappa_o = 2\pi / L_o$	18
$C_n^2(\zeta)$ = structure constant of index of refraction fluctuations	18
$\Gamma(\bullet)$ = gamma function	18
L_o = outer scale of turbulence	18
$K(\vec{r})$ = three-dimensional random process	18
$\Gamma_K(\vec{r})$ = autocorrelation of $K(\vec{r})$	19
$\|\bullet\|$ = magnitude of $(\bullet)$	19
$C_n^2(\zeta_i), \zeta_i, \Delta\zeta_i$ = structure constant, altitude, thickness of ith turbulent layer	19
$\vec{x}$ = two-dimensional position vector	20
$\Phi(\vec{x})$ = turbulence induced phase at position $\vec{x}$	20
λ = wavelength	20
$W_\Phi(\kappa)$ = PSD of turbulence induced phase	21
$W_\Phi(\kappa, \zeta_i)$ = PSD of phase in i^{th} layer	21
w_i = layer weights	21
r_o = atmospheric coherence diameter or Fried parameter	21

List of Abbreviations

AFIT/DS/ENG/00-02

Abstract

The use of adaptive optics entails the design of a controller. This requires the development of a model of the plant to be controlled, which, in this case, consists of the atmosphere through which light is traveling. In optics, Zernike polynomials are used as a basis set for the expansion of wavefront phase distortions. Due to the turbulence induced stochastic nature of the underlying process involved, the spatial-temporal correlation functions of the Zernike polynomial phase expansion coefficients must be evaluated if a proper stochastic model of the plant is to be developed and adaptive optics is to be employed. In this work, these correlation functions are developed using a layered atmospheric model which takes into account wind effects and anisoplanatism. Calculations are provided for the first few low-order Zernike modes. Using these correlation functions, an underlying linear, stochastic, dynamical system, which represents the atmosphere and is adequate for control synthesis, is identified. Within an acceptable error bound, the correlation functions of this system are representative of the calculated functions. The deformable mirror is also modeled, output equations are specified, and the complete system is constructed. This system, in turn, provides the basis for the employment of advanced control and estimation concepts. The control objective is to apply the estimated conjugate phase to the deformable mirror so that, at the target, the outbound wavefront distortion is minimized and the Strehl ratio is maximized.

ALGORITHM DEVELOPMENT FOR ON-LINE
CONTROL OF THE AIRBORNE LASER

I. Introduction

1.1 Overview

For years, scientists have been concerned about the effects of atmospheric

turbulence on the propagation of light. Atmospheric turbulence has the effect of

randomly varying the index of refraction of the propagation medium. These fluctuations

cause the familiar "twinkling" of stars and "shimmering of heat" over hot pavement [25].

Due to the randomly varying index of refraction, atmospheric turbulence causes random

wavefront distortion which in turn degrades the performance of optical imaging systems,

below the limit set by diffraction theory. However, it has been shown that real-time

wavefront compensation, commonly called adaptive optics, can improve system

performance [11]. Adaptive Optics (AO) is a broad term used to cover a system which,

in real time, measures the optical aberrations induced in the wavefront over the

propagation path and corrects for their adverse effects.

The root of all evil in the propagation of light in the atmosphere is the existence of

fluctuations in the index of refraction. Index of refraction fluctuations are due to

turbulent air motion which obtains its energy from differential heating and cooling of the

atmosphere. These fluctuations vary both spatially and temporally. Because of this,

when an optical wave propagates through a random medium (like the atmosphere), the

wave undergoes chaotic changes in its phase, amplitude, and other parameters [28].

Stochastic models for turbulence specify second-order statistics, such as the spatial correlation, of the index of refraction fluctuations. Hence, it follows that the turbulence-induced wavefront phase and amplitude deformations can be characterized by their spatial correlation properties. Therefore, the statistical properties of the phase and amplitude fluctuations must be determined.

Adaptive optics is a method of compensating for the random phase and amplitude fluctuations of an optical wave propagating through turbulence. An adaptive optics system consists of three basic components:

1. Wavefront Sensor (WFS) which is a device to measure wavefront deformations.

2. Wavefront modifying device which corrects wavefront deformations, commonly called a Deformable Mirror (DM).

3. Controller which processes measurements and provides commands to the wavefront modifying device.

In general terms, adaptive optics involves the measurement and control of wavefronts in real time in order to deposit light effectively on a detector or target.

In the most basic current application, adaptive optics is used in ground-based imaging systems. In this case, the receiving telescope is fixed on the ground and is directed to an astronomical object. This scenario is depicted in Figure 1.
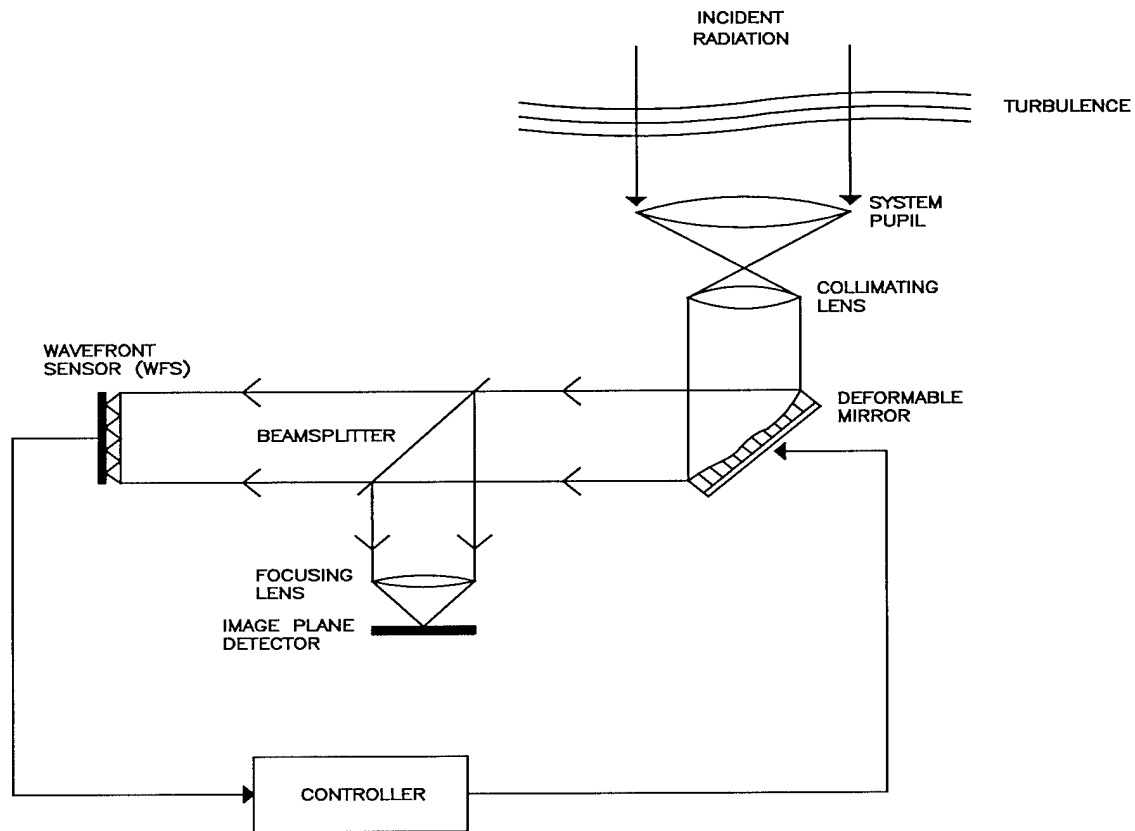
Figure 1: Conventional adaptive optics system used in astronomy.

In Figure 1, the three main components of an adaptive optics system are shown.

Specifically, these are a wavefront modifying device or, in this case, a deformable mirror

(the actuator), a wavefront sensor, and an information processing device (controller). The

WFS accepts light and provides a measurement of the wavefront slope, while the

controller accepts the output of the WFS and converts it to appropriate control signals

sent to the deformable mirror. Indeed, an AO enhanced telescope is a feedback control

system in which the (uncertain) plant is the turbulent atmosphere. Atmospheric

turbulence induces phase shifts in the light's wavefront which are measured by the WFS,

processed by the controller, and corrected by the DM. Hence, the feedback control system is a regulator - the control objective being to drive the atmospheric turbulence-induced phase distortion to zero. In the scenario depicted in Figure 1, the WFS accepts light reflected from the deformable mirror. In this case, the WFS measures the wavefront distortion in the corrected wavefront. Thus, the WFS directly provides a measurement of the error signal, as is required in conventional SISO control systems.

Figure 2 shows a modified adaptive optics system that can be used in astronomy.
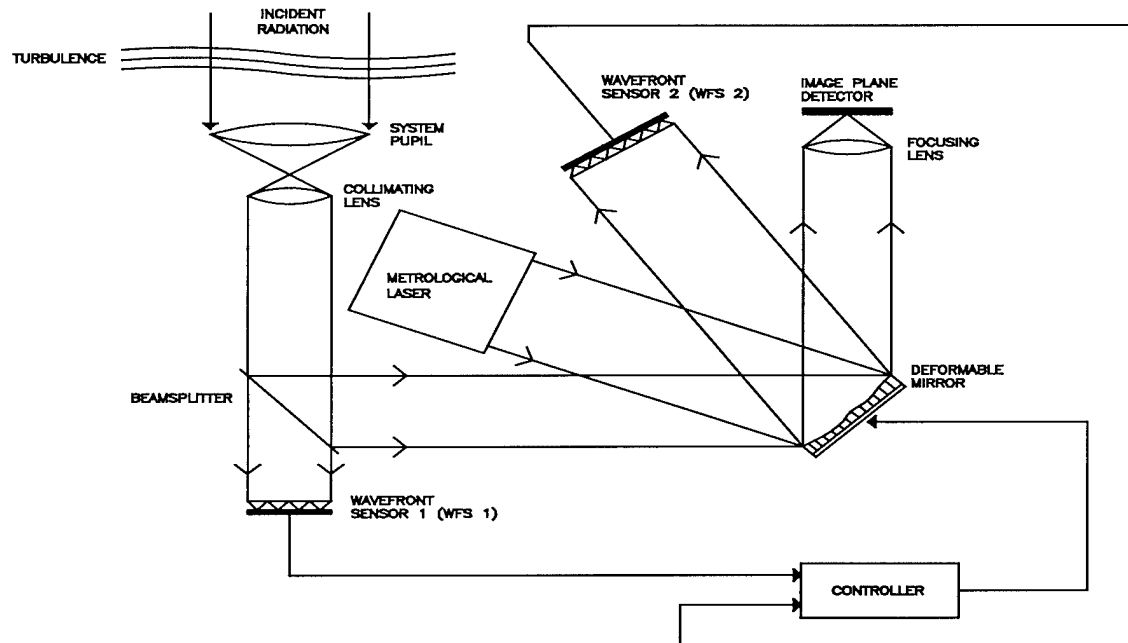
Figure 2: Modified adaptive optics system used in astronomy.

In this case, the WFS measures the distortion in the incident light's wavefront. The incident radiation may be either the object being imaged or a beacon. The beacon is an object, either a natural star or a laser guide star, which provides light to the WFS. Many

times beacons are necessary because the object being imaged does not provide an

adequate amount of light. The metrological laser in Figure 2 is used to provide a minor

feedback loop which is useful when the dynamics of the deformable mirror are not known

precisely. Figures 3 and 4 show the AO control systems for the configurations shown in

Figures 1 and 2.
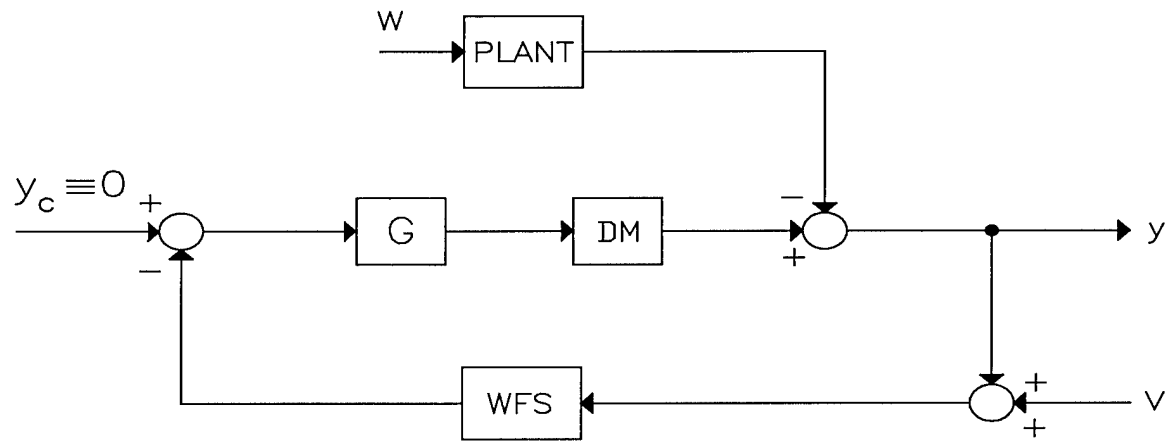
Figure 3. Control system which corresponds to the AO arrangement shown in Figure 1.
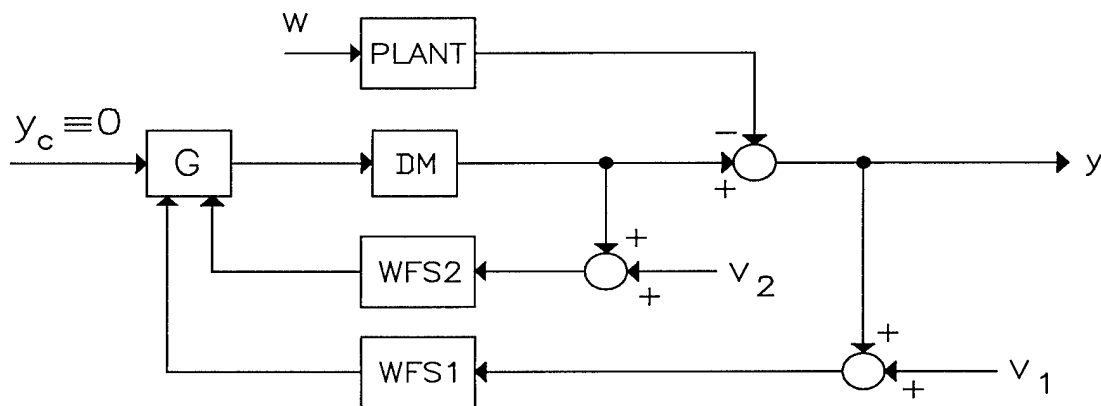
Figure 4. Control system which corresponds to the AO arrangement shown in Figure 2.

In Figures 3 and 4, the controller is denoted by G; the atmospheric model is denoted by PLANT; w denotes white process noise which drives the plant; the phase distortion of the light deposited on the detector is y; and v, v_1, and v_2 are the WFS white noise signals. The subscript 'c' denotes the command signal, which is zero in the regulator control systems used in AO.

If the AO components discussed above worked perfectly, the AO system would achieve ideal performance, namely, the diffraction limit. However, there are numerous factors which degrade the performance of an AO system. The fundamental limiting factors include [23]:

1. Finite light levels in the WFS.

2. Finite degrees of freedom of the DM.

3. Finite spatial sampling of the WFS.

4. Finite temporal response of the AO system.

5. Anisoplanatism.

Until recently, factors (1) - (4) were severe problems. Fortunately, with advances in WFS, DM, and AO hardware design, these degradations play a much smaller role. The same cannot be said for anisoplanatism. Anisoplanatism is a term referring to the object and beacon wavefronts sampling different volumes of the atmosphere. Anisoplanatism results when the object and beacon have a spatial separation. This spatial separation between the beacon, or reference, and object causes the optical paths from the reference and the object to traverse different regions of the atmosphere, resulting in distinct

wavefront perturbations for each wavefront [23]. Figure 5 displays a common

anisoplanatic scenario.

BEACON   OBJECT

TURBULENCE

RAY PATHS

APERTURE
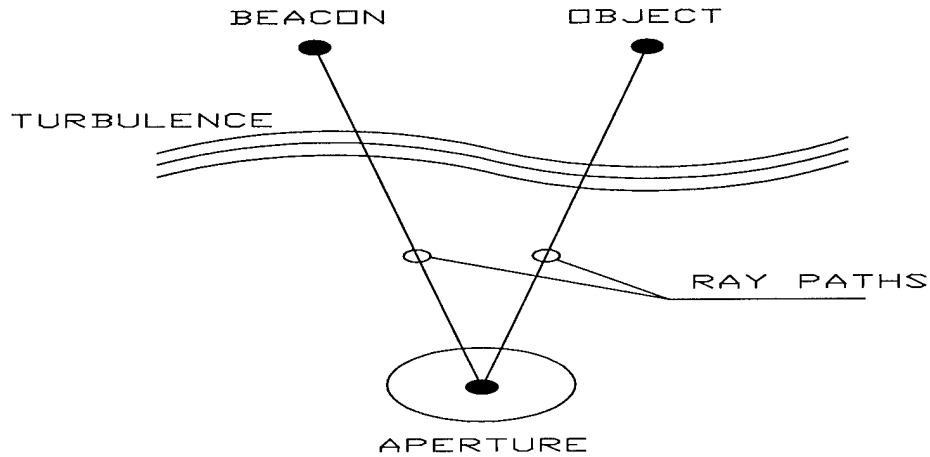
Figure 5: Anisoplanatism.

However, just because a spatial separation exists between the reference and object

does not mean that anisoplanatic effects are observed. In fact, the two objects may lie

within the isoplanatic angle, defined as the maximum angular separation for which the

turbulence-induced wavefront deformations for the object and beacon wavefronts are still

essentially the same. In the visible spectrum, the object being imaged must be within 5 to

10 μrad of the beacon [23]. At infrared wavelengths, the isoplanatic angle is significantly

larger, on the order of 100's of μrad.

1.2 AirBorne Laser

The AirBorne Laser (ABL) is an atmospherically based directed energy weapon system currently being developed by the United States Air Force. This program uses a high-energy laser, mounted in an airplane, to deposit energy on and disable a theater ballistic missile in boost phase. The ABL scenario is significantly different from typical optical imaging systems. First, the ABL operates at an altitude of about 40,000 ft. Unlike ground-based imaging systems, in which the wavefronts propagate perpendicularly to the earth's surface, the propagation paths of the beacon and High-Energy Laser (HEL) are approximately horizontal to the earth's surface. Second, there is an enormous amount of motion in this problem. Both the aperture (mounted in the airplane) and target are moving at large velocities. Hence, unlike conventional imaging systems in which the wind introduces a temporal dependence in the index of refraction fluctuations, dynamic aperture and target motion account for the majority of temporal effects.

The arrangements shown in Figures 1 and 2 do not allow for anisoplanatism and do not account for time delays inherent in the control system. For use in the ABL, the adaptive optics configurations shown in Figures 1 and 2 must be modified. Figure 6 shows the ABL's adaptive optics arrangement. In this situation, there are two wavefronts of interest. First is the beacon, incident, or inbound, radiation. The beacon wavefront is a spherical wavefront emanating from the sharp tip of the missile - or a fixed anchor point. This is unlike the astronomical case in which radiation from the laser guide star beacon is
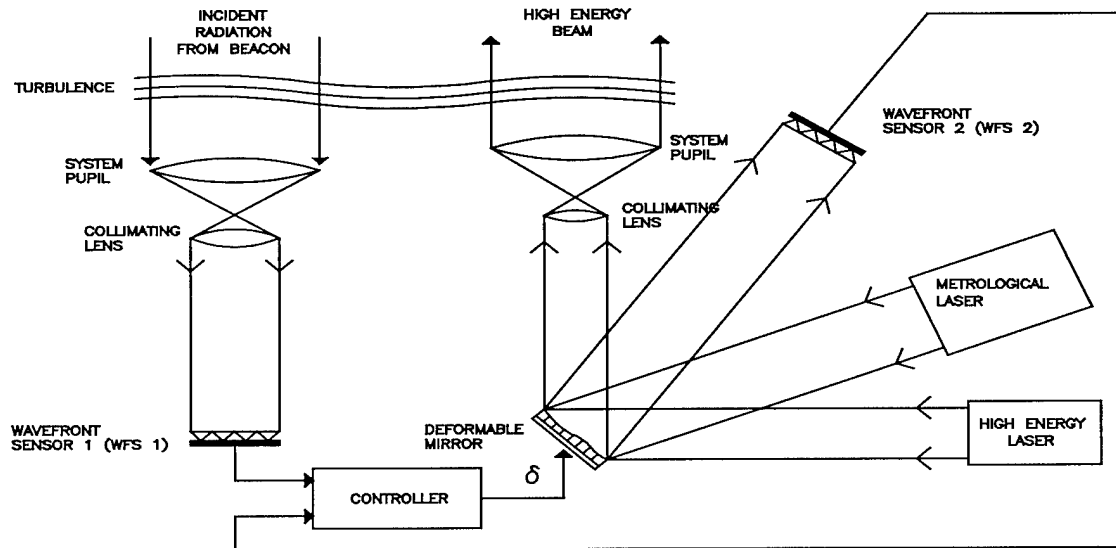
Figure 6: ABL adaptive optics system.

scattered from the layer in the ionosphere. Hence, in astronomy, the beacon is subject to

constant turbulence-induced fluctuations due to the upward passage of the beacon's laser

beam through the turbulent atmosphere. This does not allow for tilt estimation (and

correction) in the astronomical application of straight-forward AO. This is not so in the

ABL case in which the target's tip is flooded by laser illumination and most of the

radiation is reflected off the fixed tip of the missile. The beacon wavefront is the same as

the ones displayed in Figures 1 and 2. Second is the high-energy beam which is used to

deposit the corrected, or controlled, high-energy laser on the target. As in Figure 2, the

metrological laser is used to provide a minor feedback loop if the mirror dynamics are not

known precisely.

Atmospheric turbulence will induce random temporal variations in the laser

beam's wavefront which, in turn, will reduce the light intensity at the target and hence the

directed energy weapon's effectiveness. This fact provides the motivation for the employment of AO in order to correct for the deleterious effects caused by atmospheric turbulence.

In order to apply AO to the AirBorne Laser (ABL), a model of the plant to be controlled must be developed. The plant, in this case, is the turbulent atmosphere through which light is traveling. Because of atmospheric turbulence, the plant, which models the atmosphere, will be stochastic.

1.3 Historical Overview

Pioneering work in optical wave propagation through atmospheric turbulence was performed in the 1950's by Tatarski [27]. In his work, Tatarski considered the medium between the source and aperture as a continuum. However, the most common forms of the Power Spectral Density (PSD) of the index of refraction fluctuations contain singularities at the origin. Thus, evaluation of the necessary integrals requires special care. In the simple astronomical scenario considered by Tatarski, integrations in the z-direction, i.e., the direction of wavefront propagation, could be performed in closed-form. In the process, the singularity in the PSD of the index of refraction fluctuations did not pose any difficulty; however, no such analytical techniques present themselves in the more dynamic ABL scenario. A layered (discrete) atmospheric model can be used to avoid integration in the direction of wavefront propagation. In this model, the atmosphere is assumed to be composed of a finite number of properly separated layers so that the spatial correlation can be described as the sum of the contributions from all

layers. Hence, the layered atmospheric model requires simpler, two-dimensional integrations as opposed to the three-dimensional integrations in Tatarski's original work. Other seminal work in optical propagation through atmospheric turbulence is due to Kolmogorov [14] and Fried [4, 5]. Kolmogorov developed a statistical model for the structure of turbulent air flows. His model is widely used as the spatial PSD of the index of refraction fluctuations. Fried has extended the results of Tatarski and also developed the seeing cell size, commonly called the Fried parameter, r_0. The seeing cell size is interpreted as the aperture size beyond which further increases in diameter result in no further increases in resolution.

Zernike polynomials have been extensively used for analysis in optical systems [6, 12, 18]. These orthonormal polynomials, which are defined within a circle of unit radius, form a complete set and represent many specific phase aberrations [23]. Due to the fact that the ABL application requires the consideration of two distinct wavefronts at two different time instants, the spatial-temporal correlation of the Zernike polynomials' phase expansion coefficients of the wavefronts of interest is required. For implementation in adaptive optics systems, some partial results for these correlation functions have been provided by Takato and Yamaguchi [26], Valley and Wandzura [30], Whiteley, et. al [35], and Whiteley [36].

1.4 Problem Statement

The application of AO to the ABL is a vast problem. In no way could one dissertation attempt to tackle the entire problem. Therefore, a viable, but challenging problem statement for this dissertation is as follows:

> The objectives are to develop fully a unified approach to beam control for the ABL so that advanced control techniques can be applied, and to quantify the performance improvements that can be achieved by utilizing these techniques.

To this end, a generic ABL engagement geometry is selected as the basis for this problem. Simplifications can be made to transform this work into special cases which are applicable to imaging and laser communications. For this general geometry, the performance degradation due to turbulence-induced optical aberrations is investigated and the associated optimal estimation and control theory is developed. The results obtained in this research are for a layered, homogeneous, isotropic, wide-sense stationary turbulence model. For a homogeneous, isotropic random process, the autocorrelation function of $X(\bar{r})$, denoted $\Gamma_X(\bar{r})$, is a function only of the scalar distance $r = |\bar{r}|$. Tilt compensation is the main concern in this problem, with model inadequacies and time delays also included. The control objective is to provide commands to the DM so that the estimated conjugate phase can be applied to the mirror such that, at the target, the high-energy laser's wavefront distortion is minimized and the Strehl ratio is maximized. In this way, the HEL is correctly pointed to the aim point. The Strehl ratio is a performance metric defined as the irradiance with wavefront aberrations present divided by the diffraction-limited irradiance on the optical axis. A perfect Strehl ratio is one, while typical imaging systems have Strehl ratios well below the theoretical limit; however, an exact number is

difficult to present because many factors contribute to the Strehl ratio. A good Strehl ratio would be 0.6 or higher.

1.5 Key Results

The analysis conducted in this research has led to the following key results:

- A unified framework for the application of adaptive optics to the ABL.

- A fully developed engagement geometry for the ABL encompassing target and aperture motion as well as wind effects.

- A modified Frozen Flow Hypothesis (FFH) which takes into account translation and rotation of the aperture and target.

- A new approach to developing an atmospheric model which directly uses correlation kernel data instead of designing shaping filters for the atmospheric states. This results in a lower-order, and therefore, more practical atmospheric model.

- Development of an atmospheric model that provides a good representation of the atmosphere. This is validated by examining the robustness of the Kalman filter based upon that model.

- A complete AO control system which accounts for anisoplanatism and time delays.

- Significant improvement in the reduction of wavefront phase deformations that can be obtained by simply performing tilt correction. This result is displayed using simulations of the entire ABL AO control system.

- Strehl ratios that are improved by about 0.15 using tilt compensation as compared to the no compensation case. In terms of simple conjugation, Strehl ratios are improved by about 0.04.

1.6 Organization

Due to the atmospheric turbulence-induced stochastic nature of the underlying processes involved, the spatial-temporal correlation functions of the Zernike polynomial phase expansion coefficients must be evaluated if a proper stochastic model of the plant is to be developed and adaptive optics is to be employed. In this research, these correlation functions are developed using a layered atmospheric model, and calculations for the first few low-order Zernike modes are performed. The spatial-temporal correlation of the Zernike phase expansion coefficients is developed for a generic adaptive optics configuration. In fact, the general situation, as it applies to the ABL scenario, is considered. Specifically, two separate wavefronts at two distinct time instants are considered. With the dynamic scenario in mind, a novel modified frozen flow hypothesis which accounts for translation as well as rotation of the aperture and target is also developed.

The use of AO entails the design of a controller. This requires the development of a model of the plant to be controlled. In AO, the plant consists of the atmosphere through which light is traveling. Moreover, a distinct feature of the AO control application is the presence of random signals in the plant. Thus, in order to apply control concepts to the ABL scenario and realize the benefits of AO, an underlying linear, stochastic, dynamical

14

system model which generates the correlation functions of the Zernike expansion coefficients and is adequate for control synthesis must be developed. This work addresses the attendant realization problem. Using the calculated correlation functions, an atmospheric model (plant) is constructed. This model will then serve in a Kalman filter-based optimal stochastic controller (Linear Quadratic Gaussian controller) mechanization of an adaptive optics control system for the ABL. In the ABL paradigm, the deformable mirror is the actuator element for the control system. Thus, a model of the DM compatible with the modal approach is developed. An equivalent discrete-time model of the realized continuous-time system is constructed and the complete adaptive optics control system is discussed and simulated.

This dissertation is organized as follows. Atmospheric models and Zernike polynomials are discussed in Chapter 2. In Chapter 3, the ABL-specific engagement scenario is introduced, including all of the necessary geometrical relations. Next, the attendant auto- and cross-correlations of the atmosphere's Zernike polynomial phase expansion coefficients are derived in Chapter 4. Also, the correlation functions are calculated and a linear, stochastic, dynamical system is synthesized using the developed correlation functions. Chapter 5 contains a description of the modeling of the deformable mirror dynamics, using a modal approach. The complete system model as well as the equivalent discrete-time system are also discussed in Chapter 5. Chapter 6 describes the Kalman filter and Linear Quadratic Gaussian (LQG) controller design while Chapter 7 provides results of the control system simulation as well as a discussion of these results. Last, appendices, a succinct list of relevant references, and a vita are provided.

1.7 Summary

In this chapter, the compensation of atmospheric turbulence using adaptive optics has been introduced. The main components of an AO system as well as some common AO configurations have also been considered. Some of the most prevalent performance degrading factors, with emphasis on anisoplanatism, have also been discussed. To achieve the goal of successfully applying AO to the ABL, a general engagement geometry must be considered. This allows development of the correlation between the inbound (beacon) and outbound (HEL) wavefronts. Advanced control concepts can then be used to compensate for optical wavefront aberrations.

In the next chapter, second-order statistics of the index of refraction fluctuations will be discussed. In particular, the two most common spectral representations of the fluctuations, namely, the Kolmogorov and von Karman spectra, will be delineated. The layered atmospheric model and Zernike polynomials will also be covered.

II. Atmospheric Models and Zernike Polynomials

2.1 Introduction

Atmospheric models and Zernike polynomials will be discussed in the upcoming sections. In order to describe the atmosphere mathematically, the physical nature of turbulence must be understood. In particular, index of refraction fluctuations, the Kolmogorov spectrum, and the von Karman spectrum will be covered. Also, the layered atmospheric model will be examined. Following this, a description of Zernike polynomials and their application to optics will be included.

2.2 Index of Refraction Fluctuations

Index of refraction fluctuations arise from turbulent air motion which obtains its energy from differential heating and cooling of the atmosphere. Turbulent eddies are pockets of air which have a uniform index of refraction. The statistical description of the number and size of these eddies is given by the Power Spectral Density (PSD) of the randomly fluctuating index of refraction term, $n_1(\bar{r}, t)$, where $\bar{r}$ is a three-dimensional position vector and t is time. Denoting this PSD by $W_{n_1}(\kappa, \zeta)$ (explicitly a function of spatial wavenumber κ and altitude ζ), two widely used forms can be delineated, namely, the Kolmogorov and von Karman spectra [13]:

$$W_{n_1}^K(\kappa, \zeta) = \frac{\sqrt{3} \ \Gamma\left(\frac{8}{3}\right)}{2(2\pi)^{8/3}} C_n^2(\zeta) \kappa^{\frac{-11}{3}} \qquad (1)$$

17

and

$$W_{n_1}^V(\kappa,\zeta) = \frac{\sqrt{3}\ \Gamma\!\left(\dfrac{8}{3}\right)}{2(2\pi)^{8/3}} \frac{C_n^2(\zeta)}{\left(\kappa^2 + \kappa_o^2\right)^{11/6}} \tag{2}$$

where $\kappa_o = 2\pi\,/\,L_o$, L_o is the outer scale of turbulence, $C_n^2(\zeta)$ is structure constant of the

index of refraction fluctuations, $\Gamma(\bullet)$ is the gamma function, and the superscripts 'K' and

'V' represent the Kolmogorov and von Karman spectra, respectively. $C_n^2(\zeta)$ can be

thought of as a term which characterizes the strength of the index of refraction

fluctuations. Many $C_n^2(\zeta)$ profiles exist, for example, the SLC-Day, Hufnagel-Valley,

and Greenwood models [10, 21]. The L_o term represents the characteristic dimension of

the largest turbulent eddies which break up following Kolmogorov theory. The von

Karman spectrum will be used extensively in the upcoming work because it does not

contain the non-integrable pole at $\kappa = 0$ which is present in the Kolmogorov spectrum.

Thus far, only the spectral characteristics of the index of refraction fluctuations

have been considered. These spectral representations have corresponding spatial

representations, with the two being related through the Fourier transform. As already

stated, the second-order statistics of the Zernike polynomial phase expansion coefficients

are of interest. However, to obtain this expression requires evaluation of the second-

order statistics of the index of refraction fluctuations. In order to examine this, two

definitions related to three-dimensional random processes will be required. First, let $K(\bar{r})$

be a three-dimensional random process where $\bar{r}$ is a position vector. The process $K(\bar{r})$ is

said to be homogeneous if the autocorrelation of $K(\bar{r})$,

$$\Gamma_K(\vec{r}_1, \vec{r}_2) = E\{K(\vec{r}_1)K(\vec{r}_2)\}, \qquad (3)$$

where $E\{\bullet\}$ denotes the expectation operator, is a function only of the difference $\vec{r}_1 - \vec{r}_2$.

Second, a random process is isotropic if its autocorrelation function is spherically

symmetric. In other words, for a homogeneous, isotropic random process, the

autocorrelation function, $\Gamma_K(\vec{r})$, is a function only of the scalar distance $r = |\vec{r}|$, where $|\bullet|$

denotes the magnitude of the corresponding vector. In all cases, the index of refraction

fluctuations in the atmosphere are assumed to be homogeneous and isotropic.

2.3 Layered Atmospheric Model

In this model, the atmosphere is assumed to be composed of a finite number of

properly separated layers. The term properly refers to the layers being treated as

independent. A more thorough discussion of independent layers is presented later in this

section. Basically, the layered model can be thought of as the discrete counterpart to the

continuous model. Hence, integrations along the propagation path (z-direction) in the

continuous model are replaced by summations in the discrete model. Therefore, the

desired spatial correlation between wavefronts can be described as the sum of the

contributions from all layers. This layering of the turbulence significantly simplifies the

calculations to follow.

For a layered model, the $C_n^2(\zeta)$ profile is broken up into a finite number of slabs,

with each slab characterized by a turbulence strength which is nearly constant in each

layer. Letting $C_n^2(\zeta_i)$, ζ_i, and $\Delta\zeta_i$ be the structure constant, altitude, and thickness of the

i^{th} turbulent layer, the structure constant and altitude are selected in such a way that the

zeroth through seventh moments, ξ, of the continuous model match the discrete model [23]:

$$\int_0^L \zeta^\xi C_n^2(\zeta)d\zeta = \sum_i \zeta_i^\xi C_n^2(\zeta_i)\Delta\zeta_i \ . \tag{4}$$

In eq. (4), L is the propagation path length and $0 \le \xi \le 7$. Moments zero through seven are used to provide enough fidelity in the layered model. Higher order moments could be used, but the rate of return is negligible. The weights and heights of the most common four-layer models have been calculated by Troxel, et. al. [29]. Also, it should be mentioned that $\Delta\zeta_i$ surrounds ζ_i symmetrically.

If diffraction effects are assumed to be negligible, then the turbulence-induced phase at position $\bar{x}$ can be written as

$$\Phi(\bar{x}) = \int_0^L \left(\frac{2\pi}{\lambda}\right) n_i(\bar{x},z)dz \tag{5}$$

where λ is the wavelength. Equation (5) displays the computation of wavefront phase when the atmosphere is considered a continuum. Since $\Phi(\bar{x})$ is the sum of a large number of zero-mean random variables, namely $n_1(\bar{x},z)$, then, by the Central Limit Theorem [3], $\Phi(\bar{x})$ will be zero-mean and Gaussian.

For a layered atmospheric model, the expression analogous to eq. (5) is

$$\Phi(\bar{x}) = \frac{2\pi}{\lambda} \sum_i \Delta\zeta_i n_1(\bar{x},\zeta_i) \ . \tag{6}$$

By the Fourier transform relation between the PSD and autocorrelation, the PSD of the turbulence-induced phase is

$$W_\Phi(\kappa) = FT\left[E\left\{\Phi(\bar{x})\Phi(\bar{x}+\Delta\bar{x})\right\}\right]$$

$$= \sum_i \Delta\zeta_i\left(\frac{2\pi}{\lambda}\right)\sum_{i'} \Delta\zeta_{i'}\left(\frac{2\pi}{\lambda}\right)FT\left[E\left\{n_1(\bar{x},\zeta_i)n_1(\bar{x}+\Delta\bar{x},\zeta_{i'})\right\}\right]$$

$$= \sum_i \Delta\zeta_i\left(\frac{2\pi}{\lambda}\right)^2 W_{n_1}(\kappa,\zeta_i) \tag{7}$$

where FT{$\bullet$} denotes the Fourier transform. The term in the summation is the PSD of the

phase in the ith layer, denoted $W_\Phi(\kappa,\zeta_i)$. Thus,

$$W_\Phi(\kappa) = \sum_i W_\Phi(\kappa,\zeta_i). \tag{8}$$

Substituting eq. (2) into eq. (7) yields the von Karman spectrum for the phase in the ith

layer:

$$W_\Phi^V(\kappa,\zeta_i) = \frac{\sqrt{3}\ \Gamma\left(\frac{8}{3}\right)}{2(2\pi)^{8/3}}\left(\frac{2\pi}{\lambda}\right)^2 \Delta\zeta_i\ \frac{C_n^2(\zeta_i)}{\left(\kappa^2+\kappa_o^2\right)^{11/6}}. \tag{9}$$

For $\xi = 0$, eq. (4) implies that

$$\sum_i \frac{\Delta\zeta_i C_n^2(\zeta_i)}{\displaystyle\int_0^L C_n^2(\zeta)d\zeta} = 1. \tag{10}$$

The term in eq. (10) can be identified as a turbulence-dependent layer weight w_i:

$$w_i = \frac{\Delta\zeta_i C_n^2(\zeta_i)}{\displaystyle\int_o^L C_n^2(\zeta)d\zeta}. \tag{11}$$

Defining the atmospheric coherence diameter, or Fried parameter [4], r_o, as

$$r_o = \left[\frac{2.91}{6.88}\left(\frac{2\pi}{\lambda}\right)^2 \int_0^L C_n^2(\zeta)d\zeta\right]^{-3/5}, \qquad (12)$$

and using this result and eq. (11) in eq. (9) gives

$$W_\Phi^V(\kappa,\zeta_i) = \frac{\sqrt{3}\,\Gamma\!\left(\frac{8}{3}\right)}{2(2\pi)^{8/3}}\left(\frac{6.88}{2.91}\right) w_i r_o^{-5/3}\left(\kappa^2 + \kappa_o^2\right)^{-11/6}. \qquad (13)$$

Equation (13) provides the final form of the von Karman spectrum and will be used in subsequent calculations.

When using a layered atmospheric model, the problem of calculating the correlation properties of the field perturbations reduces to calculating those for a single layer and then extending the results to account for all layers. Tatarski [27], Goodman [8], and Troxel, et. al. [29] have argued that the layers can be treated as approximately independent if the separation of layer centers is greater than the largest distance between field points in the pupil [23]. This allows the spatial correlation of phase perturbations to be calculated for each layer separately, with the results being added to account for propagation through the entire turbulent region. The independence condition will be satisfied by choosing the locations of the turbulent layers such that the separation of layer centers is greater than the largest distance between field points in the pupil, i.e., the aperture diameter in this case.

The results in this dissertation are derived using geometrical optics which is equivalent to assuming that near field conditions exist. Near field conditions exist if the total thickness of the turbulent region satisfies [37]

$$\sum_{n=1}^{N} \Delta \zeta_i \leq \frac{\left| \Delta \vec{x}_{max} \right|}{\lambda \pi} \qquad (14)$$

where N is the number of layers, λ is the wavelength, and $\Delta \vec{x}_{max}$ is the maximum

separation in the aperture. When near field conditions exist, the turbulence region is

close enough to the aperture plane that refraction caused by index of refraction variations

can be neglected [23]. This allows the correlation between the inbound and outbound

wavefronts to be derived based on straight ray path calculations. As the turbulent region

extends outward from the aperture plane, refraction cannot be ignored. In this case, the

propagation paths cross and interfere with each other, which in turn causes amplitude

perturbations. This scenario is referred to as far field turbulence. In the case of near field

conditions, the perturbations in the aperture plane are entirely phase perturbations. Near

field conditions will exist in the ABL scenario, which implies that only phase

perturbations will be investigated.

2.4 Zernike Polynomials

Zernike polynomials, denoted by $Z_i(\vec{x})$, are a complete set of orthonormal

polynomials defined within a circle of unit radius. They are commonly used in optics

because they represent many specific phase aberrations [1]. In the study of optics, it is

necessary to have some means to express the phase distortion in a wavefront.

Considering a circular aperture with an incident wavefront propagating through

turbulence, the absolute phase, $\Phi(\tilde{x}, \tilde{y}, t)$, of the wave within the aperture is a function of

time and the spatial coordinates within the aperture. Here, $\tilde{x}$ and $\tilde{y}$ are normalized x-

and y-coordinates, for describing the plane of the aperture, such that

$0 \leq |\tilde{x}| \leq 1, 0 \leq |\tilde{y}| \leq 1$. Because Zernike polynomials are orthonormal only on a unit

circle, the aperture's radius must be normalized to apply Zernikes to non-unit radius

apertures. The appropriate transformation is

$$x = \frac{\tilde{x}}{R} \ , \ y = \frac{\tilde{y}}{R} \tag{15}$$

where R is the radius of the aperture.

Since Zernike functions are a complete set which span the functional space

containing $\Phi(\tilde{x}, \tilde{y}, t)$, the phase can be written as a linear combination of Zernikes, that

is,

$$\Phi(\tilde{x}, \tilde{y}, t) = \Phi(Rx, Ry, t) = \sum_{i} a_i(t) Z_i(x, y) \tag{16}$$

where $a_i(t)$ are the Zernike polynomial phase expansion coefficients. Letting (Rx, Ry) =

$R\vec{x}$ and (x, y) = $\vec{x}$, eq. (16) can be equivalently written as

$$\Phi(R\vec{x}, t) = \sum_{i} a_i(t) Z_i(\vec{x}) \ . \tag{17}$$

Other basis functions exist, for example, Legendre [24] and Karhunen-Loeve [18,

34]. The decision to use Zernike polynomials in this work is due simply to personal

preference. Zernike polynomials are suitable to optics problems since they represent

many specific phase aberrations such as tilt, coma, astigmatism, etc. Hence, they provide

a physical understanding of the turbulence-corrupted wavefront. The drawback of

Zernikes is that all of the modes are not uncorrelated with each other. Karhunen-Loeve

basis functions are simply linear combinations of Zernike functions and are uncorrelated

[23]. However, since they are linear combinations of Zernikes, the physical

understanding of wavefront distortion is lost. Hence, the decision was made to use the more common and physically practical Zernike polynomials.

The expansion coefficients in eqs. (16) and (17) can be obtained by projecting the wavefront phase onto the space of Zernike polynomials, that is,

$$a_i(t) = \int \Phi(R\vec{x}, t) Z_i(\vec{x}) W(\vec{x}) d\vec{x} \tag{18}$$

where $W(\vec{x})$ is a weighting function defined as

$$W(\vec{x}) = \begin{cases} 1/\pi & \text{if} \quad |\vec{x}| \leq 1 \\ 0 & \text{otherwise} \end{cases} \tag{19}$$

and the integration is over the entire two-dimensional plane. Also, Zernike polynomials form an orthonormal basis set which satisfies

$$\int W(\vec{x}) Z_i(\vec{x}) Z_j(\vec{x}) d\vec{x} = \delta_{ij} \tag{20}$$

where δ_{ij} is the Kronecker delta defined by

$$\delta_{ij} = \begin{cases} 1 & \text{if} \quad i = j \\ 0 & \text{if} \quad i \neq j. \end{cases} \tag{21}$$

Table 1 lists some low-order Zernike polynomials, $Z_i(r,\theta)$ in polar coordinates, $Z_i(x,y)$ in rectangular coordinates, their corresponding radial and azimuthal orders [18], n and m, and the optical aberrations they represent [1].

Zernike # i	n	m	$Z_i(r,\theta)$	$Z_i(x,y)$	Aberration
1	0	0	1	1	Piston
2	1	1	$\dfrac{2r\cos\theta}{R}$	$\dfrac{2x}{R}$	X-tilt
3	1	1	$\dfrac{2r\sin\theta}{R}$	$\dfrac{2y}{R}$	Y-tilt
4	2	0	$\sqrt{3}\left[2\left(\dfrac{r}{R}\right)^2-1\right]$	$\dfrac{\sqrt{3}}{R^2}\left(2x^2+2y^2-R^2\right)$	Focus
5	2	2	$\sqrt{6}\left(\dfrac{r}{R}\right)^2\sin(2\theta)$	$\dfrac{2\sqrt{6}}{R^2}(xy)$	Astigmatism
6	2	2	$\sqrt{6}\left(\dfrac{r}{R}\right)^2\cos(2\theta)$	$\dfrac{\sqrt{6}}{R^2}\left(x^2-y^2\right)$	Astigmatism
7	3	1	$\sqrt{8}\left[3\left(\dfrac{r}{R}\right)^3-2\left(\dfrac{r}{R}\right)\right]\sin(\theta)$	$\dfrac{\sqrt{8}}{R^3}\left(3x^2+3y^2-2R^2\right)y$	Coma
8	3	1	$\sqrt{8}\left[3\left(\dfrac{r}{R}\right)^3-2\left(\dfrac{r}{R}\right)\right]\cos(\theta)$	$\dfrac{\sqrt{8}}{R^3}\left(3x^2+3y^2-2R^2\right)x$	Coma

Table 1. Zernike polynomials.

2.5 Summary

In this chapter, index of refraction fluctuations and the Kolmogorov and von Karman spectra were discussed. The layered atmospheric model was introduced and the turbulence-induced phase, using this model, was delineated. Zernike polynomials and their application to optics were also covered.

In Chapter 3, the ABL engagement geometry will be introduced. The objective is to determine the projections of the aperture vectors into the turbulent layers. These projections are necessary since the only contributions to the correlation between

wavefronts are due to the turbulent slabs. Once the projections have been determined, the separation between the projected vectors can be evaluated. The effect of wind is also taken into account and the necessary kinematic variables are delineated.

III. ABL Engagement Geometry

3.1 Introduction

The engagement geometry for the ABL is introduced in this chapter. Due to the dynamic nature of the ABL engagement scenario, the geometry has been chosen to be as general as possible. Two times instants of interest, t_1 and t_2, are considered and both aperture and source motion as well as wind effects are included. In conventional AO, the latter is responsible for introducing a temporal dependence in the index of refraction fluctuations. In the ABL application, dynamic object and source motion cause the major temporal dependence. Since the object and source velocities are much greater than the wind velocity, the wind has a diminished effect in this application. However, wind is also included so that the general results derived in this work can be specialized to classical AO situations such as fixed target or source and fixed target and source. Also, a layered atmospheric turbulence model is used with a wind vector of general direction. In using a layered atmospheric model, it is necessary to project the aperture vectors into the turbulent layers.

In the ABL, there are two wavefronts of interest, namely, the inbound (beacon) and outbound (HEL) wavefronts. Currently, for the ABL, the inbound wavefront's wavelength is 1.03 μm while the wavelength of the outbound wavefront is 1.05 μm. Therefore, in the simulations in this work, it will be assumed that the beacon's wavelength is 1.03 μm and the HEL's wavelength is 1.05 μm.

28

It is desired to determine the correlation between these two wavefronts. This is needed since measurements come from the inbound propagation path; that is, only the turbulence-induced wavefront deformations of the inbound wavefront are measured. In order to fire the HEL successfully, the effects of turbulence on the propagation of the outbound wavefront must be determined. A method of achieving this result is to evaluate the correlation between the inbound and outbound wavefronts. Since a layered atmospheric model has been selected, the spatial separation between inbound and outbound wavefront points, in the turbulent layer, is needed. Thus, the objective in this section is to develop an expression for the separation of projected aperture vectors. However, to obtain this quantity it will be necessary to project the aperture vectors, perform transformations between reference frames, determine the time t_2 kinematic variables in terms of their time t_1 counterparts, and include the wind effect. In this process, a novel frozen flow hypothesis needs to be developed.

3.2 ABL Engagement

Consider the simplified ABL engagement geometry depicted in Figure 7. This figure displays the aperture and target at two time instants of interest, t_1 and t_2, where $t_2 > t_1$. Aperture and target motion are considered with corresponding constant velocity vectors $\vec{V}_A$ and $\vec{V}_T$, respectively. Constant velocity vectors have been assumed since the sample period, $\Delta t = t_2 - t_1$, will be small (on the order of tenths of milliseconds).
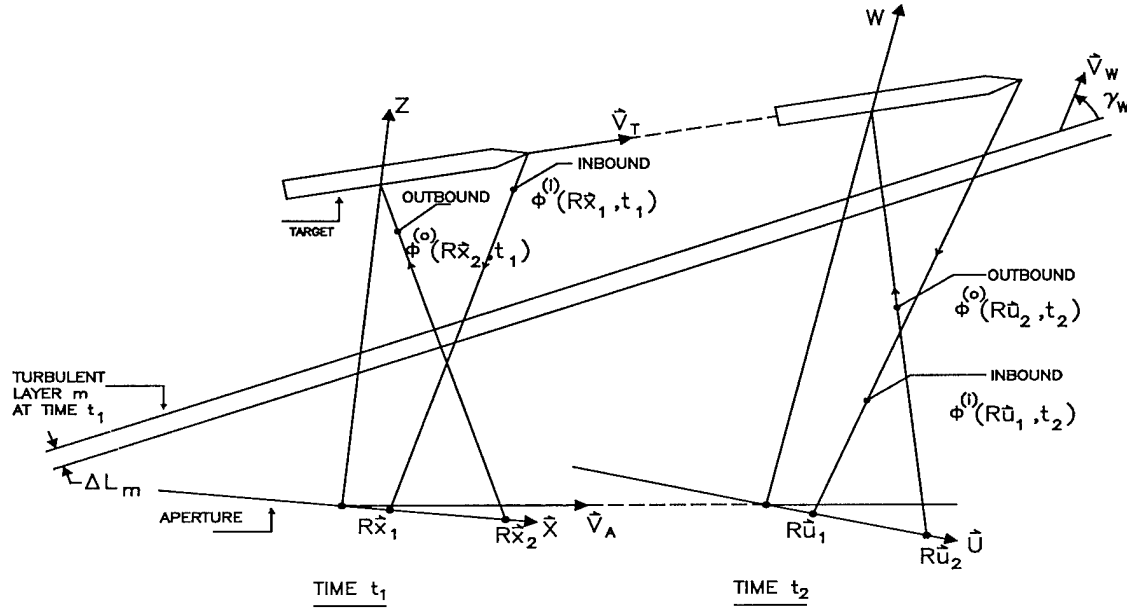
Figure 7. Simplified ABL engagement geometry.

Two wavefronts are depicted, namely, the inbound (beacon) and outbound (HEL). Measurements for the ABL come from the inbound wavefront, that is, the tip of the missile is flooded with a laser and the returned light is sampled by a WFS to determine the amount of distortion in the inbound wavefront's phase. The HEL is pointed to the aim point, or that point where the beam will be directed to disable the target. It can be seen that there is a spatial separation between the inbound and outbound wavefronts, resulting in some degree of anisoplanatism. Due to the fact that there are two wavefronts, two aperture locations at each time instant are denoted, namely, $R\bar{x}_i$ and $R\bar{u}_i$, $i = 1, 2$. Also, it is assumed that the aperture accurately tracks the target at all times.

The layered atmospheric model is depicted by displaying turbulent layer m with thickness ΔL_m. The wind has the effect of shifting the turbulent layer; therefore, turbulent layer m is moved by wind vector $\bar{V}_w$. There are two reference frames included in this

figure, the first being $(\bar{X}, Z)$, which is coincident with the aperture at time t_1 and has the Z-axis normal to the aperture. Likewise, frame $(\bar{U}, W)$ is coincident with the aperture at time t_2 and the W-axis is normal to the aperture.

Figure 7 was shown here simply to display an uncluttered drawing. Figure 8 shows the full ABL engagement geometry first introduced in [19].
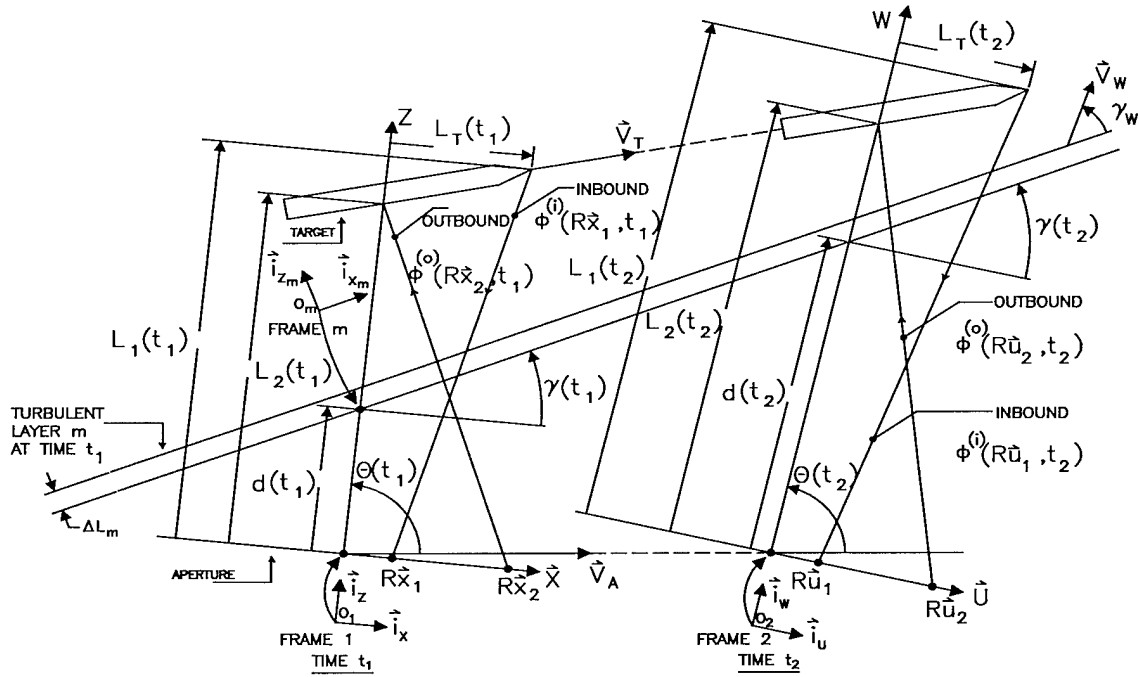
Figure 8. ABL engagement geometry.

This figure is the same as Figure 7 with all of the necessary geometrical constructs included. In particular, there are three reference frames of interest:

1. Frame 1 = $(\vec{i}_x, \vec{i}_z)$ with origin O_1 coincident with the aperture and the $\vec{i}_x$ axis aligned with the aperture at time t_1.

2. Frame 2 = $\left(\vec{i}_u, \vec{i}_w\right)$ with origin O_2 coincident with the aperture and the $\vec{i}_u$ axis aligned with the aperture at time t_2.

3. Frame 3 = $\left(\vec{i}_{x_m}, \vec{i}_{z_m}\right)$ with origin O_m located on the mth turbulent layer and the $\vec{i}_{x_m}$ axis aligned with the turbulent layer.

The notation $\vec{i}_*$ is used to denote a unit vector and the subscripts 'F1', 'F2', and 'Fm' denote vectors written in Frame 1, Frame 2, and Frame m, respectively. Without loss of generality, the vectors $\vec{i}_x$ and $\vec{i}_u$ lie in the plane of the aperture at times t_1 and t_2 and $\vec{V}_A$ and $\vec{V}_T$ are in the $\left(\vec{i}_x, \vec{i}_z\right)$ plane. In other words, this is a planar engagement. The planar engagement has been selected because the ABL operates on missiles in boost phase. Hence, the aperture can be aligned so that the majority of motion occurs in the x-direction. Although this is somewhat restrictive, it is more than adequate for the development of the framework for the application of AO to the ABL. Moreover, the following notation is used to denote the kinematic variables of the engagement geometry:

$\gamma(t_1)$, $\gamma(t_2)$ = angles from the $\vec{i}_x, \vec{i}_u$ axes to the turbulent layer at times t_1, t_2.

$d(t_i)$ = distance from the aperture to the turbulent layer at time t_i, measured normal to the aperture, i = 1, 2.

$L_T(t_i)$ = distance from the aperture normal to the tip of the missile, i = 1, 2.

$L_1(t_i)$ = distance from the tip of the missile to the aperture measured along the aperture normal, i = 1, 2.

$L_2(t_i)$ = distance from the intersection of the aperture normal and the missile to the aperture measured along the aperture normal, i = 1, 2.

$\theta(t_i)$ = angle measured from the aperture velocity vector to the aperture normal vectors, Z and W, respectively, i = 1, 2.

ΔL_m = thickness of the mth turbulent layer.

$\vec{V}_w$ = turbulent layer wind vector, γ_w = angle that the turbulent layer wind vector makes with $\vec{i}_{x_m}$.

$\Phi^{(i)}(R\vec{x}_1, t_1)$, $\Phi^{(i)}(R\vec{u}_1, t_2)$ = inbound, or beacon, wavefront phase.

$\Phi^{(o)}(R\vec{x}_2, t_1)$, $\Phi^{(o)}(R\vec{u}_2, t_2)$ = outbound, or high-energy laser, wavefront phase.

For the upcoming development, it will be necessary to transform vectors written in

reference frames 1 and 2 to vectors written in frame m. To accomplish this, two

transformations are necessary. The first transformation embodies the novel modified

frozen flow hypothesis [20] which takes into account translation as well as rotation of the

system as time progresses from t_1 to t_2. In mathematical terms, given a vector $\vec{r}$, written

in frame 2, the required transformation to express this vector in frame 1 is

$$\vec{r}_{F1} = \begin{bmatrix} \cos\Delta\theta & 0 & \sin\Delta\theta \\ 0 & 1 & 0 \\ -\sin\Delta\theta & 0 & \cos\Delta\theta \end{bmatrix} \vec{r}_{F2} + \begin{bmatrix} \sin\theta(t_1) \\ 0 \\ \cos\theta(t_1) \end{bmatrix} |\vec{V}_A| \Delta t = \mathbf{ROT}(\Delta\theta)\vec{r}_{F2} + \mathbf{TRANS\ 1} \quad (22)$$

where $\Delta\theta = \theta(t_1) - \theta(t_2)$, $\Delta t = t_2 - t_1$, $\mathbf{ROT}(\Delta\theta)$ denotes a rotation matrix, $\mathbf{TRANS\ 1}$ is a

translation vector to frame 1, and $|\bullet|$ denotes the magnitude of the corresponding vector.

The reason for the opposite conventions in the definitions of Δt and $\Delta\theta$ is that a positive

Δt will yield a positive $\Delta\theta$.

The second transformation is as follows: given a vector $\vec{r}$, written in frame 1, the

required transformation to express this vector in frame m is

$$\vec{r}_{Fm} = \begin{bmatrix} \cos\gamma(t_1) & 0 & \sin\gamma(t_1) \\ 0 & 1 & 0 \\ -\sin\gamma(t_1) & 0 & \cos\gamma(t_1) \end{bmatrix} \vec{r}_{F1} + \begin{bmatrix} -d(t_1)\sin\gamma(t_1) \\ 0 \\ -d(t_1)\cos\gamma(t_1) \end{bmatrix} = \mathbf{ROT}\{\gamma(t_1)\}\vec{r}_{F1} + \mathbf{TRANS\ m} .(23)$$

33

3.3 Aperture Vector Projections

In this section, the projections of the aperture vectors, $R\bar{x}_i$ and $R\bar{u}_i$, $i = 1, 2$, into the turbulent layer will be determined. Recall that the only contributions to the correlation between inbound and outbound wavefronts are from the layers. Hence, the spatial separation between aperture vectors projected into the layers must be evaluated. Figure 9 is used to perform these projections. Figure 9 shows the aperture, target, and turbulent layer at one time instant along with the turbulent layer normal vector, $\vec{i}_n$. It is desired to determine an expression for the point (X,Y,Z), in terms of the kinematic variables, which requires evaluation of the line that connects the points (x,y,0) and $(L_T, 0, L(t))$.

To begin, the equation of the plane in which the turbulent layer resides must be determined. The normal vector to the turbulent layer, written in frame 1 coordinates, can be expressed as

$$\vec{i}_n = \begin{bmatrix} -\sin\gamma & 0 & \cos\gamma \end{bmatrix}^T. \tag{24}$$

Then, the equation of the plane in which the turbulent layer lies is

$$-\sin\gamma(X - 0) + 0(Y - 0) + \cos\gamma(Z - d) = 0 \quad \Rightarrow \quad -\tan\gamma X + (Z - d) = 0. \tag{25}$$
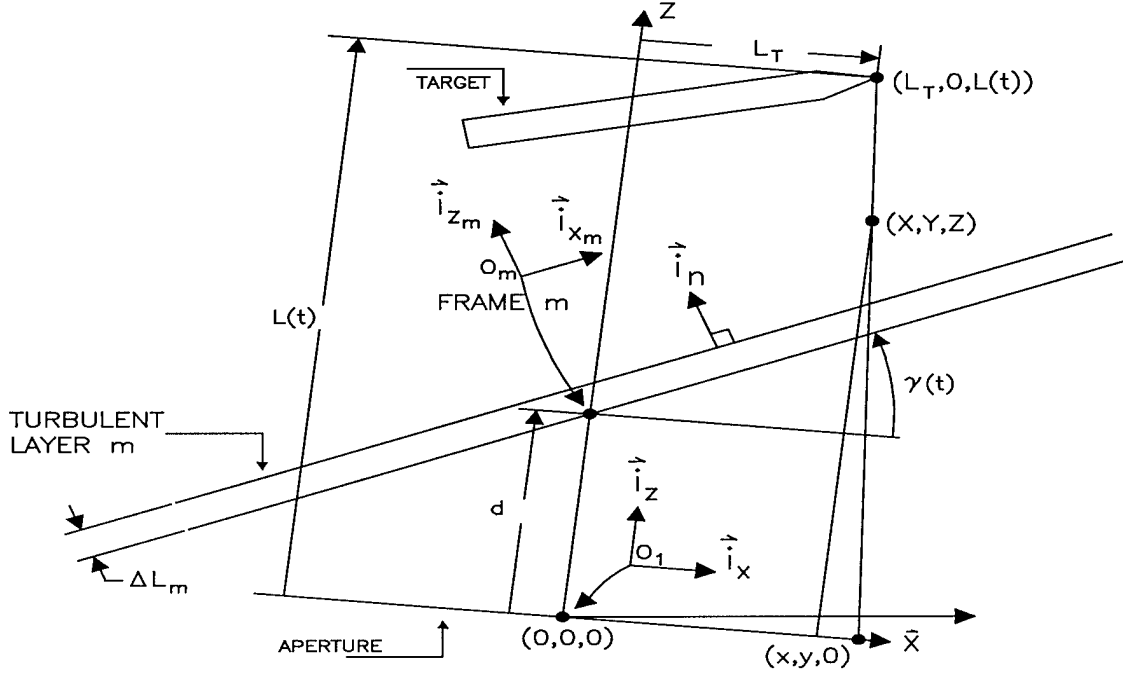
Figure 9. Aperture, target, and turbulent layer for determination of projected vectors.

Now, letting 'sf' be a scale factor, differences in the three components for the line

between (x,y,0) and (L$_T$,0,L(t)) are

$$
\begin{aligned}
X - x &= (sf)(L_T - x) \\
Y - y &= -(sf)y \\
Z &= (sf)L(t) \ .
\end{aligned}
\tag{26}
$$

Using these expressions in the equation of the plane, eq. (25), yields

$$
sf = \frac{x \tan \gamma + d}{L(t) - L_T \tan \gamma + x \tan \gamma} .
\tag{27}
$$

Substituting eq. (27) into eq. (26) gives

$$
\begin{bmatrix} X & Y & Z \end{bmatrix}^T = \left[\frac{L_T d + x\{L(t) - d\}}{L(t) - \tan \gamma (L_T - x)} \quad \frac{L(t) - L_T \tan \gamma - d}{L(t) - \tan \gamma (L_T - x)} \quad \frac{L(t)d + L(t)x \tan \gamma}{L(t) - \tan \gamma (L_T - x)} \right]^T . \tag{28}
$$

35

Therefore, the projection of aperture point (x,y,0) onto the mth layer is given by (X,Y,Z) in eq. (28). In a similar manner, projections for the vectors $R\bar{x}_i$ and $R\bar{u}_i$, i = 1, 2 can be computed. Utilizing the kinematic variables defined in Figure 8 yields the following expressions for the projections of the two aperture vectors at each time instant:

$$\bar{x}_{kpF1} = \begin{bmatrix} X_{kp} \\ Y_{kp} \\ Z_{kp} \end{bmatrix}_{F1} = \frac{1}{L_k(t_1) - \tan\gamma(t_1)\{L_T(t_1)\delta_{k1} - Rx_k\}} \begin{bmatrix} L_T(t_1)d(t_1)\delta_{k1} + \{L_k(t_1) - d(t_1)\}Rx_k \\ \{L_k(t_1) - \tan\gamma(t_1)L_T(t_1)\delta_{k1} - d(t_1)\}Ry_k \\ L_k(t_1)d(t_1) + L_k(t_1)\tan\gamma(t_1)Rx_k \end{bmatrix} \quad (29)$$

$$\bar{u}_{npF2} = \begin{bmatrix} U_{np} \\ V_{np} \\ W_{np} \end{bmatrix}_{F2} = \frac{1}{L_n(t_2) - \tan\gamma(t_2)\{L_T(t_2)\delta_{n1} - Ru_n\}} \begin{bmatrix} L_T(t_2)d(t_2)\delta_{n1} + \{L_n(t_2) - d(t_2)\}Ru_n \\ \{L_n(t_2) - \tan\gamma(t_2)L_T(t_2)\delta_{n1} - d(t_2)\}Rv_n \\ L_n(t_2)d(t_2) + L_n(t_2)\tan\gamma(t_2)Ru_n \end{bmatrix} \quad (30)$$

where $\begin{bmatrix} Rx_k \\ Ry_k \end{bmatrix} = R\bar{x}_k$, $\begin{bmatrix} Ru_n \\ Rv_n \end{bmatrix} = R\bar{u}_n$, the subscript 'p' denotes a projected vector, the subscripts 'F1' and 'F2' denote vectors written in frames 1 and 2, δ_{k1}, δ_{n1} are Kronecker deltas such that $\delta_{k1} = \begin{cases} 1 & \text{if} \quad k = 1 \\ 0 & \text{if} \quad k \neq 1 \end{cases}$, $\delta_{n1} = \begin{cases} 1 & \text{if} \quad n = 1 \\ 0 & \text{if} \quad n \neq 1 \end{cases}$, and k = 1, 2, n = 1, 2. It can be seen that eq. (30) contains kinematic variables defined at time t_2. Hence, relationships between the time t_2 and time t_1 variables must be determined so that expressions in subsequent chapters only contain time t_1 quantities.

3.4 Calculation of d(t$_2$), γ(t$_2$), and the Apparent Thickness of the Turbulent Layer

In this section, relationships between time t_2 kinematic variables and their time t_1 counterparts will be determined. It should be pointed out that d(t$_2$) and γ(t$_2$) are determined by the engagement geometry and the time interval $t_2 - t_1$. Letting ω be the slew rate of the aperture, it is clear that

36

$$\theta(t_2) = \theta(t_1) + \omega(t_2 - t_1). \tag{31}$$

A constant slew rate has been assumed since the sample period is short.

To aid in the calculation of $\gamma(t_2)$, Figure 10 will be used. Figure 10 shows the turbulent layer, the aperture at time t_2, the time t_1 aperture normal vector, Z, lines which are normal to the Z- and W-axes, and some other geometrical constructs.

TIME t_2

Figure 10. Time t_2 geometry for calculation of $\gamma(t_2)$.

As can be seen in Figure 10,

$$\gamma(t_2) = \gamma(t_1) + p. \tag{32}$$

Utilizing triangle QRS and the fact that the sum of the included angles is 180° produces

$$b + 90^\circ + \theta(t_1) - \theta(t_2) = 180^\circ \quad \Rightarrow \quad b = 90^\circ - \theta(t_1) + \theta(t_2). \tag{33}$$

Then, looking at the Z axis at point R, the following relationship becomes apparent:

$$b + p + 90^\circ = 180^\circ \quad \Rightarrow \quad p = \theta(t_1) - \theta(t_2). \tag{34}$$

Using eq. (34) in eq. (32) yields the desired result:

$$\gamma(t_2) = \gamma(t_1) + \theta(t_1) - \theta(t_2). \tag{35}$$

In order to determine $d(t_2)$, Figure 11 will be used. This figure displays the aperture and target at both time instants along with other necessary quantities.

Figure 11. Aperture and target for calculation of $d(t_2)$.

The first step in this process is to determine the length A. This can be accomplished using the law of sines on triangle BCD which produces

$$\frac{d(t_1)}{\sin[\gamma(t_1)+\theta(t_1)-90°]} = \frac{A}{\sin[90°-\gamma(t_1)]} \tag{36}$$

or

$$A = \frac{d(t_1)\cos\gamma(t_1)}{-\cos[\gamma(t_1)+\theta(t_1)]}. \tag{37}$$

Using the law of sines once again, this time on triangle BEF, gives

$$\frac{d(t_2)}{\sin[\gamma(t_1)+\theta(t_1)-90°]} = \frac{A+\left|\vec{V}_A\right|(t_2-t_1)}{\sin[90°-\gamma(t_2)]}. \tag{38}$$

Substituting eq. (37) into eq. (38) and rearranging yields the desired result:

$$d(t_2) = \frac{d(t_1)\cos\gamma(t_1)-\left|\vec{V}_A\right|(t_2-t_1)\cos[\gamma(t_1)+\theta(t_1)]}{\cos[\theta(t_2)-\theta(t_1)-\gamma(t_1)]}. \tag{39}$$

The last quantity of interest in this section is the apparent thickness of the turbulent layer. The thickness of the layer is denoted by ΔL_m. However, since the rays from the beacon and HEL do not pass perpendicular to the turbulent layer, the apparent thickness of the turbulent layer, that is, that amount of each slab which is traversed by each ray, must be determined. Figure 12 will be used to evaluate this quantity. This figure shows the aperture, target, and turbulent layer at one time instant. Other quantities displayed in this figure are the angles h and f and the apparent thickness, denoted by $\Delta L_m^{(1)}$. Using this figure, angle h can be obtained as

$$h = \tan^{-1}\left[\frac{L_1(t_1)}{L_T(t_1) - R|\vec{x}_1|}\right]. \qquad (40)$$

The expression for h can be simplified by considering the physical dimensions of the problem. In particular, the ABL operates with $L_1(t_1)$ on the order of 100 kilometers, $L_T(t_1) \approx 2$ meters, and $R|\vec{x}_1| \leq 0.875$ meters. Therefore, $L_1(t_1) \gg L_T(t_1) - R|\vec{x}_1|$. Hence, h $\approx \pi / 2$. Now, using Figure 12, it can be seen that $h = f + \gamma(t_1) \Rightarrow f \approx \pi / 2 - \gamma(t_1)$. Then, by simple geometry,

$$\sin f = \frac{\Delta L_m}{\Delta L_m^{(1)}} \quad \Rightarrow \quad \Delta L_m^{(1)} \approx \frac{\Delta L_m}{\sin\left(\dfrac{\pi}{2} - \gamma(t_1)\right)} = \frac{\Delta L_m}{\cos\gamma(t_1)}. \qquad (41)$$
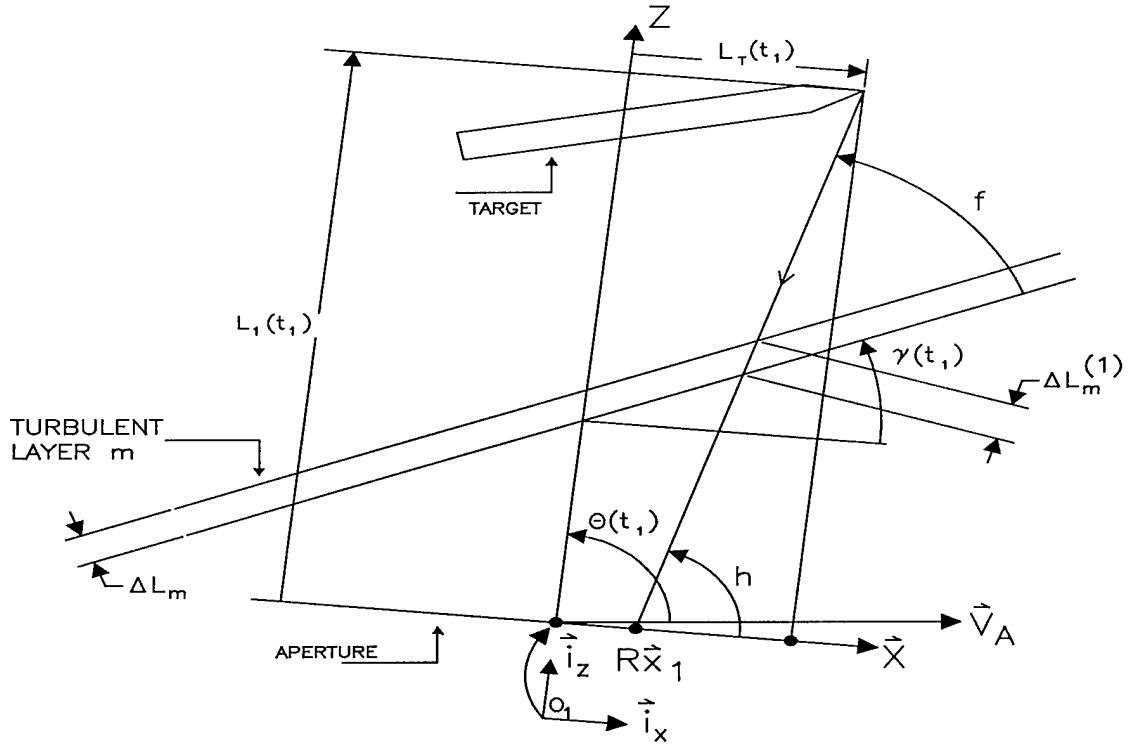
Figure 12. Engagement at one time instant for apparent layer thickness.

In a similar manner, the apparent thicknesses for the other rays can be determined. The expressions are the same as that in eq. (41) with $\gamma(t_1)$ replaced by $\gamma(t_2)$ for time t_2 thicknesses.

3.5 Wind Effect

To incorporate the effect of wind on the turbulent layer, the wind vector is resolved into components written in reference frame 2. Thus,

$$\vec{V}_w = \left[\left|\vec{V}_w\right|\cos\eta \quad 0 \quad \left|\vec{V}_w\right|\sin\eta \right]^T \tag{42}$$

where $\eta = \gamma(t_2) + \gamma_w$ and $\left|\vec{V}_w\right|\cos\eta, \left|\vec{V}_w\right|\sin\eta$ are the components of $\vec{V}_w$ in the U-, W-axis directions, respectively. The wind vector is written in terms of frame 2 coordinates because the effect of wind between times t_1 and t_2 is of interest. Obviously, for $t > t_2$, wind effects also occur, but only two time instants need to be considered in the development. The results can then be propagated to later time instants. In the upcoming development, the subscript 'V$_w$' on a variable is used to indicate that the wind effects have been incorporated into that quantity.

First, consider the wind in the W-axis direction. Figure 13 shows the geometry for this case. In this figure, the aperture and target (source) are shown along with the turbulent layer at times t_1 and t_2. The term source is used since the tip of the target, i.e., the point of reflection of the beacon laser, can be considered a point source. Notice that the W-axis component of the wind moves the turbulent layer only along the W-axis. The

two quantities that need to be evaluated are the new d(t$_2$) distance, denoted $d\left(t_2\right)_{V_W}$, and

the new projected u vector, denoted $\vec{u}_{ipv_W F2}$.
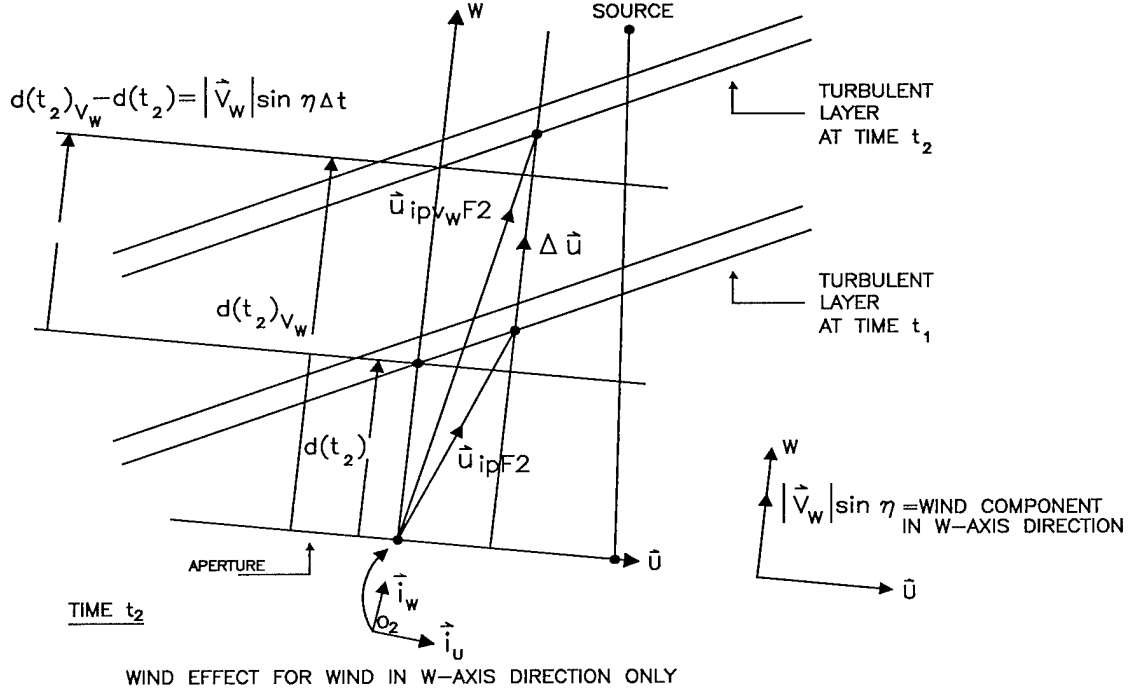
Figure 13. Wind effect in W-axis direction.

It can be seen, from Figure 13, that

$$\vec{u}_{ipv_W F2} = \vec{u}_{ipF2} + \Delta\vec{u} \tag{43}$$

where

$$\Delta\vec{u} = \begin{bmatrix} 0 & 0 & \left|\vec{V}_W\right|\sin\eta \end{bmatrix}^T \Delta t \tag{44}$$

and

$$d\left(t_2\right)_{v_W} = d\left(t_2\right) + \left|\vec{V}_W\right|\sin\eta\,\Delta t . \tag{45}$$

Now, the U-axis contribution of the wind can be examined. Figure 14 shows the geometry for this case. In this figure, the aperture and source are once again shown, but now the turbulent layer has moved from point B, at time t_1, to point C at time t_2. As in the case of the W-axis wind, the two quantities of interest are $d(t_2)_{V_w}$ and $\vec{u}_{ipv_wF2}$.

Clearly, eq. (43) holds, but eq. (44) becomes

$$\Delta \vec{u} = \left[\left| \vec{V}_W \right| \cos \eta \quad 0 \quad 0 \right]^T \Delta t \tag{46}$$

and the new d(t_2) distance is

$$d(t_2)_{V_w} = d(t_2) - \Delta d(t_2) \tag{47}$$

where $\Delta d(t_2)$ is determined by simple geometry using triangle ABC in Figure 14:

$$\Delta d(t_2) = \tan \gamma(t_2) \left| \vec{V}_W \right| \cos \eta \Delta t . \tag{48}$$

Figure 14. Wind effect in U-axis direction.

Putting these results together, that is, using eqs. (43-48) leads to the desired results:

$$\vec{u}_{ipv_wF2} = \vec{u}_{ipF2} + \begin{bmatrix} \left|\vec{V}_w\right|\cos\eta\Delta t \\ 0 \\ \left|\vec{V}_w\right|\sin\eta\Delta t \end{bmatrix}, i = 1, 2 \qquad (49)$$

and

$$d(t_2)_{v_w} = d(t_2) - \tan\gamma(t_2)\left|\vec{V}_w\right|\cos\eta\Delta t + \left|\vec{V}_w\right|\sin\eta\Delta t. \qquad (50)$$

3.6 Projected Aperture Vector Separation and Relationships Between Aperture and Projected Aperture Vectors

To begin, first consider the projected aperture vector separation. As previously stated, in using a layered atmospheric model, the correlation between inbound and outbound wavefronts is due only to the turbulent layers. Hence, the separation between aperture vectors, projected into the slabs, must be determined. The notation used is as follows: $\vec{x}_{kpFm}, \vec{u}_{npv_wFm}$ are the projections of aperture vectors $R\vec{x}_k, R\vec{u}_n$ written in frame m. Figure 15 will be used in this case. Here, the projected vectors are shown, written in frame m and frame 2. From this figure, it is clear that the difference in projected vectors is simply

$$\Delta\vec{s}_m = \vec{u}_{npv_wFm} - \vec{x}_{kpFm}. \qquad (51)$$

Notice that in order to obtain $\vec{u}_{npv_wF_m}$, the transformations described in eqs. (22) and (23) must be applied to $\vec{u}_{npv_wF2}$.
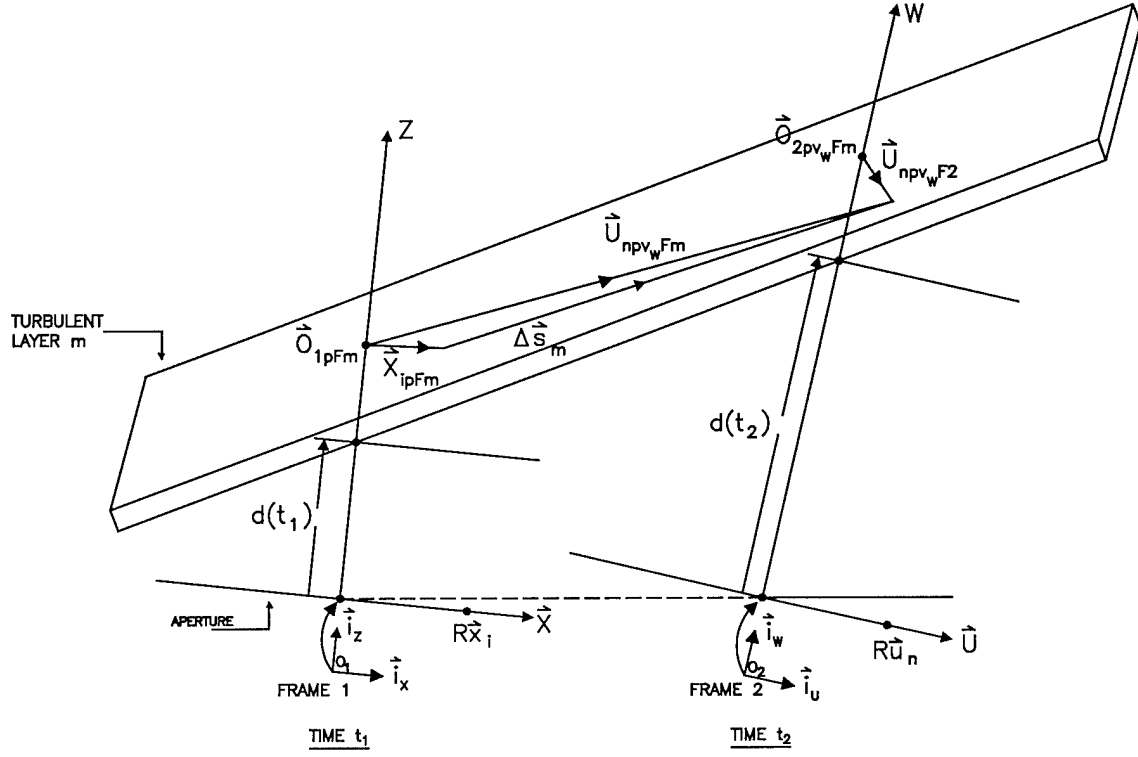
Figure 15. Projected vector separation.

In the upcoming development, an expression for the correlation functions will contain projected and non-projected aperture vectors. In order to determine the correlation contribution from each layer, it is pertinent to have only projected vectors in this expression. Hence, a relationship between projected and non-projected aperture vectors must be determined. First, consider the relationship between $R\vec{x}_{kFl}$ and $\vec{x}_{kpFm}$. Applying the transformation in eq. (23) to eq. (29) gives

$$\vec{x}_{kpFm} = \frac{1}{L_k(t_1)} \left\{ \left[\begin{array}{cc} \dfrac{L_k(t_1)-d(t_1)}{\cos\gamma(t_1)} & 0 \\ 0 & L_k(t_1)-d(t_1) \end{array} \right] R\vec{x}_{kFl} + \left[\begin{array}{c} \dfrac{L_T(t_1)d(t_1)}{\cos\gamma(t_1)}\delta_{k1} \\ 0 \end{array} \right] \right\} = \frac{1}{L_k(t_1)} \left\{ A_{xk} R\vec{x}_{kFl} + B_{xk} \right\}, \ k = 1,2 \ .$$

(52)

Then, it is clear that

$$R\vec{x}_{kFl} = A_{xk}^{-1}\left\{L_k(t_1)\vec{x}_{kpFm} - B_{xk}\right\}, \; k = 1, 2. \tag{53}$$

The expressions in eq. (52) were obtained using an approximation which produced a linear relationship between $R\vec{x}_{kFl}$ and $\vec{x}_{kpFm}$. In the full expression, the relationship between $R\vec{x}_{kFl}$ and $\vec{x}_{kpFm}$ is nonlinear; however, letting

$$L_k(t_1) >> \tan\gamma(t_1)\left\{L_T(t_1)\delta_{k1} - R|\vec{x}_{kFl}|\right\}, \; k = 1, 2, \tag{54}$$

the linear result in eq. (52) is produced. For the case of $R\vec{u}_{nF2}$ and $\vec{u}_{npv_wFm}$, the same reasoning has been employed to produce

$$\vec{u}_{npv_wFm} = \frac{1}{L_n(t_2)}\left\{\begin{bmatrix} \dfrac{L_n(t_2)}{\cos\gamma(t_2)} + a & 0 \\ 0 & L_n(t_2) - d(t_2)_{V_w} \end{bmatrix} R\vec{u}_{nF2} + \begin{bmatrix} b_{un} \\ 0 \end{bmatrix}\right\} = \frac{1}{L_n(t_2)}\left\{A_{un}R\vec{u}_{nF2} + B_{un}\right\}, \; n = 1, 2 \tag{55}$$

where

$$a = -\cos\gamma(t_2)d(t_2)_{V_w} - \tan\gamma(t_2)\{\chi\}, \tag{56}$$

$$b_{un} = d(t_2)_{V_w}\left\{\cos\gamma(t_2)L_T(t_2)\delta_{n1} + \sin\gamma(t_2)L_n(t_2)\right\} - L_n(t_2)\{\chi\}, \tag{57}$$

and

$$\chi = \cos\gamma(t_2)|\vec{V}_W|\cos\eta\Delta t + \sin\gamma(t_2)|\vec{V}_W|\sin\eta\Delta t - \sin[\gamma(t_1) + \theta(t_1)]|\vec{V}_A|\Delta t + d(t_1)\sin\gamma(t_1), \tag{58}$$

$n = 1, 2$. Therefore, it can be seen that

$$R\vec{u}_{nF2} = A_{un}^{-1}\left\{L_n(t_2)\vec{u}_{npv_wFm} - B_{un}\right\}, \; n = 1, 2. \tag{59}$$

It should be noted that A_{xk}, $k = 1, 2$, and A_{un}, $n = 1, 2$ are diagonal matrices. Hence, multiplication of these matrices with each other will be commutative.

46

3.7 Summary

In this chapter, the aperture vectors have been projected into the turbulent layers, the desired vector separation has been determined, and the kinematic variable relationships have been evaluated. At this point, all of the required geometrical analysis for this problem has been performed. It is now necessary to evaluate the correlation of the Zernike polynomial expansion coefficients using the analysis in this chapter. As can be seen in Figure 8, the inbound (beacon) and outbound (high-energy laser) wavefronts propagate through different regions of the atmosphere at different times. In other words, the sensed wavefront perturbations and the high-energy laser wavefront are associated with different observation directions. Therefore, the phase perturbations associated with the two wavefronts are different. This performance degradation is referred to as an anisoplanatic effect. To account for anisoplanatic effects, the correlation between wavefronts arising from the two directions must be evaluated. In Chapter 4, an expression for this correlation is derived.

IV. Atmospheric Modeling

4.1 Introduction

The correlation between inbound and outbound wavefronts is determined in this chapter. Since measurements in the ABL scenario are of the inbound wavefront's phase, the correlation between the inbound and outbound wavefronts must be evaluated in order to determine the effects of turbulence on the outbound wavefront's propagation path. The outbound propagation path is important since the HEL is fired through this section of atmosphere. Once the correlation functions are determined, this data will be used to synthesize a stochastic, linear, dynamical system which will serve as the model for the atmosphere.

4.2 Correlation of Inbound and Outbound Wavefronts

With the analysis from Chapter 3 in place, the correlation between Zernike polynomial phase expansion coefficients can now be determined. Much of the development of the correlation functions follows the work of Takato and Yamaguchi [26], Valley and Wandzura [30], and Whiteley [35, 36]. Modifications have been made including the modified frozen flow hypothesis, appropriate layer thicknesses, and the ABL-specific geometry.

Utilizing the Zernike polynomial expansion in eq. (17), the inbound and outbound wavefront phases can be written as

$$\Phi^{(i)}\left(R\vec{x}_{1F1},t_1\right) = \sum_f a_f^{(i)}\left(t_1\right)Z_f(\vec{x}_{1F1}), \quad \Phi^{(o)}\left(R\vec{x}_{2F1},t_1\right) = \sum_f a_f^{(o)}\left(t_1\right)Z_f(\vec{x}_{2F1}) \quad (60)$$

and

$$\Phi^{(i)}\left(R\vec{u}_{1F2},t_2\right)=\sum_j a_j^{(i)}\left(t_2\right)Z_j(\vec{u}_{1F2}), \quad \Phi^{(o)}\left(R\vec{u}_{2F2},t_2\right)=\sum_j a_j^{(o)}\left(t_2\right)Z_j(\vec{u}_{2F2}), \quad (61)$$

where $a_f^{(i)}(t_1)$, $a_f^{(o)}(t_1)$, $a_j^{(i)}(t_2)$, and $a_j^{(o)}(t_2)$ are the Zernike polynomial phase expansion

coefficients. The superscripts (i) and (o) refer to the inbound and outbound wavefronts.

The expansions used in this work will include two modes, that is, f = 2, 3 and j = 2, 3.

Zernike mode number one is termed piston (aperture averaged phase) and is not a

distortive contributor. Hence, it is ignored in the expansions. The general forms in eqs.

(60) and (61) will be used to allow the framework to be built using as many modes as one

desires. The decision to use two modes will be discussed later in this work.

These equations can be written in more compact forms as

$$\Phi^{(i,o)}\left(R\vec{x}_{kF1},t_1\right)=\sum_f a_f^{(i,o)}\left(t_1\right)Z_f(\vec{x}_{kF1}), \quad k=1,2 \qquad (62)$$

and

$$\Phi^{(i,o)}\left(R\vec{u}_{nF2},t_2\right)=\sum_j a_j^{(i,o)}\left(t_1\right)Z_j(\vec{u}_{nF2}), \quad n=1,2 \qquad (63)$$

where the notation $\Phi^{(i,o)}(\bullet,\bullet)$ and $a^{(i,o)}(t)$ designate the inbound and outbound phase and

Zernike coefficients depending on which aperture vectors are used. In other words, if

using aperture location $\vec{x}_{1F1}$ in eq. (62), i.e., k = 1, then the inbound wavefront,

superscript (i), is under consideration. If aperture location $\vec{x}_{2F1}$ in eq. (62) is used, i.e., k

= 2, then the outbound wavefront, superscript (o), is under consideration. The same holds

for the expressions in eq. (63). This notation allows derivation of the correlation between

inbound and outbound wavefronts to be evaluated in the general case, with the desired

combination of wavefronts substituted later. The Zernike coefficients can now be determined as specified in eq. (18):

$$a_f^{(i,o)}(t_1) = \int W(\vec{x}_{kFl}) Z_f(\vec{x}_{kFl}) \Phi^{(i,o)}(R\vec{x}_{kFl}, t_1) d\vec{x}_{kFl} \qquad (64)$$

and

$$a_j^{(i,o)}(t_2) = \int W(\vec{u}_{jF2}) Z_j(\vec{u}_{nF2}) \Phi^{(i,o)}(R\vec{u}_{nF2}, t_2) d\vec{u}_{nF2} \qquad (65)$$

where the integration is taken over the entire two-dimensional plane and $W(\bullet)$ was defined in eq. (19). Since it is desired to determine the correlation between the wavefronts, and the wavefronts have been expanded using eqs. (60) and (61), it follows that the desired expression can be evaluated by computing the correlation between the Zernike expansion coefficients. Hence, the correlation becomes

$$\Gamma_{a_f^{(i,o)}(t_1) a_j^{(i,o)}(t_2)} = E\left\{ a_f^{(i,o)}(t_1) a_j^{(i,o)}(t_2) \right\}$$

$$= E\left\{ \iint W(\vec{x}_{kFl}) Z_f(\vec{x}_{kFl}) W(\vec{u}_{nF2}) Z_f(\vec{u}_{nF2}) \Phi^{(i,o)}(R\vec{x}_{kFl}, t_1) \Phi^{(i,o)}(R\vec{u}_{nF2}, t_2) d\vec{x}_{kFl} d\vec{u}_{nF2} \right\}$$

$$= \iint W(\vec{x}_{kFl}) Z_f(\vec{x}_{kFl}) W(\vec{u}_{nF2}) Z_f(\vec{u}_{nF2}) E\left\{ \Phi^{(i,o)}(R\vec{x}_{kFl}, t_1) \Phi^{(i,o)}(R\vec{u}_{nF2}, t_2) \right\} d\vec{x}_{kFl} d\vec{u}_{nF2}$$

$$(66)$$

where the last expression was obtained using the linearity property of the expectation operator and $\Gamma_{a_f^{(i,o)}(t_1) a_j^{(i,o)}(t_2)}$ is the correlation between Zernike coefficients.

In order to evaluate the integral in eq. (66), it is necessary to determine

$$E\left\{ \Phi^{(i,o)}(R\vec{x}_{kFl}, t_1) \Phi^{(i,o)}(R\vec{u}_{nF2}, t_2) \right\}. \qquad (67)$$

Some of the properties described in Chapter 2 are now necessary. In particular, using a layered atmospheric model and assuming that all layers are of equal thickness and the

index of refraction fluctuations are uncorrelated layer to layer (by suitably placing the layers as discussed in Chapter 2), a wavefront's turbulence-induced phase can be expressed as

$$\Phi(\vec{x}) = \kappa \sum_m \Delta L_m^{(k)} n_m(\vec{x}, t) \tag{68}$$

where $\kappa = 2\pi / \lambda$ is the spatial wavenumber, λ is the wavelength, m is a layer subscript, $\Delta L_m^{(k)}$ is the apparent thickness of the mth layer as seen by the kth wavefront, and $n_m(\vec{x}, t)$ is the mth layer's randomly fluctuating index of refraction term. Using eq. (68) in eq. (67) produces

$$E\left\{ \Phi^{(i,o)}\left(R\vec{x}_{kF1}\right) \Phi^{(i,o)}\left(R\vec{u}_{nF2}\right) \right\} = E\left\{ \kappa^2 \sum_m \Delta L_m^{(k)} \Delta L_m^{(n)} n_m\left(\vec{x}_{kpF1}, t_1\right) n_m\left(\vec{u}_{npF2}, t_2\right) \right\} \tag{69}$$

where $\Delta L_m^{(k)}$, $\Delta L_m^{(n)}$ are the apparent layer thicknesses for the kth, n^{th} wavefronts and $\vec{x}_{kpF1}, \vec{u}_{npF2}$ are the projected aperture vectors written in frame 1 and frame 2. Frame 2 is used for $\vec{u}_{np}$ since the modified frozen flow hypothesis (FFH) has not been included. In fact, applying the modified FFH, as described in eq. (22), yields

$$n_m(\vec{u}_{npF2}, t_2) = n_m(\vec{u}_{npF1}, t_1). \tag{70}$$

In other words, the modified FFH takes into account target and source motion and thus relates frame 2, time t_2 variables to frame 1, time t_1 variables.

Now, transforming the vectors in eq. (69) to frame m and incorporating the effects of wind produces

51

$$E\left\{\Phi^{(i,o)}\left(R\vec{x}_{kFl}\right)\Phi^{(i,o)}\left(R\vec{u}_{nF2}\right)\right\} = E\left\{\kappa^2\sum_m \Delta L_m^{(k)}\Delta L_m^{(n)} n_m\left(\vec{x}_{kpFm},t_1\right)n_m\left(\vec{u}_{npv_wFm},t_1\right)\right\}$$

$$= \frac{\sum_m\left[\kappa^2\Delta L_m^2 E\left\{n_m\left(\vec{x}_{kpFm},t_1\right)n_m\left(\vec{u}_{npv_wFm},t_1\right)\right\}\right]}{\cos\gamma(t_1)\cos\gamma(t_2)} \qquad (71)$$

where the cosine terms arise because the expression for the apparent layer thickness has been included. It can be seen that the term in brackets is the spatial autocorrelation of the phase in the mth layer. Thus

$$E\left\{\Phi^{(i,o)}\left(R\vec{x}_{kFl}\right)\Phi^{(i,o)}\left(R\vec{u}_{nF2}\right)\right\} = \frac{\sum_m \Gamma_{\Phi_m}\left(\vec{x}_{kpFm},\vec{u}_{npv_wFm},t_1\right)}{\cos\gamma(t_1)\cos\gamma(t_2)} \qquad (72)$$

where $\Gamma_{\Phi_m}\left(\bullet,\bullet,t_1\right)$ denotes the spatial autocorrelation. Under the assumptions of homogeneous and isotropic statistics, as addressed in Chapter 2, $\Gamma_{\Phi_m}\left(\bullet,\bullet,t_1\right)$ will be a function only of the vector separation between its arguments. Therefore, using eq. (51),

$$\Gamma_{\Phi_m}\left(\vec{x}_{kpFm},\vec{u}_{npv_wFm},t_1\right) = \Gamma_{\Phi_m}\left(\Delta\vec{s}_m,t_1\right) = \Gamma_{\Phi_m}\left(\vec{u}_{npv_wFm}-\vec{x}_{kpFm},t_1\right). \qquad (73)$$

Substituting eq. (73) into eq. (72), using this result in eq. (66), and interchanging the order of integration and summation produces

$$\Gamma_{a_f^{(i,o)}(t_1)a_j^{(i,o)}(t_2)} = E\left\{a_f^{(i,o)}(t_1)a_j^{(i,o)}(t_2)\right\}$$

$$= \sum_m\frac{1}{\cos\gamma(t_1)\cos\gamma(t_2)}\iint\Gamma_{\Phi_m}\left(\vec{u}_{npv_wFm}-\vec{x}_{kpFm}\right)W\left(\vec{x}_{kFl}\right)Z_f\left(\vec{x}_{kFl}\right)W\left(\vec{u}_{nF2}\right)Z_f\left(\vec{u}_{nF2}\right)d\vec{x}_{kFl}d\vec{u}_{nF2} \; .$$

$$(74)$$

52

Due to the fact that eq. (74) contains projected and non-projected aperture vectors, the transformations given in eqs. (53) and (59) must be used to obtain only projected vectors. Applying these transformations yields

$$
\Gamma_{a_i^{(1,\omega)}(t_1)a_j^{(1,\omega)}(t_2)} = \sum_m \frac{1}{c\gamma(t_1)c\gamma(t_2)} \iint \Gamma_{\Phi_m}(\bar{u}_{npv_wFm} - \bar{x}_{kpFm})W\left[\frac{A_x^{-1}}{R}\left\{L(t_1)\bar{x}_{kpFm} - B_x\right\}\right]Z_f\left[\frac{A_x^{-1}}{R}\left\{L(t_1)\bar{x}_{kpFm} - B_x\right\}\right]
$$

$$
*W\left[\frac{A_u^{-1}}{R}\left\{L(t_2)\bar{u}_{npv_wFm} - B_u\right\}\right]Z_j\left[\frac{A_u^{-1}}{R}\left\{L(t_2)\bar{u}_{npv_wFm} - B_u\right\}\right]\left[\frac{A_x^{-1}L(t_1)}{R}\right]d\bar{x}_{kpFm}\left[\frac{A_u^{-1}L(t_2)}{R}\right]d\bar{u}_{npv_wFm}
$$

(75)

where $A_x^{-1}, L(t_1), B_x$ are $A_{x1}^{-1}, L_1(t_1), B_{x1}$ if $k = 1$ or $A_{x2}^{-1}, L_2(t_1), B_{x2}$ if $k = 2$, and likewise for the $\bar{u}$ components.

There are well-known forms for the Power Spectral Density (PSD) corresponding to the spatial autocorrelation of the phase, namely, the Kolmogorov and von Karman spectra. Since the autocorrelation of the phase and its PSD form a Fourier transform pair, transform techniques can be applied to eq. (75) to obtain a PSD term. This analysis follows the development in the work of Takato and Yamaguchi [26] and simplifies the integrations described in eq. (75). The following transform property, among others, will be useful, assuming that $s(\bar{r})$ is Fourier transformable: $FT\{\bullet\}$ denotes the Fourier transform of $\{\bullet\}$.

- Scaling and shifting property [7]:

$$
FT\{s(a_1x + b_1y + c_1, a_2x + b_2y + c_2)\} = \frac{1}{|D|}e^{-j2\pi(x_o\omega_1 + y_o\omega_2)}S\left[\frac{b_2}{D}\omega_1 - \frac{a_2}{D}\omega_2, \frac{-b_1}{D}\omega_1 + \frac{a_1}{D}\omega_2\right]
$$

(76)

where $D = a_1 b_2 - a_2 b_1$, $x_o = \dfrac{b_1 c_2 - b_2 c_1}{D}$, and $y_o = \dfrac{a_2 c_1 - a_1 c_2}{D}$.

First, consider the integral over $\vec{u}_{npv_wFm}$ in eq. (75). Letting

$$\mathbf{A}_u = \begin{bmatrix} A_{u1,1} & 0 \\ 0 & A_{u2,2} \end{bmatrix}, \mathbf{B}_u = \begin{bmatrix} B_{u1,1} \\ 0 \end{bmatrix}, \vec{u}_{npv_wFm} = \begin{bmatrix} u_{npv_wFm}(1) \\ u_{npv_wFm}(2) \end{bmatrix}, \vec{k} = \begin{bmatrix} k_1 \\ k_2 \end{bmatrix}, \tag{77}$$

the terms inside the weighting function and Zernike polynomial can be expressed as

$$\frac{\mathbf{A}_u^{-1}}{R}\left\{L(t_2)\vec{u}_{npv_wFm} - \mathbf{B}_u\right\} = \left[\left(\frac{L(t_2)u_{npv_wFm}(1)}{RA_{u1,1}} - \frac{B_{u1,1}}{RA_{u1,1}}\right) \quad \frac{L(t_2)u_{npv_wFm}(2)}{RA_{u2,2}}\right]^T. \tag{78}$$

Using eqs. (75) and (77), the components a_1, b_1, c_1, a_2, b_2, c_2, D, x_o, and y_o can be

identified and the Fourier transform of $Z_j(\bullet)W(\bullet)$ can be written as

$$FT\left\{Z_j\left[\frac{\mathbf{A}_u^{-1}}{R}\left\{L(t_2)\vec{u}_{npv_wFm} - \mathbf{B}_u\right\}\right]W\left[\frac{\mathbf{A}_u^{-1}}{R}\left\{L(t_2)\vec{u}_{npv_wFm} - \mathbf{B}_u\right\}\right]\right\} = \frac{R^2}{L^2(t_2)}\frac{1}{\left|\det(\mathbf{A}_u^{-1})\right|}e^{-j2\pi\vec{k}\bullet\frac{\mathbf{B}_u}{L(t_2)}}Q_j^*\left[\frac{RA_u\vec{k}}{L(t_2)}\right]$$

$$\tag{79}$$

where $Q_j^*(f)$ is the Fourier transform of $Z_j^*(f)W(f)$, '$*$' denotes complex conjugation, and

the dot ($\bullet$) in $e^{-j2\pi\vec{k}\bullet\frac{\mathbf{B}_u}{L(t_2)}}$ denotes dot product. Using this result and Parseval's Theorem

[8] in eq. (75) produces

$$\Gamma_{a_f^{(i,o)}(t_1)a_j^{(i,o)}(t_2)} = \sum_m \frac{1}{c\gamma(t_1)c\gamma(t_2)}\iint FT\left\{\Gamma_{\Phi_m}(\vec{u}_{npv_wFm} - \vec{x}_{kpFm})\right\}W\left[\frac{\mathbf{A}_x^{-1}}{R}\left\{L(t_1)\vec{x}_{kpFm} - \mathbf{B}_x\right\}\right]$$

$$*Z_f\left[\frac{\mathbf{A}_x^{-1}}{R}\left\{L(t_1)\vec{x}_{kpFm} - \mathbf{B}_x\right\}\right]\frac{R}{L(t_2)}\frac{1}{\left|\det(\mathbf{A}_u^{-1})\right|}e^{-j2\pi\vec{k}\bullet\left(\frac{\mathbf{B}_u}{L(t_2)}\right)}Q_j^*\left[\frac{RA_u}{L(t_2)}\vec{k}\right]\left[\frac{\mathbf{A}_x^{-1}L(t_1)}{R}\right]d\vec{x}_{kpFm}\mathbf{A}_u^{-1}d\vec{k}.$$

$$\tag{80}$$

Using the Wiener-Khinchin theorem [7] and the shifting property of the Fourier transform

gives

$$FT\left\{\Gamma_{\Phi_m}(\vec{u}_{npv_wFm} - \vec{x}_{kpFm})\right\} = W_{\Phi_m}(\vec{\kappa})e^{-j2\pi\vec{\kappa}\bullet(-\vec{x}_{kpFm})} \tag{81}$$

where $W_{\Phi_m}(\vec{\kappa})$ is the PSD of the spatial autocorrelation of the phase in the mth layer.

Substituting eq. (81) into eq. (80) and rearranging yields

$$\Gamma_{a_i^{(i,o)}(t_1)a_j^{(i,o)}(t_2)} = \sum_m \frac{1}{c\gamma(t_1)c\gamma(t_2)}\frac{R}{L(t_2)}\frac{1}{\left|\det(A_u^{-1})\right|}\int W_{\Phi_m}(\vec{\kappa})e^{-j2\pi\vec{\kappa}\bullet\left(\frac{B_u}{L(t_2)}\right)}Q_j^*\left[\frac{RA_u}{L(t_2)}\vec{\kappa}\right]$$

$$*\left(\int e^{j2\pi\vec{\kappa}\bullet\vec{x}_{kpFm}}W\left[\frac{A_x^{-1}}{R}\left\{L(t_1)\vec{x}_{kpFm} - B_x\right\}\right]Z_f\left[\frac{A_x^{-1}}{R}\left\{L(t_1)\vec{x}_{kpFm} - B_x\right\}\right]\left[\frac{A_x^{-1}L(t_1)}{R}\right]d\vec{x}_{kpFm}\right)A_u^{-1}d\vec{\kappa} \tag{82}$$

Using the Fourier transform properties once again, the term in parentheses in eq. (82) can be transformed to yield

$$\Gamma_{a_i^{(i,o)}(t_1)a_j^{(i,o)}(t_2)} = \sum_m \frac{1}{c\gamma(t_1)c\gamma(t_2)}\frac{R^2}{L(t_1)L(t_2)}\left|\det(A_x)\right|\left|\det(A_u)\right|$$

$$*\int W_{\Phi_m}(\vec{\kappa})e^{-j2\pi\vec{\kappa}\bullet\left(\frac{B_u}{L(t_2)}+\frac{B_x}{L(t_1)}\right)}Q_f\left[\frac{RA_x}{L(t_1)}\vec{\kappa}\right]Q_j^*\left[\frac{RA_u}{L(t_2)}\vec{\kappa}\right]A_x^{-1}A_u^{-1}d\vec{\kappa} \tag{83}$$

where A_x and A_u are 2-by-2 diagonal matrices. Thus, multiplication of these two matrices is commutative.

Equation (83) provides the desired result, that is, the correlation between Zernike polynomial phase expansion coefficients. However, double integrations are not feasible in an on-line situation. Therefore, it would be desirable to obtain a simplified expression by integrating out one component of the frequency vector. To simplify eq. (83), consider converting the Cartesian integral into an equivalent polar integral. Letting

$$A_x^{-1}A_u^{-1}\vec{\kappa} = \vec{\bar{\kappa}} \quad \Rightarrow \quad A_x^{-1}A_u^{-1}d\vec{\kappa} = d\vec{\bar{\kappa}}, \tag{84}$$

it can be seen that (recalling the A_x and A_u are diagonal, so that they commute)

$$\vec{\kappa} = \mathbf{A}_x \mathbf{A}_u \tilde{\vec{\kappa}} \quad , \quad \frac{RA_u}{L(t_2)} \vec{\kappa} = \frac{RA_x A_u^2}{L(t_2)} \tilde{\vec{\kappa}} \quad , \text{ and } \quad \frac{RA_x}{L(t_1)} \vec{\kappa} = \frac{RA_x^2 A_u}{L(t_1)} \tilde{\vec{\kappa}} . \tag{85}$$

Also, $W_{\Phi_m}(\vec{\kappa}) \rightarrow W_{\Phi_m}(\mathbf{A}_x \mathbf{A}_u \tilde{\vec{\kappa}})$ and letting $\vec{\alpha} = \dfrac{\mathbf{B}_u}{L(t_2)} + \dfrac{\mathbf{B}_x}{L(t_1)}$ yields

$e^{-j2\pi\vec{\kappa}\bullet\vec{\alpha}} \rightarrow e^{-j2\pi\mathbf{A}_x\mathbf{A}_u\tilde{\vec{\kappa}}\bullet\vec{\alpha}}$. Therefore, eq. (83) becomes

$$\Gamma_{a_i^{(i,o)}(t_1)a_j^{(i,o)}(t_2)} = \sum_m \frac{1}{c\gamma(t_1)c\gamma(t_2)} \frac{R^2}{L(t_1)L(t_2)} \left|\det(\mathbf{A}_x)\right|\left|\det(\mathbf{A}_u)\right|$$

$$* \int W_{\Phi_m}(\mathbf{A}_x\mathbf{A}_u\tilde{\vec{\kappa}})e^{-j2\pi(\mathbf{A}_x\mathbf{A}_u\tilde{\vec{\kappa}})\bullet\vec{\alpha}} Q_f\left[\frac{RA_x^2 A_u}{L(t_1)}\tilde{\vec{\kappa}}\right]Q_j^*\left[\frac{RA_x A_u^2}{L(t_2)}\tilde{\vec{\kappa}}\right]d\tilde{\vec{\kappa}} . \tag{86}$$

For notational simplicity, let

$$\tilde{\vec{\kappa}}_1 = \vec{\kappa} = \mathbf{A}_x\mathbf{A}_u\tilde{\vec{\kappa}} \quad , \quad \tilde{\vec{\kappa}}_2 = \frac{RA_x A_u^2}{L(t_2)}\tilde{\vec{\kappa}} \quad , \text{ and } \quad \tilde{\vec{\kappa}}_3 = \frac{RA_x^2 A_u}{L(t_1)}\tilde{\vec{\kappa}} , \tag{87}$$

where $\tilde{\vec{\kappa}}_1$ = vector whose angle to $\vec{i}_{x_m}$ is $\tilde{\theta}_1$, $\tilde{\vec{\kappa}}_2$ = vector whose angle to $\vec{i}_{x_m}$ is $\tilde{\theta}_2$, $\tilde{\vec{\kappa}}_3$ =

vector whose angle to $\vec{i}_{x_m}$ is $\tilde{\theta}_3$, and $\vec{\alpha}$ = vector whose angle to $\vec{i}_{x_m}$ is $\tilde{\theta}_\alpha$. Thus,

converting eq. (86) to an equivalent polar integral produces

$$\Gamma_{a_i^{(i,o)}(t_1)a_j^{(i,o)}(t_2)} = \sum_m \frac{1}{c\gamma(t_1)c\gamma(t_2)} \frac{R^2}{L(t_1)L(t_2)} \left|\det(\mathbf{A}_x)\right|\left|\det(\mathbf{A}_u)\right|$$

$$* \iint W_{\Phi_m}\left(\left|\tilde{\vec{\kappa}}_1\right|\right)e^{-j2\pi\left|\tilde{\vec{\kappa}}_1\right|\left|\vec{\alpha}\right|\cos\left(\tilde{\theta}_1 - \theta_\alpha\right)} Q_f\left[\left|\tilde{\vec{\kappa}}_2\right|, \tilde{\theta}_2\right]Q_j^*\left[\left|\tilde{\vec{\kappa}}_3\right|, \tilde{\theta}_3\right]\left|\tilde{\vec{\kappa}}\right|d\left|\tilde{\vec{\kappa}}\right|d\tilde{\theta} . \tag{88}$$

Now, letting

$$\mathbf{A}_x = \begin{bmatrix} A_{x1,1} & 0 \\ 0 & A_{x2,2} \end{bmatrix} \text{ and } \mathbf{A}_u = \begin{bmatrix} A_{u1,1} & 0 \\ 0 & A_{u2,2} \end{bmatrix} , \tag{89}$$

it can be seen that

$$\vec{\tilde\kappa} = \begin{bmatrix} \tilde\kappa_1 \\ \tilde\kappa_2 \end{bmatrix} = \frac{\begin{bmatrix} A_{x2,2}A_{u2,2}\kappa_1 \\ A_{x1,1}A_{u1,1}\kappa_2 \end{bmatrix}}{\det \mathbf{A}_x \det \mathbf{A}_u} \Rightarrow \tilde\theta = \tan^{-1}\left(\frac{A_{x1,1}A_{u1,1}\kappa_2}{A_{x2,2}A_{u2,2}\kappa_1} \right),$$

$$\vec{\tilde\kappa}_1 = \begin{bmatrix} A_{x1,1}A_{u1,1}\tilde\kappa_1 \\ A_{x2,2}A_{u2,2}\tilde\kappa_2 \end{bmatrix} \Rightarrow \tilde\theta_1 = \tan^{-1}\left(\frac{A_{x2,2}A_{u2,2}}{A_{x1,1}A_{u1,1}} \tan\tilde\theta \right), \tag{90}$$

and

$$\vec{\tilde\kappa}_2 = \begin{bmatrix} \dfrac{RA_{x1,1}A_{u1,1}^2\tilde\kappa_1}{L(t_2)} \\ \dfrac{RA_{x2,2}A_{u2,2}^2\tilde\kappa_2}{L(t_2)} \end{bmatrix} \Rightarrow \tilde\theta_2 = \tan^{-1}\left(\frac{A_{x2,2}A_{u2,2}^2}{A_{x1,1}A_{u1,1}^2} \tan\tilde\theta \right),$$

$$\vec{\tilde\kappa}_3 = \begin{bmatrix} \dfrac{RA_{x1,1}^2A_{u1,1}\tilde\kappa_1}{L(t_1)} \\ \dfrac{RA_{x2,2}^2A_{u2,2}\tilde\kappa_2}{L(t_1)} \end{bmatrix} \Rightarrow \tilde\theta_3 = \tan^{-1}\left(\frac{A_{x2,2}^2A_{u2,2}}{A_{x1,1}^2A_{u1,1}} \tan\tilde\theta \right). \tag{91}$$

Using Noll's expressions for the Fourier transform of the Zernike polynomials [18], that

is,

$$Q_f(\kappa,\theta) = \sqrt{n_f+1}\,(-1)^{\frac{n_f}{2}}\sqrt{2}^{\left(1-\delta_{m_f,0}\right)}\frac{J_{n_f+1}(2\pi\kappa)}{\pi\kappa}\cos\left\{m_f\theta + \frac{\pi}{4}\left(1-\delta_{m_f,0}\right)\left[(-1)^f - 1\right]\right\} \tag{92}$$

where n, m are the radial degree and azimuthal frequency of the Zernike polynomials,

$J_{n_f+1}(\bullet)$ is a Bessel function of the first kind of order ($n_f + 1$), and $\delta_{m_f 0}$ is a Kronecker

delta such that $\delta_{m_f 0} = \begin{Bmatrix} 1 & \text{if } m_f = 0 \\ 0 & \text{otherwise} \end{Bmatrix}$, in eq. (88) yields

$$\Gamma_{a_f^{(i,o)}(t_1)a_j^{(i,o)}(t_2)} = \sum_m \frac{1}{c\gamma(t_1)c\gamma(t_2)} \frac{R^2}{L(t_1)L(t_2)} \left|\det(\mathbf{A_x})\right|\left\|\det(\mathbf{A_u})\right| \left\{(n_f+1)(n_j+1)\right\}^{\frac{1}{2}} (-1)^{\frac{n_f+n_j}{2}} (-1)^{n_j} \sqrt{2}^{\left(2-\delta_{m_f0}-\delta_{m_j0}\right)}$$

$$* \int_0^\infty \left|\vec{\tilde{\kappa}}\right| W_{\Phi_m}\left(\left|\vec{\tilde{\kappa}}_1\right|\right) \frac{J_{n_f+1}\left(2\pi\left|\vec{\tilde{\kappa}}_2\right|\right)}{\pi\left|\vec{\tilde{\kappa}}_2\right|} \frac{J_{n_j+1}\left(2\pi\left|\vec{\tilde{\kappa}}_3\right|\right)}{\pi\left|\vec{\tilde{\kappa}}_3\right|} \int_{\tilde{\theta}_\alpha}^{\tilde{\theta}_\alpha+2\pi} e^{-j2\pi\left|\vec{\tilde{\kappa}}_1\right|\left|\vec{\alpha}\right|\cos\left(\tilde{\theta}_1-\theta_\alpha\right)}$$

$$* \cos\left\{m_f\tilde{\theta}_3 + \frac{\pi}{4}\left(1-\delta_{m_f0}\right)\left[(-1)^f-1\right]\right\} \cos\left\{m_j\tilde{\theta}_2 + \frac{\pi}{4}\left(1-\delta_{m_j0}\right)\left[(-1)^j-1\right]\right\} d\tilde{\theta}d\left|\vec{\tilde{\kappa}}\right| . \quad (93)$$

Unfortunately, there is not a readily available closed-form solution to the integral

over $\tilde{\theta}$. The closed form is essential for the real-time applicability of this work. Without

performing the integration over $\tilde{\theta}$, numerical double integrations would be required in

real time. Since the turbulence-induced wavefront deformations change relatively quickly

and the system must be updated at speeds commensurate with these changes, on-line

numerical double integrations are not feasible. However, single integrations are

acceptable and hence it is desirable to integrate out the $\tilde{\theta}$ dependence. Therefore, to aid

in the evaluation of the integral over $\tilde{\theta}$, two additional assumptions are now introduced.

The two assumptions are as follows:

$$1. \; \gamma(t_1) \approx 0° \quad \text{and} \quad 2. \; \Delta t \ll 1 \; \text{sec}. \quad (94)$$

Recall that $\gamma(t_1)$ is the angle from the plane of the aperture to the turbulent layer at time t_1.

The first assumption can be justified by noticing that the layered turbulence model

requires $\gamma(t_1) \approx 0°$. This would correspond to the classical situation of an optical imaging

system. Clearly, $\gamma(t_1) \approx 90°$ is not a practical physical situation since the propagation

paths would always lie within a single layer. The second assumption comes from the

prediction of correlation times on the order of tenths of milliseconds. With these

assumptions, it can be seen, using eqs. (31) and (35) that

$$\theta(t_1) \approx \theta(t_2) \Rightarrow \gamma(t_2) \approx \gamma(t_1) \Rightarrow \gamma(t_2) \approx 0^\circ. \tag{95}$$

Also, using eqs. (53)-(59), (89), and (94), it is found that

$$A_{x1,1} = A_{x2,2} \quad \text{and} \quad A_{u1,1} = A_{u2,2}. \tag{96}$$

Therefore, after some manipulation, the integral over $\tilde{\theta}$ in eq. (93) reduces to

$$\text{INT}_{\tilde{\theta}} = \frac{1}{2} \int_{\theta_\alpha}^{\theta_\alpha + 2\pi} e^{-j2\pi|\vec{\kappa}_1||\vec{\alpha}|\cos(\tilde{\theta}-\theta_\alpha)} \left[\cos\left\{ (m_f + m_j)\tilde{\theta} + g \right\} + \cos\left\{ (m_f - m_j)\tilde{\theta} + h \right\} \right] d\tilde{\theta} \tag{97}$$

where

$$g = \left\{ \frac{\pi}{4} \left\{ \left(1 - \delta_{m_f 0}\right)\left[(-1)^f - 1\right] + \left(1 - \delta_{m_j 0}\right)\left[(-1)^j - 1\right] \right\} \right\} \tag{98}$$

and

$$h = \left\{ \frac{\pi}{4} \left\{ \left(1 - \delta_{m_f 0}\right)\left[(-1)^f - 1\right] - \left(1 - \delta_{m_j 0}\right)\left[(-1)^j - 1\right] \right\} \right\}. \tag{99}$$

By a change of variables, a trigonometric identity, and the definition for a Bessel function

of the first kind [9], denoted by $J_*(\bullet)$, it is found that

$$\text{INT}_{\tilde{\theta}} = \cos\left\{ (m_f + m_j)\theta_\alpha + g \right\} \pi(-1)^{\frac{3(m_f + m_j)}{2}} J_{(m_f + m_j)}\left(2\pi|\vec{\kappa}_1||\vec{\alpha}|\right)$$

$$+ \cos\left\{ (m_f - m_j)\theta_\alpha + h \right\} \pi(-1)^{\frac{3(m_f - m_j)}{2}} J_{|m_f - m_j|}\left(2\pi|\vec{\kappa}_1||\vec{\alpha}|\right). \tag{100}$$

The details of integrating eq. (97) are shown in Appendix A. Therefore, the expression

for the correlation between Zernike polynomial phase expansion coefficients becomes

$$\Gamma_{a_f^{(i,o)}(t_1)a_j^{(i,o)}(t_2)} = \sum_m \frac{1}{c\gamma(t_1)c\gamma(t_2)} \frac{R^2}{L(t_1)L(t_2)\pi} |\det(\mathbf{A}_x)| |\det(\mathbf{A}_u)| \{(n_f+1)(n_j+1)\}^{\frac{1}{2}} (-1)^{\frac{n_f+n_j}{2}} (-1)^{n_j} \sqrt{2}^{(2-\delta_{m_f 0}-\delta_{m_j 0})}$$

$$* \int_0^\infty |\vec{\kappa}| W_{\Phi_m}(|\vec{\kappa}_1|) \frac{J_{n_f+1}(2\pi|\vec{\kappa}_2|)}{|\vec{\kappa}_2|} \frac{J_{n_j+1}(2\pi|\vec{\kappa}_3|)}{|\vec{\kappa}_3|} * \left[\cos\{(m_f+m_j)\theta_\alpha + g\}(-1)^{\frac{3(m_f+m_j)}{2}} J_{(m_f+m_j)}(2\pi|\vec{\kappa}_1||\vec{\alpha}|) \right.$$

$$\left. + \cos\{(m_f-m_j)\theta_\alpha + h\}(-1)^{\frac{3(m_f-m_j)}{2}} J_{|m_f-m_j|}(2\pi|\vec{\kappa}_1||\vec{\alpha}|) \right] d|\vec{\kappa}| . \qquad (101)$$

The final component of eq. (101) that must be specified is the power spectrum. In this work, the von Karman spectrum, eq. (13), is used and with a weighted turbulence-dependent layer model can be expressed as

$$W_{\Phi_m}(\kappa,\zeta_m) = \frac{\sqrt{3}\,\Gamma\!\left(\frac{8}{3}\right)}{2(2\pi)^{\frac{8}{3}}} \left(\frac{6.88}{2.91}\right) w_m r_o^{\frac{-5}{3}} \left(\kappa^2 + \kappa_o^2\right)^{-11/6} . \qquad (102)$$

Using eq. (102) in eq. (101) produces the final result:

$$\Gamma_{a_f^{(i,o)}(t_1)a_j^{(i,o)}(t_2)} = \sum_m \frac{1}{c\gamma(t_1)c\gamma(t_2)} \frac{R^2}{L(t_1)L(t_2)\pi} |\det(\mathbf{A}_x)| |\det(\mathbf{A}_u)| \{(n_f+1)(n_j+1)\}^{\frac{1}{2}} (-1)^{\frac{n_f+n_j}{2}} (-1)^{n_j} \sqrt{2}^{(2-\delta_{m_f 0}-\delta_{m_j 0})} \frac{\sqrt{3}\,\Gamma\!\left(\frac{8}{3}\right)}{2(2\pi)^{\frac{8}{3}}}$$

$$* \left(\frac{6.88}{2.91}\right) w_m r_o^{\frac{-5}{3}} \int_0^\infty |\vec{\kappa}| \left(|\vec{\kappa}_1|^2 + \kappa_o^2\right)^{\frac{-11}{6}} \frac{J_{n_f+1}(2\pi|\vec{\kappa}_2|)}{|\vec{\kappa}_2|} \frac{J_{n_j+1}(2\pi|\vec{\kappa}_3|)}{|\vec{\kappa}_3|} * \left[\cos\{(m_f+m_j)\theta_\alpha + g\}(-1)^{\frac{3(m_f+m_j)}{2}} J_{(m_f+m_j)}(2\pi|\vec{\kappa}_1||\vec{\alpha}|) \right.$$

$$\left. + \cos\{(m_f-m_j)\theta_\alpha + h\}(-1)^{\frac{3(m_f-m_j)}{2}} J_{|m_f-m_j|}(2\pi|\vec{\kappa}_1||\vec{\alpha}|) \right] d|\vec{\kappa}| . \qquad (103)$$

4.3 Calculations

Now that the analysis has been set into place, the correlation functions for the first few combinations of Zernike polynomials will be determined. These calculations are performed by numerically integrating eq. (103) over the spatial frequency vector.

The following scenario, similar to that used by Whiteley, et. al. [35, 36] is

considered: one turbulent layer is used and is placed a distance of 25,000 meters from the

aperture at time t_1. The geometry is shown in Figure 16 and the engagement parameters

are as follows:

$$\vec{V}_A = \begin{bmatrix} 300 & 0 & 0 \end{bmatrix}^T, \vec{V}_T = \begin{bmatrix} 0 & 0 & 0 \end{bmatrix}^T, \vec{V}_W = \begin{bmatrix} 0 & 0 & 0 \end{bmatrix}^T$$
$$L_2(t_1) = 50,000, L_T(t_1) = 1, \gamma(t_1) = 0°, R = 0.875$$

(104)

where the velocity and distance units are meters/sec and meters, respectively.
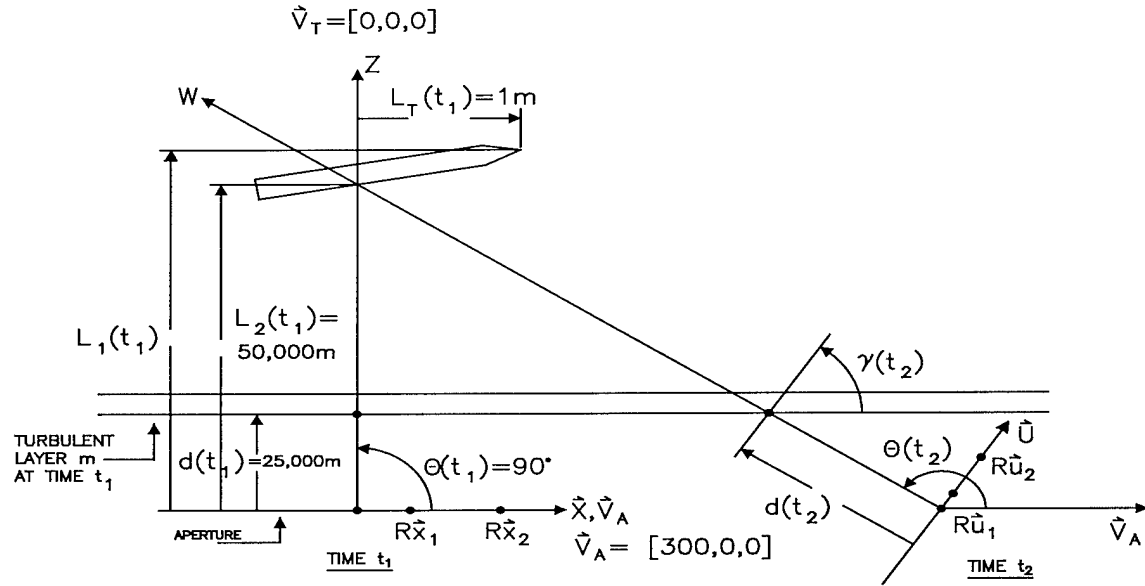
Figure 16. Engagement geometry for calculations.

For the simulations and modeling to follow, two Zernike modes (tilts) are used to

approximate the wavefront phases. This number may seem quite small, however, the

order of the linear, stochastic, dynamical system modeling the atmosphere (plant) that is

derived from these correlations is two times the number of Zernike modes used for each

wavefront expansion. Thus, if more Zernike modes were used, the order of the system would increase to the point that advanced control concepts would be difficult to apply in an on-line application as required in adaptive optics. The Zernike modes used in this case are $Z_2(\bar{x})$ and $Z_3(\bar{x})$. These modes represent wavefront tilt at the aperture. Tilt can be described as the least squares sense best fit to the aperture phase. It is an important component of wavefront expansions since x- and y-tilts represent about 87% of the power in the phase fluctuations [23]. The first Zernike mode, $Z_1(\bar{x})$, is termed piston and represents the aperture averaged wavefront phase. Piston is not a distortive contributor and is not considered in any calculations.

The following notation, as introduced in Chapter 3, has been adopted to represent the Zernike polynomial phase expansion coefficients: $a_n^{(i)}$, $a_n^{(o)}$ are Zernike coefficient n, (n = 2, 3), of the inbound (i) and outbound (o) wavefronts. Using two Zernike modes, there are ten correlation functions of interest. To see this, consider the stacked vector which contains the Zernike expansion coefficients:

$$\mathbf{a}^{(a)}(t) = \begin{bmatrix} a_2^{(i)}(t) & a_3^{(i)}(t) & a_2^{(o)}(t) & a_3^{(o)}(t) \end{bmatrix}^{\mathrm{T}} \tag{105}$$

where the superscript 'a' implies atmosphere. Integration of eq. (103) will yield the correlation kernel function of the vector in eq. (105) which can be expressed as

$$E\{\mathbf{a}^{(a)}(t)\mathbf{a}^{(a)}(t+\tau)^{\mathrm{T}}\} = \begin{bmatrix} E\{a_2^{(i)}a_2^{(i)}\} & E\{a_2^{(i)}a_3^{(i)}\} & E\{a_2^{(i)}a_2^{(o)}\} & E\{a_2^{(i)}a_3^{(o)}\} \\ E\{a_2^{(i)}a_3^{(i)}\} & E\{a_3^{(i)}a_3^{(i)}\} & E\{a_3^{(i)}a_2^{(o)}\} & E\{a_3^{(i)}a_3^{(o)}\} \\ E\{a_2^{(i)}a_2^{(o)}\} & E\{a_3^{(i)}a_2^{(o)}\} & E\{a_2^{(o)}a_2^{(o)}\} & E\{a_2^{(o)}a_3^{(o)}\} \\ E\{a_2^{(i)}a_3^{(o)}\} & E\{a_3^{(i)}a_3^{(o)}\} & E\{a_2^{(o)}a_3^{(o)}\} & E\{a_3^{(o)}a_3^{(o)}\} \end{bmatrix} \tag{106}$$

where $\tau = \Delta t = t_{j+1} - t_j$. This matrix is symmetric, thus only the diagonal and upper or lower diagonal terms need be calculated. Hence, there are ten correlation functions to be

determined. Figures 17-21 show the correlation functions which are the result of integrating eq. (103) using the parameters displayed in Figure 16.
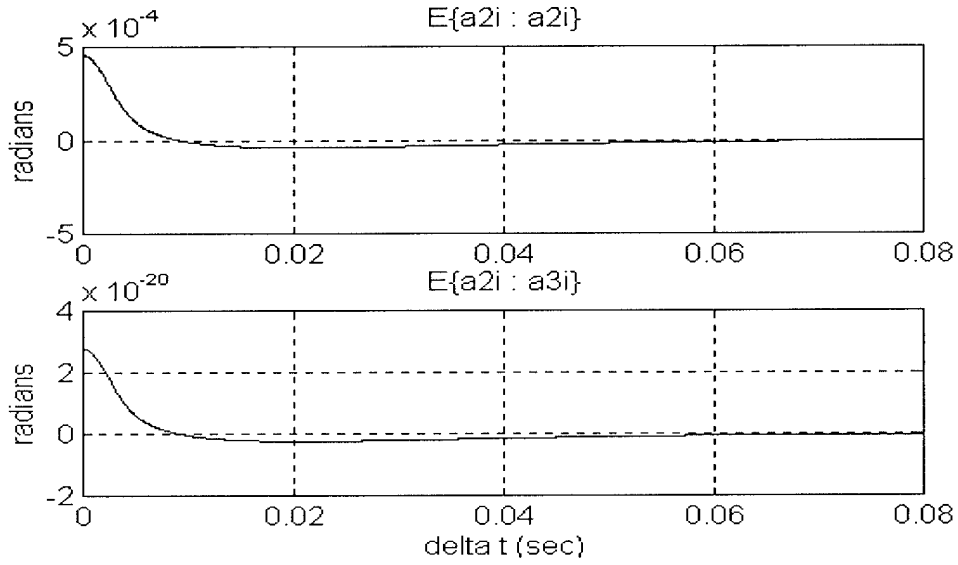
Figure 17. $E\left\{a_2^{(i)}a_2^{(i)}\right\}$ and $E\left\{a_2^{(i)}a_3^{(i)}\right\}$ versus Δt.
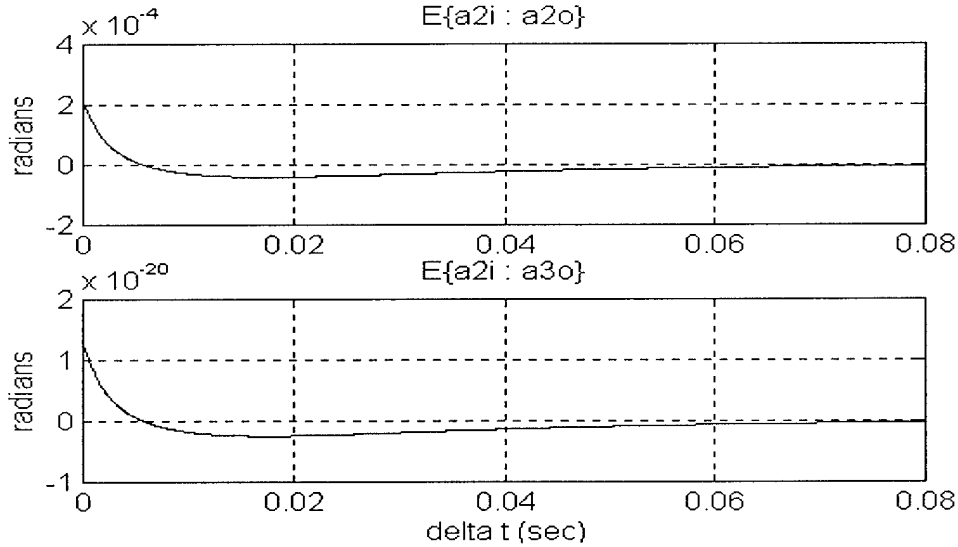
Figure 18. $E\left\{a_2^{(i)}a_2^{(o)}\right\}$ and $E\left\{a_2^{(i)}a_3^{(o)}\right\}$ versus Δt.

63
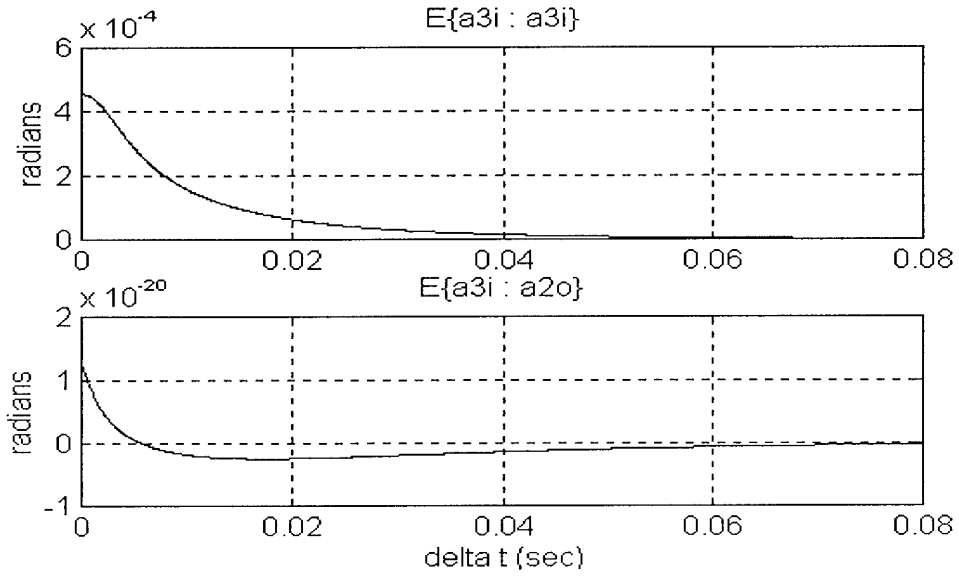
Figure 19. $E\left\{a_3^{(i)}a_3^{(i)}\right\}$ and $E\left\{a_3^{(i)}a_2^{(o)}\right\}$ versus Δt.
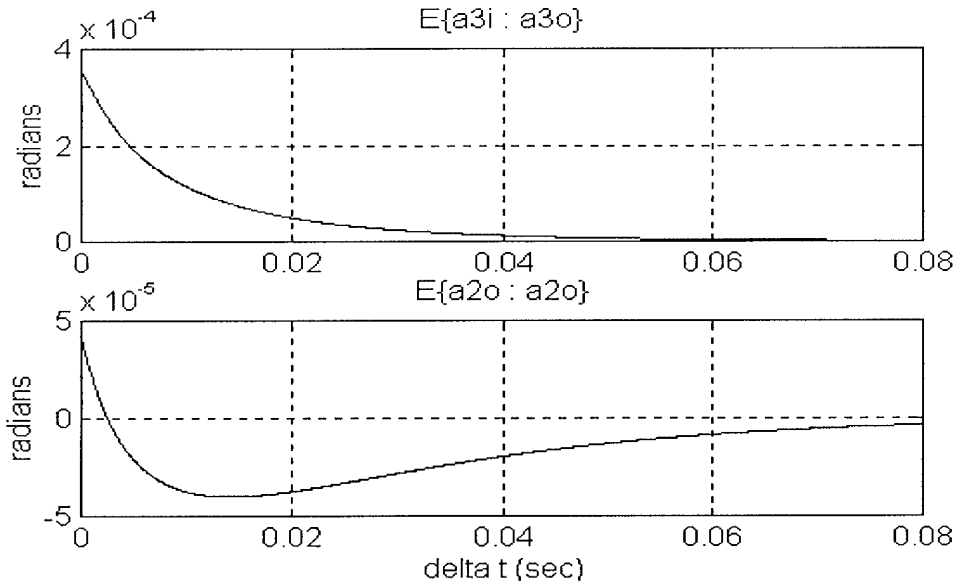
Figure 20. $E\left\{a_3^{(i)}a_3^{(o)}\right\}$ and $E\left\{a_2^{(o)}a_2^{(o)}\right\}$ versus Δt.
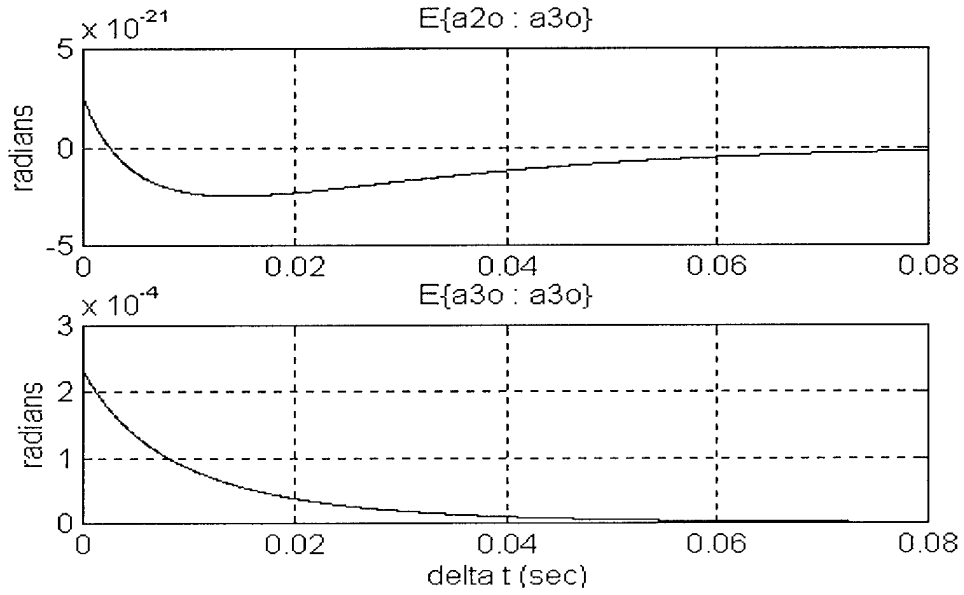
Figure 21. $E\left\{a_2^{(o)'}a_3^{(o)}\right\}$ and $E\left\{a_3^{(o)'}a_3^{(o)}\right\}$ versus Δt.

As can be seen from these figures, four of the correlations are at least fifteen orders of magnitude less than the others. Therefore, $E\left\{a_2^{(i)'}a_3^{(i)}\right\}$, $E\left\{a_2^{(i)'}a_3^{(o)}\right\}$, $E\left\{a_3^{(i)'}a_2^{(o)}\right\}$, and $E\left\{a_2^{(o)'}a_3^{(o)}\right\}$ will be set to zero in the upcoming work. Now that the calculations are in place, it is necessary to realize an underlying linear, stochastic, dynamical system which has correlations that are representative of those in Figure 17-21. The next section addresses this task.

4.4 Stochastic Modeling

Since the correlation functions calculated in Section 4.3 are due to the turbulent atmosphere, the linear, stochastic, dynamical system to be derived will in turn be a model

of the atmosphere, i.e., the plant. Due to the random nature of the atmosphere, this model

will be stochastic. Let the linear system to be identified be represented by [16]

$$da^{(a)}(t) = F_a a^{(a)}(t)dt + G_a dB_a(t) \tag{107}$$

where $B_a(t)$ is Brownian motion with statistics $E\{B_a(t)\} = 0$ and

$$E\left\{[B_a(t) - B_a(t')][B_a(t) - B_a(t')]^T\right\} = \int_t^{t'} Q_a(\tau)d\tau = \int_t^{t'} I \, d\tau \tag{108}$$

for all $t \geq t'$, I is the identity matrix, and F_a, G_a have the following forms:

$$F_a = \begin{bmatrix} f_{11} & f_{12} & f_{13} & f_{14} \\ f_{21} & f_{22} & f_{23} & f_{24} \\ f_{31} & f_{32} & f_{33} & f_{34} \\ f_{41} & f_{42} & f_{43} & f_{44} \end{bmatrix}, \quad G_a = \begin{bmatrix} g_{11} & g_{12} \\ g_{21} & g_{22} \\ g_{31} & g_{32} \\ g_{41} & g_{42} \end{bmatrix}. \tag{109}$$

The dimensionality of F_a was determined by the number of states in the state vector, i.e.,

$a^{(a)}(t) = \begin{bmatrix} a_2^{(i)}(t) & a_3^{(i)}(t) & a_2^{(o)}(t) & a_3^{(o)}(t) \end{bmatrix}$. The four element state vector contains the x-

and y-tilt Zernike expansion coefficients of the inbound and outbound wavefronts. Tilts

were used since they contain most of the power in the wavefront aberrations. Higher

order modes can be used, but their inclusion does not significantly improve the developed

model. G_a was selected as a 4-by-2 matrix through iterative testing. It was desired that

the realized system's correlation kernel functions accurately represent those which were

calculated. In this case, a 4-by-2 input noise matrix sufficed. Notice that in eq. (108), the

diffusion of $B_a(t)$ was set to I. This simply eliminates one of the design parameters and

allows system identification to be performed with more ease. Also, it can be seen that eq.

(107) lacks a $Bu(t)dt$ term. This is due to the obvious fact that the atmosphere is

uncontrollable.

Using eq. (107), the correlation kernel matrix of the state process, denoted $\mathbf{P}_a(t,\tau)$, satisfies

$$E\left\{\mathbf{a}^{(a)}(t)\mathbf{a}^{(a)}(t+\tau)^{T}\right\} = \mathbf{P}_a(t,t+\tau) \tag{110}$$

where

$$\mathbf{P}_a(t,t+\tau) = \mathbf{P}_a(t)e^{\mathbf{F}_a^{T}\tau}, \ \tau \geq 0 \tag{111}$$

and $\mathbf{P}_a(t)$ is the correlation matrix. Taking the derivative of eq. (111) with respect to τ and manipulating yields

$$\frac{\partial \mathbf{P}_a(t,t+\tau)}{\partial \tau} = \mathbf{P}_a(t)e^{\mathbf{F}_a^{T}\tau}\mathbf{F}_a^{T} = \mathbf{P}_a(t,t+\tau)\mathbf{F}_a^{T}. \tag{112}$$

Equation (112) is needed to obtain the system matrix. The calculations in Section 4.3 provide the correlation kernel matrix. The derivative of this matrix, with respect to τ, can then be obtained. Hence, the only unknown in eq. (112) is the system matrix. Therefore, using the correlation data in Section 4.3 and eq. (112), the system matrix, $\mathbf{F}_a$, can be identified. In order to obtain the input matrix, $\mathbf{G}_a$, consider the correlation of the state process which satisfies the following differential equation:

$$\dot{\mathbf{P}}_a(t) = \mathbf{F}_a\mathbf{P}_a(t) + \mathbf{P}_a(t)\mathbf{F}_a^{T} + \mathbf{G}_a\mathbf{I}\mathbf{G}_a^{T}. \tag{113}$$

Letting $t \rightarrow \infty$ while maintaining a fixed separation between t and $t + \tau$, which is the steady-state case and produces a stationary process, provides

$$\dot{\mathbf{P}}_a(t) = 0 = \mathbf{F}_a\mathbf{P}_{a_{ss}}(t) + \mathbf{P}_{a_{ss}}(t)\mathbf{F}_a^{T} + \mathbf{G}_a\mathbf{I}\mathbf{G}_a^{T} \tag{114}$$

67

where the subscript 'ss' implies steady-state. $P_{a_{ss}}(t)$ is found from the calculated correlation kernel data by letting $\tau = 0$. Then, G_a can be determined by taking the Cholesky decomposition [16] of

$$G_a G_a^T = -\left(F_a P_{a_{ss}}(t) + P_{a_{ss}}(t)F_a^T\right). \tag{115}$$

After performing the computations, the atmospheric model becomes

$$da^{(a)}(t) = \begin{bmatrix} -410.35 & 0 & 420 & 0 \\ 0 & -437.47 & 0 & 464.41 \\ -207.88 & 0 & 199.75 & 0 \\ 0 & -186.53 & 0 & 165.59 \end{bmatrix} a^{(a)}(t)dt + \begin{bmatrix} .4445 & 0 \\ 0 & .2687 \\ .27 & 0 \\ 0 & .2516 \end{bmatrix} dB_a(t)$$

$$= F_a a^{(a)}(t) + G_a dB_a(t). \tag{116}$$

By computing the eigenvalues of the F_a matrix, namely, -29.48, -70.39, -181.12, and -201.48, it can be seen that the system is stable. Figures 22-24 show the nonzero correlation functions from the calculations in Section 4.3 with those from the atmospheric model in eq. (116) superimposed. These three figures convey the fact that the model does provide a good representation of the calculated correlation functions. However, there is some modeling error. It would appear that using more Zernike modes in the wavefront expansions would provide a better representation of the calculated correlation functions. In fact, using 5 Zernike modes in the wavefront expansions was investigated. Although the accuracy did improve with more modes, the modeling error was consistently present. There is a trade-off between modeling accuracy and computation time. More modes increases accuracy, at the expense of increased computational delays. Since the modeling error decreased only slightly with more modes, the decision was made to use tilts (two modes) in the wavefront expansions.
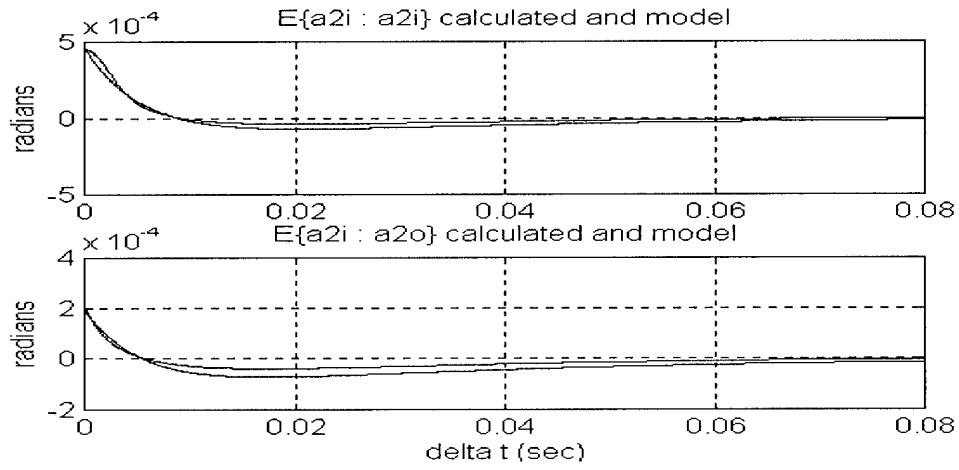
Figure 22. $E\left\{a_2^{(i)}a_2^{(i)}\right\}$ and $E\left\{a_2^{(i)}a_2^{(o)}\right\}$, calculated and model versus Δt.
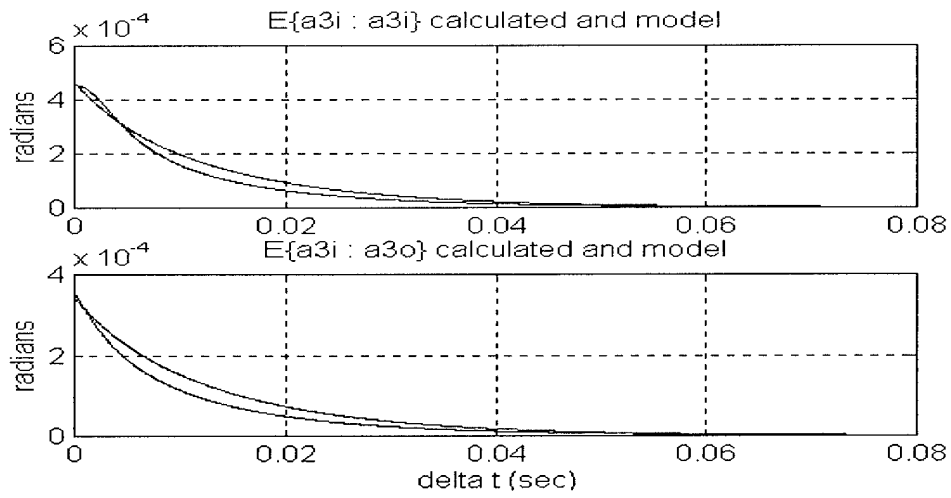
Figure 23. $E\left\{a_3^{(i)}a_3^{(i)}\right\}$ and $E\left\{a_3^{(i)}a_3^{(o)}\right\}$, calculated and model versus Δt.
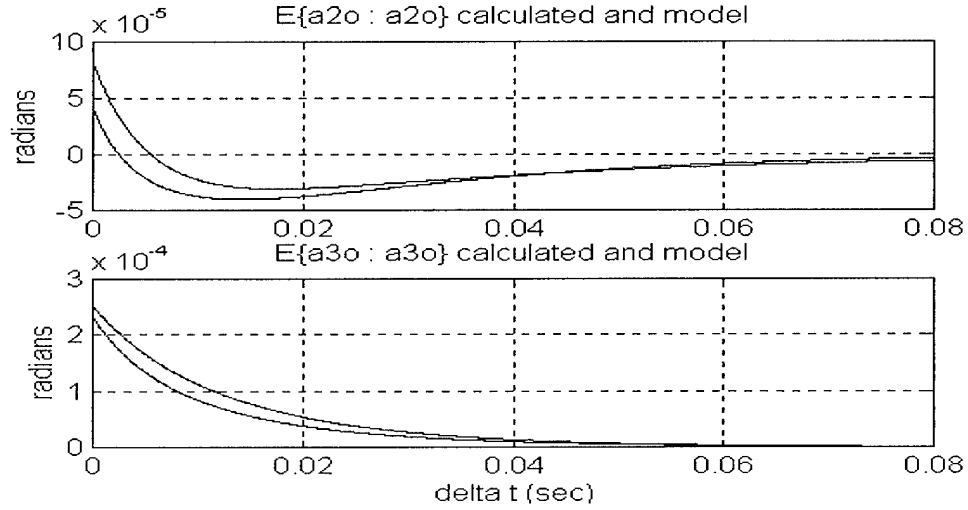
Figure 24. $E\{a_2^{(o)}a_2^{(o)}\}$ and $E\{a_3^{(o)}a_3^{(o)}\}$, calculated and model versus Δt.

One final point concerning the Zernike phase expansion coefficients. According

to Noll [18], these coefficients are well modeled as zero-mean, Gaussian random

variables. They are zero-mean because the wavefront phases, $\Phi^{(i)}(R\vec{x}_1,t_1)$,

$\Phi^{(i)}(R\vec{u}_1,t_2)$, $\Phi^{(o)}(R\vec{x}_2,t_1)$, and $\Phi^{(o)}(R\vec{u}_2,t_2)$ are the deviation of the phase from the

ideal, or unperturbed wavefront. Gaussianness is the result of the wavefront phases being

the sum of a large number of random variables. The Central Limit Theorem [3] then

states that the phases will be Gaussian.

4.5 Summary

At this point, the correlation between Zernike polynomial expansion coefficients

has been determined. Using these correlations, a state-space model of the atmosphere

was constructed. In order to characterize the AO control system fully, a model of the

mirror must be developed and an output equation must be specified. The next chapter

addresses the mirror and complete models.

V. Deformable Mirror and Complete Models

5.1 Introduction

In the upcoming work, a model for the deformable mirror is derived. The deformable mirror (DM) currently used has a continuous mirror surface worked by 49 actuators. It will be assumed that all actuators can be driven by control voltages, i.e., there are no slave actuators. Actuator linearity is also assumed which implies that the graph of actuator displacement versus applied control voltage is a straight line. Additionally, the deformable mirror is a linear device. In this case, inter-actuator superposition holds. For example, if a voltage is applied to actuator 1 and the mirror's response is measured, then a control voltage is applied to actuator 2, the sum of the two responses would be equivalent to applying the voltages simultaneously. After completing the mirror modeling, the complete system will be formed by appending the mirror and atmospheric models. Output equations for the system, that is, measurements of the inbound and reflected wavefronts, will be covered. Lastly, the continuous-time system will be converted to an equivalent discrete-time system for implementation in a digital computer.

5.2 Steady-State Mirror Behavior

In this section, it is desired to determine the relation between applied control voltages and the mirror's behavior. The term steady-state implies that a finite time has elapsed since the last occurrence of a control voltage, i.e., the mirror is not deforming.

The analysis used to determine the mirror model and output equations follows the derivation in the work of Von Bokern, et. al. [32] and Von Bokern [33]. However, the determination of some of the required matrices, as detailed in Appendix B, are specific to this work. This is due to the functions chosen to represent certain parameters, as will be shown.

To begin the derivation, consider the HEL beam. The HEL wavefront, prior to reaching the DM, is planar and in phase. For a section of the DM that has not been actuated, the change in Optical Path Lengths (OPL) is zero. However, there is a decrease in the OPL for a section of the DM that has moved. This decreased OPL causes the reflected light's path length to be decreased by two times the change in OPL. Thus, the absolute phase of the reflected wavefront, corresponding to a section of the DM that has been actuated, is larger than for a section of the DM that has not moved. Since the incident HEL wavefront is planar, any phase distortion in the reflected image will be solely due to the DM's shape.

To determine the steady-state behavior of the mirror, influence functions will be used. Influence functions represent the effect of a single actuator voltage on the mirror shape and manifest themselves in differences in OPL for the HEL. Utilizing the influence functions and the fact that there are in general n_A actuators, the DM's shape can be represented by

$$\Phi^{(m)}(\vec{x}) = \sum_{k=1}^{n_A} I_k(\vec{x}) v_{ak} \tag{117}$$

73

where $\bar{x}$ is a spatial location on the DM, $I_k(\bar{x})$ is the kth influence function, and v_{ak} is the control voltage applied to the kth actuator. Now, the reflected wavefront's phase distortion, excluding piston, is given by

$$\Phi^{(m)}(\bar{x}) = \sum_{k=1}^{n_A} I_k(\bar{x})v_{ak} - E\left[\sum_{k=1}^{n_A} I_k(\bar{x})v_{ak}\right] \tag{118}$$

where the expected value term, $E[\bullet]$, is piston and the superscript 'm' implies the mirror.

The reflected wavefront can also be written as a linear combination of Zernike polynomials, that is,

$$\Phi^{(m)}(\bar{x},t) = \sum_i a_i^{(m)}(t)Z_i(\bar{x}) \tag{119}$$

where $a_i^{(m)}(t)$ are the Zernike polynomial phase expansion coefficients associated with the mirror. As shown in Chapter 2, the mirror expansion coefficients are given by

$$a_i^{(m)}(t) = \int W(\bar{x})Z_i(\bar{x})\Phi^{(m)}(\bar{x},t)d\bar{x}. \tag{120}$$

Substituting the reflected wavefront's phase distortion, eq. (118), into the above equation yields

$$a_i^{(m)}(t) = \int W(\bar{x})Z_i(\bar{x})\left\{\sum_{k=1}^{n_A} I_k(\bar{x})v_{ak} - E\left[\sum_{k=1}^{n_A} I_k(\bar{x})v_{ak}\right]\right\}d\bar{x}$$

$$= \int W(\bar{x})Z_i(\bar{x})\sum_{k=1}^{n_A} I_k(\bar{x})v_{ak}d\bar{x} - \int W(\bar{x})Z_i(\bar{x})E\left[\sum_{k=1}^{n_A} I_k(\bar{x})v_{ak}\right]d\bar{x}. \tag{121}$$

Notice that the second term is the product of piston and a non-piston Zernike polynomial. Using the orthogonality property of the Zernike polynomials shows that the second term is identically zero. Thus,

$$a_i^{(m)}(t) = \int W(\bar{x})Z_i(\bar{x})\sum_{k=1}^{n_A} I_k(\bar{x})v_{ak}\,d\bar{x}$$

$$= \sum_{k=1}^{n_A}\left[\int W(\bar{x})Z_i(\bar{x})I_k(\bar{x})\,d\bar{x}\right]v_{ak}$$

$$= \mathbf{m}_i^T \mathbf{v}_a \tag{122}$$

where

$$\mathbf{m}_i^T = \left[\int W(\bar{x})Z_i(\bar{x})I_1(\bar{x})\,d\bar{x} \quad \int W(\bar{x})Z_i(\bar{x})I_2(\bar{x})\,d\bar{x} \quad \cdots \quad \int W(\bar{x})Z_i(\bar{x})I_{n_A}(\bar{x})\,d\bar{x}\right] \tag{123}$$

and

$$\mathbf{v}_a = \begin{bmatrix} v_{a1} & v_{a2} & \cdots & v_{an_A} \end{bmatrix}^T. \tag{124}$$

Therefore,

$$\begin{aligned} a_2^{(m)}(t) &= \mathbf{m}_2^T \mathbf{v}_a \\ a_3^{(m)}(t) &= \mathbf{m}_3^T \mathbf{v}_a \\ &\vdots \\ a_{n+1}^{(m)}(t) &= \mathbf{m}_{n+1}^T \mathbf{v}_a \end{aligned} \quad \Rightarrow \mathbf{a}^{(m)}(t) = \mathbf{M}\,\mathbf{v}_a \tag{125}$$

where $\mathbf{m}_i^T$ has size 1 x n_A, $\mathbf{v}_a$ has size n_A x 1, and $\mathbf{M}$ is n x n_A where n is the number of

Zernike modes used in the expansion and n_A is the number of actuators. In physical

terms, the matrix $\mathbf{M}$ can be considered the steady-state influence function matrix since it

relates control voltages to the steady-state influence of the mirror. Complete specification

of matrix $\mathbf{M}$ can be found in Appendix B.

5.3 Actuator Dynamics

Now that the steady-state behavior of the mirror has been considered, it is

necessary to model its transient behavior. Piezoelectric actuators, used in the

construction of deformable mirrors, can be modeled as first-order, linear, time-invariant, deterministic systems [33]. Thus, the dynamics equation for the displacement of an actuator can be modeled by the scalar equation

$$\dot{\delta}(t) = \frac{-1}{\tau_a}\delta(t) + bu(t) \tag{126}$$

where u(t) is the command signal (voltage) applied to the actuator, $\delta(t)$ is the path length decrease, and τ_a, b are free parameters to be determined by empirical data. In fact, τ_a is the time constant of the actuators. Under the assumption that all actuators behave in the same manner, n_A equations identical to the above would be written. As discussed earlier, the states in this case, $\delta(t)$, are the 2-way decrease in path length since the light is reflected from the mirror.

Now, it is desired to formulate the dynamics of the mirror in the form

$$\dot{\mathbf{a}}^{(m)}(t) = \mathbf{F}_m \mathbf{a}^{(m)}(t) + \mathbf{B}_m \mathbf{u}(t) \tag{127}$$

where $\mathbf{a}^{(m)}(t) = \begin{bmatrix} a_2^{(m)}(t) & a_3^{(m)}(t) & \cdots & a_{n+1}^{(m)}(t) \end{bmatrix}^T$ and $\mathbf{F}_m$, $\mathbf{B}_m$ are the dynamics and control input matrices, respectively. Since all actuators have the same dynamics equation, the entire mirror exhibits dynamic behavior with a time constant of τ_a. Thus, the mirror's contribution to the phase distortion of the reflected image [33], denoted by $\Phi^{(m)}(\vec{x}, t)$, can be written as

$$\dot{\Phi}^{(m)}(\vec{x}, t) = \frac{-1}{\tau_a}\Phi^{(m)}(\vec{x}, t) + \mathbf{b}_m^T(\vec{x})\mathbf{u}(t) \tag{128}$$

where $\mathbf{b}_m^T(\vec{x})$ maps control voltages to the rate of change of phase at spatial location $\vec{x}$.

Zernike polynomials can also be used to write

76

$$\Phi^{(m)}(\vec{x}, t) = \sum_i a_i^{(m)}(t) Z_i(\vec{x}). \tag{129}$$

Taking the time derivative of the above equation yields

$$\dot{\Phi}^{(m)}(\vec{x}, t) = \sum_i \dot{a}_i^{(m)}(t) Z_i(\vec{x}). \tag{130}$$

Substituting eqs. (129) and (130) into eq. (128) produces

$$\dot{a}_2^{(m)}(t) Z_2(\vec{x}) + \dot{a}_3^{(m)}(t) Z_3(\vec{x}) + \cdots + \dot{a}_{n+1}^{(m)}(t) Z_{n+1}(\vec{x})$$

$$= \frac{-1}{\tau_a} \left[a_2^{(m)}(t) Z_2(\vec{x}) + a_3^{(m)}(t) Z_3(\vec{x}) + \cdots + a_{n+1}^{(m)}(t) Z_{n+1}(\vec{x}) \right] + \mathbf{b}_m^T(\vec{x}) \mathbf{u}(t). \tag{131}$$

In more compact notation, eq. (131) becomes

$$\sum_{i=2}^{n+1} \dot{a}_i^{(m)}(t) Z_i(\vec{x}) = \frac{-1}{\tau_a} \sum_{i=2}^{n+1} a_i^{(m)}(t) Z_i(\vec{x}) + \sum_{j=1}^{n_A} b_j(\vec{x}) u_j(t) \tag{132}$$

where $b_j(\vec{x}), u_j(t)$ are the jth components of $\mathbf{b}_m^T(\vec{x}), \mathbf{u}(t)$, respectively. Multiplying the

above equation by $W(\vec{x}) Z_2(\vec{x})$ and integrating over the area of the mirror yields

$$\int \sum_{i=2}^{n+1} \dot{a}_i^{(m)}(t) Z_i(\vec{x}) W(\vec{x}) Z_2(\vec{x}) d\vec{x} = \frac{-1}{\tau_a} \int \sum_{i=2}^{n+1} a_i^{(m)}(t) Z_i(\vec{x}) W(\vec{x}) Z_2(\vec{x}) d\vec{x} + \int \sum_{j=1}^{n_A} b_j(\vec{x}) u_j(t) W(\vec{x}) Z_2(\vec{x}) d\vec{x}.$$

$$\tag{133}$$

Utilizing the orthogonality property of Zernike polynomials produces

$$\dot{a}_2^{(m)}(t) = \frac{-1}{\tau_a} a_2^{(m)}(t) + \mathbf{r}_2^T \mathbf{u}(t). \tag{134}$$

Performing the same procedure for $Z_3(\vec{x}), \cdots, Z_{n+1}(\vec{x})$ gives

$$\dot{a}_2^{(m)}(t) = \frac{-1}{\tau_a}a_2^{(m)}(t) + \mathbf{r}_2^T\mathbf{u}(t)$$

$$\dot{a}_3^{(m)}(t) = \frac{-1}{\tau_a}a_3^{(m)}(t) + \mathbf{r}_3^T\mathbf{u}(t) \tag{135}$$

$$\vdots$$

$$\dot{a}_{n+1}^{(m)}(t) = \frac{-1}{\tau_a}a_{n+1}^{(m)}(t) + \mathbf{r}_{n+1}^T\mathbf{u}(t)$$

where it can be seen, from eqs. (133) and (134), that

$$\mathbf{r}_i^T = \left[\int b_1(\bar{x})W(\bar{x})Z_i(\bar{x})d\bar{x} \quad \int b_2(\bar{x})W(\bar{x})Z_i(\bar{x})d\bar{x} \quad \cdots \quad \int b_{n_A}(\bar{x})W(\bar{x})Z_i(\bar{x})d\bar{x}\right] \tag{136}$$

and

$$\mathbf{u}(t) = \left[u_1(t) \quad u_2(t) \quad \cdots \quad u_{n_A}(t)\right]^T. \tag{137}$$

Thus,

$$\dot{\mathbf{a}}^{(m)}(t) = \mathbf{DIAG}\left(\frac{-1}{\tau_a}\right)\mathbf{a}^{(m)}(t) + \mathbf{r}^T\mathbf{u}(t) \tag{138}$$

where $\mathbf{DIAG}(-1/\tau_a)$ is a diagonal matrix with $(-1/\tau_a)$ along the main diagonal and zeros

everywhere else. At steady-state, $\dot{\mathbf{a}}^{(m)}(t) = \mathbf{0}$. Therefore,

$$\mathbf{0} = \mathbf{DIAG}\left(\frac{-1}{\tau_a}\right)\mathbf{a}_{ss}^{(m)}(t) + \mathbf{r}^T\mathbf{u}_{ss}(t) \tag{139}$$

where the subscript 'ss' implies steady-state. Rearranging produces

$$\mathbf{a}_{ss}^{(m)}(t) = -\mathbf{DIAG}(-\tau_a)\mathbf{r}^T\mathbf{u}_{ss}(t). \tag{140}$$

Using the steady-state information developed earlier, that is, eq. (125), gives

$$\mathbf{M}\mathbf{u}_{ss}(t) = -\mathbf{DIAG}(-\tau_a)\mathbf{r}^T\mathbf{u}_{ss}(t) \Rightarrow \mathbf{r}^T = -\mathbf{DIAG}\left(\frac{-1}{\tau_a}\right)\mathbf{M}. \tag{141}$$

Hence, the mirror model becomes

78

$$\dot{\mathbf{a}}^{(m)}(t) = \mathbf{DIAG}\left(\frac{-1}{\tau_a}\right)\mathbf{a}^{(m)}(t) + \left[-\mathbf{DIAG}\left(\frac{-1}{\tau_a}\right)\mathbf{Mu}(t)\right] = \mathbf{F}_m \mathbf{a}^{(m)}(t) + \mathbf{B}_m \mathbf{u}(t). \qquad (142)$$

5.4 Complete System Model

Thus far, two separate models have been developed. The first is the atmospheric model, viz., the plant, which is a linear, stochastic, dynamical system driven by Brownian motion. This model, described in eq. (116), is given by

$$d\mathbf{a}^{(a)}(t) = \mathbf{F}_a \mathbf{a}^{(a)}(t)dt + \mathbf{G}_a d\mathbf{B}_a(t) \qquad (143)$$

or, in less-rigorous, white-noise notation,

$$\dot{\mathbf{a}}^{(a)}(t) = \mathbf{F}_a \mathbf{a}^{(a)}(t) + \mathbf{G}_a \mathbf{w}_a(t). \qquad (144)$$

Here, the state vector $\mathbf{a}^{(a)}(t)$ contains the coefficients of the Zernike polynomials which expand the distortion in the phase of the inbound (beacon) and outbound (HEL) wavefronts. The second is the deformable mirror model, eq. (142) and is given by

$$\dot{\mathbf{a}}^{(m)}(t) = \mathbf{F}_m \mathbf{a}^{(m)}(t) + \mathbf{B}_m \mathbf{u}(t) \qquad (145)$$

where $\mathbf{a}^{(m)}(t)$ contains the coefficients of the Zernike polynomials which expand the DM's shape. The complete system model is formed by appending these two systems:

$$\dot{\mathbf{a}}(t) = \begin{bmatrix} \dot{\mathbf{a}}^{(a)}(t) \\ \dot{\mathbf{a}}^{(m)}(t) \end{bmatrix} = \begin{bmatrix} \mathbf{F}_a & \mathbf{0} \\ \mathbf{0} & \mathbf{F}_m \end{bmatrix} \begin{bmatrix} \mathbf{a}^{(a)}(t) \\ \mathbf{a}^{(m)}(t) \end{bmatrix} + \begin{bmatrix} \mathbf{0} \\ \mathbf{B}_m \end{bmatrix} \mathbf{u}(t) + \begin{bmatrix} \mathbf{G}_a \\ \mathbf{0} \end{bmatrix} \mathbf{w}_a(t)$$

$$= \mathbf{F}\,\mathbf{a}(t) + \mathbf{B}\,\mathbf{u}(t) + \mathbf{G}\mathbf{w}_a(t). \qquad (146)$$

An output equation must also be specified. This development is described in the next section.

5.5 Output Equations

Recall that the state vector is given by

$$\mathbf{a}(t) = \begin{bmatrix} \mathbf{a}^{(a)}(t) \\ \mathbf{a}^{(m)}(t) \end{bmatrix} = \begin{bmatrix} \mathbf{a}^{(i)}(t) \\ \mathbf{a}^{(o)}(t) \\ \mathbf{a}^{(m)}(t) \end{bmatrix}. \tag{147}$$

The quantities that can be measured in this case are the Zernike coefficients associated with the inbound and reflected wavefronts. Measurements of the reflected wavefront are considered only if the metrological laser shown in Figures 2 and 6 is used. Considering the inbound wavefront first, a matrix selector can be used to extract the relevant Zernike coefficients, that is,

$$\mathbf{a}^{(i)}(t) = \begin{bmatrix} \mathbf{I} & \mathbf{0} & \mathbf{0} \end{bmatrix} \mathbf{a}(t) = \mathbf{E}_i \mathbf{a}(t) \tag{148}$$

where $\mathbf{I}$ and $\mathbf{0}$ are n by n identity and zero matrices, respectively, and $\mathbf{E}_i$ is a selection matrix. It is desired to derive the measurement equation in the form

$$\mathbf{z}_i(t_j) = \mathbf{H}_i \mathbf{a}(t_j) + \mathbf{v}_i(t_j) \tag{149}$$

where $\mathbf{v}_i(t_j)$ is a white, Gaussian, zero-mean, discrete-time process with variance

$$E\left\{\mathbf{v}_i(t_j)\mathbf{v}_i^T(t_k)\right\} = \mathbf{R}_i(t_j)\delta_{jk}. \tag{150}$$

It is assumed that the measurement device is a Hartmann wavefront sensor (HWFS) [11, 23]. Basic operation of this sensor is as follows: the HWFS contains square subapertures, each of which focuses its share of incident light onto a reticon

detector. The location of the focused light on the detector provides a measurement of the average x- and y-tilts. Thus, the HWFS is essentially a slope sensor. Hence, phase distortion in the inbound wavefront's image manifests itself in a set of subaperture tilt measurements. For a WFS with p subapertures, there are 2p outputs (p x-tilts and p y-tilts). It is further assumed that the HWFS directly outputs these slope measurements.

To begin the derivation, consider the phase distortion in the inbound image at discretized times, $\Phi^{(i)}(\bar{x}, t_j)$, where $\bar{x} = (X, Y)$ defines a rectangular position on the aperture with respect to the aperture center. Since the HWFS is a slope sensor, the x-tilt prior to reaching the square subaperture, at position X_1, Y_1, is

$$x - \text{tilt} = \left. \frac{\partial \Phi^{(i)}(\bar{x}, t_j)}{\partial Y} \right|_{X_1, Y_1}. \tag{151}$$

Let X_s, Y_s define the center of the sth subaperture with respect to the entire sensor array. Then, the average x-tilt going into the sth subaperture is [33]

$$\frac{1}{A} \int_{Y_s - \frac{\sqrt{A}}{2}}^{Y_s + \frac{\sqrt{A}}{2}} \int_{X_s - \frac{\sqrt{A}}{2}}^{X_s + \frac{\sqrt{A}}{2}} \frac{\partial \Phi(X, Y, t_j)}{\partial Y} dX \, dY \tag{152}$$

where A is the area of a subaperture. From Peterson and Cho [22], the output of a HWFS is a similar integral, but with the slopes spatially weighted. In particular, for the x-tilt channel, the output is

$$z_{x_s}(t_j) = L \frac{1}{A} \int_{Y_s - \frac{\sqrt{A}}{2}}^{Y_s + \frac{\sqrt{A}}{2}} \int_{X_s - \frac{\sqrt{A}}{2}}^{X_s + \frac{\sqrt{A}}{2}} W_x(X - X_s, Y - Y_s) \frac{\partial \Phi(X, Y, t_j)}{\partial Y} dX \, dY + v_{i_{x_s}}(t_j) \tag{153}$$

where L is a constant which depends on wavelength, lenslet focal length, and output scaling and $v_{i_{x_s}}(t_j)$ is an element from the vector $v_i(t_j)$. Peterson and Cho [22] have also

derived a normalized version of the spatial weighting function, which for the x-tilt channel can be expressed as

$$W_x(X',Y') = \frac{1}{2\ln 2}\left[2\ln 2 - \left(1 - \frac{2Y'}{\sqrt{A}}\right)\ln\left(1 - \frac{2Y'}{\sqrt{A}}\right) - \left(1 + \frac{2Y'}{\sqrt{A}}\right)\ln\left(1 + \frac{2Y'}{\sqrt{A}}\right)\right] . \quad (154)$$

The inbound wavefront's distorted phase image can be written as a linear combination of Zernike polynomials, that is,

$$\Phi^{(i)}(\vec{x}, t_j) = \sum_n a_{n+1}^{(i)}(t_j) Z_{n+1}(\vec{x}) . \quad (155)$$

Taking the partial derivative of $\Phi^{(i)}(\vec{x}, t_j)$ with respect to Y, as described in eq. (151), produces

$$\frac{\partial \Phi^{(i)}(\vec{x}, t_j)}{\partial Y} = \sum_n a_{n+1}^{(i)}(t_j) \frac{\partial Z_{n+1}(\vec{x})}{\partial Y} . \quad (156)$$

Using eq. (156) in eq. (153) yields

$$z_{x_s}(t_j) = L\frac{1}{A}\int_{Y_s - \frac{\sqrt{A}}{2}}^{Y_s + \frac{\sqrt{A}}{2}}\int_{X_s - \frac{\sqrt{A}}{2}}^{X_s + \frac{\sqrt{A}}{2}} W_x(X - X_s, Y - Y_s)\sum_n a_{n+1}^{(i)}(t_j)\frac{\partial Z_{n+1}(\vec{x})}{\partial Y}dX\,dY + v_{i_{x_s}}(t_j)$$

$$= L\frac{1}{A}\sum_n\left[\int_{Y_s - \frac{\sqrt{A}}{2}}^{Y_s + \frac{\sqrt{A}}{2}}\int_{X_s - \frac{\sqrt{A}}{2}}^{X_s + \frac{\sqrt{A}}{2}} W_x(X - X_s, Y - Y_s)\frac{\partial Z_{n+1}(\vec{x})}{\partial Y}\right]dX\,dY\, a_{n+1}^{(i)}(t_j) + v_{i_{x_s}}(t_j)$$

$$= \frac{L}{A}\mathbf{p}_x^T \mathbf{a}^{(i)}(t_j) + v_{i_{x_s}}(t_j)$$

$$= \frac{L}{A}\mathbf{p}_x^T \mathbf{E}_i \mathbf{a}(t_j) + v_{i_{x_s}}(t_j) \quad (157)$$

where

$$\mathbf{p}_x^T = \left[\iint W_x \frac{\partial Z_2(\bar{x})}{\partial y} dXdY \quad \iint W_x \frac{\partial Z_3(\bar{x})}{\partial y} dXdY \quad \cdots \quad \iint W_x \frac{\partial Z_{n+1}(\bar{x})}{\partial y} dXdY \right] \quad (158)$$

and $W_x = W_x(X-X_s, Y-Y_s)$. In order to specify measurements of the inbound wavefront completely, expressions similar to those in eq. (157) would have to be written for y-tilts and for each of the p subapertures. Putting these equations into matrix form gives

$$\mathbf{z}_i(t_j) = \frac{L}{A} \mathbf{N} \mathbf{E}_i \mathbf{a}(t_j) + \mathbf{v}_i(t_j)$$

$$= \mathbf{H}_i \mathbf{a}(t_j) + \mathbf{v}_i(t_j) \quad (159)$$

where $\mathbf{H}_i = \frac{L}{A} \mathbf{N} \mathbf{E}_i$ and $\mathbf{N}$ is a 2p x n matrix with the following form:

$$\mathbf{N} = \left[\mathbf{p}_{x1} \mathbf{p}_{x2} \cdots \mathbf{p}_{xp} \mathbf{p}_{y1} \mathbf{p}_{y2} \cdots \mathbf{p}_{yp} \right]^T . \quad (160)$$

More information on matrix $\mathbf{N}$ can be found in Appendix B.

Proceeding in a similar manner for measurements of the reflected wavefront, the selection matrix is

$$\mathbf{a}^{(m)}(t) = \begin{bmatrix} \mathbf{0} & \mathbf{0} & \mathbf{I} \end{bmatrix} \mathbf{a}(t) = \mathbf{E}_m \mathbf{a}(t) \quad (161)$$

where $\mathbf{I}$ and $\mathbf{0}$ are n by n identity and zero matrices. The measurement equation in this case becomes

$$\mathbf{z}_m(t_j) = \mathbf{H}_m \mathbf{a}(t_j) + \mathbf{v}_m(t_j) \quad (162)$$

where $\mathbf{v}_m(t_j)$ is a white, Gaussian, zero-mean, discrete-time process with variance

$$E\left\{ \mathbf{v}_m(t_j) \mathbf{v}_m^T(t_k) \right\} = \mathbf{R}_m(t_j) \delta_{jk} \quad (163)$$

and $\mathbf{v}_i(t_j)$ and $\mathbf{v}_m(t_j)$ are independent random vectors. In this case, the x-tilt output of the HWFS is

$$z_{m_{x_s}}(t_j) = L \frac{1}{A} \int_{Y_s - \frac{\sqrt{A}}{2}}^{Y_s + \frac{\sqrt{A}}{2}} \int_{X_s - \frac{\sqrt{A}}{2}}^{X_s + \frac{\sqrt{A}}{2}} W_x(X - X_s, Y - Y_s) \sum_n a_{n+1}^{(m)}(t_j) \frac{\partial Z_{n+1}(\bar{x})}{\partial Y} dX dY + v_{m_{x_s}}(t_j)$$

$$= \frac{L}{A} \mathbf{p}_x^T \mathbf{E}_m \mathbf{a}(t_j) + v_{m_{x_s}}(t_j). \tag{164}$$

Writing equations for each subaperture and for the y-tilts produces

$$\mathbf{z}_m(t_j) = \frac{L}{A} \mathbf{N} \mathbf{E}_m \mathbf{a}(t_j) + \mathbf{v}_m(t_j)$$

$$= \mathbf{H}_m \mathbf{a}(t_j) + \mathbf{v}_m(t_j) \tag{165}$$

where $\mathbf{H}_m = \frac{L}{A} \mathbf{N} \mathbf{E}_m$.

In summary, the following dynamics model and output equation have been

developed:

$$\dot{\mathbf{a}}(t) = \begin{bmatrix} \dot{\mathbf{a}}^{(a)}(t) \\ \dot{\mathbf{a}}^{(m)}(t) \end{bmatrix} = \begin{bmatrix} \mathbf{F}_a & \mathbf{0} \\ \mathbf{0} & \mathbf{F}_m \end{bmatrix} \begin{bmatrix} \mathbf{a}^{(a)}(t) \\ \mathbf{a}^{(m)}(t) \end{bmatrix} + \begin{bmatrix} \mathbf{0} \\ \mathbf{B}_m \end{bmatrix} \mathbf{u}(t) + \begin{bmatrix} \mathbf{G}_a \\ \mathbf{0} \end{bmatrix} \mathbf{w}_a(t) = \mathbf{F}\mathbf{a}(t) + \mathbf{B}\mathbf{u}(t) + \mathbf{G}\mathbf{w}_a(t), \tag{166}$$

$$\mathbf{z}_i(t_j) = \mathbf{H}_i \mathbf{a}(t_j) + \mathbf{v}_i(t_j), \tag{167}$$

$$\mathbf{z}_m(t_j) = \mathbf{H}_m \mathbf{a}(t_j) + \mathbf{v}_m(t_j), \tag{168}$$

$$\mathbf{z}(t_j) = \begin{bmatrix} \mathbf{z}_i(t_j) \\ \mathbf{z}_m(t_j) \end{bmatrix} = \begin{bmatrix} \mathbf{H}_i \\ \mathbf{H}_m \end{bmatrix} \mathbf{a}(t_j) + \begin{bmatrix} \mathbf{v}_i(t_j) \\ \mathbf{v}_m(t_j) \end{bmatrix} = \mathbf{H}\mathbf{a}(t_j) + \mathbf{v}(t_j), \tag{169}$$

where $\mathbf{w}_a(t)$ is a zero-mean, white, Gaussian noise with $E\{\mathbf{w}_a(t)\mathbf{w}_a(t+\tau)\} = \mathbf{I}\delta(\tau)$, $\mathbf{v}_i(t_j)$

is a zero-mean, white, Gaussian, discrete-time process with $E\{\mathbf{v}_i(t_j)\mathbf{v}_i^T(t_k)\} = \mathbf{R}_i(t_j)\delta_{jk}$,

$\mathbf{v}_m(t_j)$ is a zero-mean, white, Gaussian, discrete-time process with

$$E\{\mathbf{v}_m(t_j)\mathbf{v}_m^T(t_k)\} = \mathbf{R}_m(t_j)\delta_{jk}, \quad \mathbf{H} = \begin{bmatrix} \mathbf{H}_i \\ \mathbf{H}_m \end{bmatrix}, \text{ and } \mathbf{v}(t_j) = \begin{bmatrix} \mathbf{v}_i(t_j) \\ \mathbf{v}_m(t_j) \end{bmatrix}. \text{ Also, } \mathbf{v}(t_j) \text{ is a zero-}$$

mean, white, Gaussian, discrete-time process with variance

$$E\{\mathbf{v}(t_j)\mathbf{v}^T(t_k)\} = \begin{bmatrix} E\{\mathbf{v}_i(t_j)\mathbf{v}_i(t_k)\} & E\{\mathbf{v}_i(t_j)\mathbf{v}_m(t_k)\} \\ E\{\mathbf{v}_m(t_j)\mathbf{v}_i(t_k)\} & E\{\mathbf{v}_m(t_j)\mathbf{v}_m(t_k)\} \end{bmatrix} = \begin{bmatrix} \begin{pmatrix} \mathbf{R}_i(t_j) & 0 \\ 0 & \mathbf{R}_m(t_j) \end{pmatrix} = \mathbf{R}(t_j) \quad j = k \\ \begin{pmatrix} 0 & 0 \\ 0 & 0 \end{pmatrix} \quad j \neq k \end{bmatrix}.$$

$$(170)$$

Equation (166) represents the underlying dynamic system for the Kalman filter.

5.6 Discrete-Time System

The system in eq. (166) is a continuous-time model of the atmosphere and deformable mirror. Since the Kalman filter and controller to be developed in the next chapter will be implemented in a digital computer, it is necessary to convert eq. (166) to an equivalent discrete-time system [16]. To perform this conversion, consider the solution to eq. (166) which can be written as

$$\mathbf{a}(t_{j+1}) = \Phi(t_{j+1},t_j)\mathbf{a}(t_j) + \left[\int_{t_j}^{t_{j+1}}\Phi(t_{j+1},\tau)\mathbf{Bu}(\tau)d\tau\right] + \left[\int_{t_j}^{t_{j+1}}\Phi(t_{j+1},\tau)\mathbf{Gw}_a(\tau)d\tau\right]$$

$$= \Phi(t_{j+1},t_j)\mathbf{a}(t_j) + \left[\int_{t_j}^{t_{j+1}}\Phi(t_{j+1},\tau)\mathbf{B}d\tau\right]\mathbf{u}(t_j) + \left[\int_{t_j}^{t_{j+1}}\Phi(t_{j+1},\tau)\mathbf{Gw}_a(\tau)d\tau\right]$$

$$= \Phi(t_{j+1},t_j)\mathbf{a}(t_j) + \mathbf{B}_d(t_j)\mathbf{u}(t_j) + \mathbf{w}_d(t_j). \tag{171}$$

Note that the second expression in eq. (171) can be written since it is assumed that the control, $\mathbf{u}(t)$, is held constant over each sample period. Also, in eq. (171), $\Phi(t_{j+1},t_j)$ is the

state transition matrix, $\mathbf{B_d}(t_j) = \int_{t_j}^{t_{j+1}} \Phi(t_{j+1},\tau)\mathbf{B}d\tau$, and $\mathbf{w_d}(t_j)$ is a white, Gaussian,

discrete-time stochastic process with statistics duplicating those of

$\int_{t_j}^{t_{j+1}} \Phi(t_{j+1},\tau)\mathbf{G}\mathbf{w_a}(\tau)d\tau$. In other words, $\mathbf{w_d}(t_j)$ has statistics

$$E\left\{\mathbf{w_d}(t_j)\right\} = \mathbf{0}$$

$$E\left\{\mathbf{w_d}(t_j)\mathbf{w_d^T}(t_j)\right\} = \mathbf{Q_d}(t_j) = \int_{t_j}^{t_{j+1}} \Phi(t_{j+1},\tau)\mathbf{G}\,\mathbf{I}\mathbf{G^T}\Phi^T(t_{j+1},\tau)d\tau \qquad (172)$$

$$E\left\{\mathbf{w_d}(t_j)\mathbf{w_d^T}(t_k)\right\} = \mathbf{0} \quad j \neq k.$$

Since the complete system model is linear and time-invariant, $\Phi(t_{j+1},t_j)$ reduces to a

function of the time difference $\Delta t = t_{j+1} - t_j$. Therefore,

$$\Phi(t_{j+1},t_j) = \Phi(t_{j+1} - t_j) = e^{F(t_{j+1}-t_j)}. \qquad (173)$$

Appendix B contains a complete explanation of the determination of the discrete-time

system matrices for simulation purposes.

5.7 Summary

At this point, all of the required modeling has been performed. In particular,

atmospheric and mirror models have been formed, output equations have been specified,

and an equivalent discrete-time system has been developed. Now, these models can be

embedded in a Kalman filter so that estimation of the outbound wavefront Zernike

expansion coefficients can be performed. Using these estimates, a linear quadratic

Gaussian controller will apply the estimated conjugate phase to the mirror. The next

chapter addresses design of the filter and controller.

6.1 Introduction

The objective of this research is to design a control system which can provide commands to the deformable mirror to cancel the effects of atmospheric turbulence in the highly dynamic scenario of the ABL. The atmospheric model, mirror model, and measurement equations have been discussed and are given by eqs. (166) - (170).

6.2 Kalman Filter

A Kalman filter is used to estimate the state vector $\mathbf{a}(t_j)$. Recall that $\mathbf{a}(t_j)$ is composed of the inbound, outbound, and mirror Zernike polynomial expansion coefficients, i.e., $\mathbf{a}(t) = \left[\left\{\mathbf{a}^{(i)}(t)\right\}^T \quad \left\{\mathbf{a}^{(o)}(t)\right\}^T \quad \left\{\mathbf{a}^{(m)}(t)\right\}^T\right]^T$. The Kalman filter accepts measurements, $\mathbf{z}(t_j)$, and outputs estimates of the system state, $\hat{\mathbf{a}}(t_j)$, where the superscript '^' is used to denote an estimate. The filter performs these estimates using an internal model, eq. (171), propagating the state estimate and state estimation error covariance, and then appropriately incorporating the measurements, eq. (167). The filter's state estimation error covariance, denoted $\mathbf{P}_f(t)$, is defined by

$$\mathbf{P}_f(t) = E\left\{\left[\mathbf{a}(t) - \hat{\mathbf{a}}(t)\right]\left[\mathbf{a}(t) - \hat{\mathbf{a}}(t)\right]^T \big| \mathbf{Z}(t)\right\} \tag{174}$$

where the expectation is conditioned on the measurement history $\mathbf{Z}(t)$.

Operation of the Kalman filter can be divided into two processes: propagation and measurement update. Propagation is the change in state estimate and filter covariance as

time is moved forward from t_{j-1} to t_j. Measurement update is the change in state estimate and filter covariance as measurements are processed. The governing equations for these two cycles are [16]:

$$\hat{a}(t_j^-) = \Phi(t_j - t_{j-1})\hat{a}(t_{j-1}^+) + B_d(t_{j-1})u(t_{j-1}),\tag{175}$$

$$P_f(t_j^-) = \Phi(t_j - t_{j-1})P_f(t_{j-1}^+)\Phi^T(t_j - t_{j-1}) + Q_d(t_j),\tag{176}$$

$$K(t_j) = P_f(t_j^-)H^T\left[HP_f(t_j^-)H^T + R(t_j)\right]^{-1},\tag{177}$$

$$\hat{a}(t_j^+) = \hat{a}(t_j^-) + K(t_j)\left[z_j - H\hat{a}(t_j^-)\right],\tag{178}$$

and

$$P_f(t_j^+) = P_f(t_j^-) - K(t_j)HP_f(t_j^-)\tag{179}$$

where

$\hat{a}(t_{j-1}^+) = $ state estimate at the start of the t_{j-1} to t_j propagation cycle and after the measurement update at t_{j-1},

$P_f(t_{j-1}^+) = $ filter covariance at the start of the t_{j-1} to t_j propagation cycle and after the measurement update at t_{j-1},

$\hat{a}(t_j^-) = $ state estimate at the end of the t_{j-1} to t_j propagation cycle and before the measurement update at t_j,

$P_f(t_j^-) = $ filter covariance at the end of the t_{j-1} to t_j propagation cycle and before the measurement update at t_j,

$K(t_j) = $ Kalman filter gain,

$\hat{a}(t_j^+) = $ state estimate at the end of the t_{j-1} to t_j propagation cycle and after the measurement update at t_j,

$P_f(t_j^+) = $ filter covariance at the end of the t_{j-1} to t_j propagation cycle and after the measurement update at t_j,

and

$\mathbf{z}_j =$ measurement realization at the update time.

Initial conditions on the filter, that is, $\hat{\mathbf{a}}(t_0)$ and $\mathbf{P}_f(t_0)$, must also be specified. Therefore, the initial conditions and eqs. (166) - (171), (175) - (179) fully describe the Kalman filter.

6.3 LQG Controller

In this section, an LQG (*L*inear dynamic system model, *Q*uadratic cost, and *G*aussian noise inputs) controller [17] will be developed. The general idea here is that the behavior of some underlying dynamic system is to be affected by control inputs in such a way that the controlled variables exhibit some desired characteristics [17]. The controller will in fact be a regulator, which is based on the assumption that there are costs associated with nonzero controlled variables and nonzero controls. The cost function is quadratic in nature, that is, the cost is proportional to the weighted squares of the controlled variables and inputs.

For the ABL, the inbound wavefront's phase is measured to determine the turbulence-induced wavefront aberrations. It is then desired to apply the estimated conjugate (opposite) phase to the mirror so that the HEL's wavefront phase perturbation will be minimal upon reaching the target, viz., the Strehl ratio at the target is maximized. Therefore, the controlled variables are

$$\mathbf{y}(t_j) = \begin{bmatrix} \mathbf{0} & -\mathbf{I} & \mathbf{I} \end{bmatrix} \mathbf{a}(t_j) = \mathbf{E}_c \mathbf{a}(t_j) = -\mathbf{a}^{(o)}(t_j) + \mathbf{a}^{(m)}(t_j) \qquad (180)$$

where the size of $\mathbf{y}(t_j)$ is n by 1.

A useful form of quadratic cost function is [17]

$$J = E\left\{\sum_{j=0}^{N} \frac{1}{2}\left[\mathbf{y}^T(t_j)\mathbf{Y}(t_j)\mathbf{y}(t_j) + \mathbf{u}^T(t_j)\mathbf{U}(t_j)\mathbf{u}(t_j)\right] + \frac{1}{2}\mathbf{y}^T(t_{N+1})\mathbf{Y}_f\mathbf{y}(t_{N+1})\right\} \quad (181)$$

where $\mathbf{Y}(t_j) \; \forall \; t_j$ and $\mathbf{Y}_f$ are selected as n by n (n = 2 for tilts) positive definite matrices and

$\mathbf{U}(t_j)$ is a positive definite matrix of dimension equal to the number of actuators. In the

simulations discussed in Chapter 7, the quadratic cost function matrices were selected as

$$\mathbf{Y}(t_j) = \mathbf{Y}_f = \begin{bmatrix} 5 & 0 \\ 0 & 1 \end{bmatrix}, \; \mathbf{U}(t_j) = 0.5\mathbf{I}. \quad (182)$$

These values were selected after many iterations to provide satisfactory state regulation

without expending too much control energy. Recall that the controlled variables are

$\mathbf{y}(t_j) = \begin{bmatrix} -a_2^{(o)}(t) + a_2^{(m)}(t) & -a_3^{(o)}(t) + a_3^{(m)}(t) \end{bmatrix}^T$. Since dynamic motion occurs only in the x-

direction, it is expected that there will be more error in the x-tilt controlled variables as

compared to the y-tilt variables. Hence, entry (1,1) of $\mathbf{Y}(t_j)$ and $\mathbf{Y}_f$ was set to 5 to place

more emphasis on regulation of the x-tilt controlled variables.

Equation (181) does not include any cross-terms between the controlled variables

and controls. Cross-terms are useful when it is desired to exert control influence on the

state vector over the entire sample period, not just at the sample points. However, since

the sample period is small for this system, it is expected that cross-terms would be of

negligible benefit and thus will not be necessary. Using the expression for the controlled

variables, eq. (180), in eq. (181), the cost function becomes

$$J = E\left\{\sum_{j=0}^{N} \frac{1}{2}\left[\mathbf{a}^T(t_j)\mathbf{A}(t_j)\mathbf{a}(t_j) + \mathbf{u}^T(t_j)\mathbf{U}(t_j)\mathbf{u}(t_j)\right] + \frac{1}{2}\mathbf{a}^T(t_{N+1})\mathbf{A}_f\mathbf{a}(t_{N+1})\right\} \quad (183)$$

91

where $A(t_j) = E_c^T Y(t_j) E_c$ and $A_f = E_c^T Y_f E_c$. It is desired to determine the control function $u^*(\bullet)$ which minimizes the cost function given in eq. (183). It can be shown that the cost minimizing controller [17] is

$$u^*(t_j) = -G_c^*(t_j)\hat{a}(t_j^+) \tag{184}$$

where $G_c^*(t_j)$ is the controller gain. This gain can be calculated from the solution to

$$G_c^*(t_j) = \left[U(t_j) + B_d^T(t_j) K_c(t_{j+1}) B_d(t_j) \right]^{-1} \left[B_d^T(t_j) K_c(t_{j+1}) \Phi(t_{j+1}, t_j) \right] \tag{185}$$

where $K_c(t_j)$ satisfies the backward Riccati equation [17]

$$K_c(t_j) = A(t_j) + \Phi^T(t_{j+1}, t_j) K_c(t_{j+1}) \Phi(t_{j+1}, t_j) - \left[\Phi^T(t_{j+1}, t_j) K_c(t_{j+1}) B_d(t_j) \right] G_c^*(t_j)$$

$$= A(t_j) + \Phi^T(t_{j+1}, t_j) K_c(t_{j+1}) \left[\Phi(t_{j+1}, t_j) - B_d(t_j) G_c^*(t_j) \right] \tag{186}$$

solved backwards from the terminal condition

$$K_c(t_{N+1}) = A_f. \tag{187}$$

The filter and associated measurements devices are denoted by Kalman filter 1, Kalman filter 2 and WFS 1, WFS 2 in Figure 25. The input to Kalman filter 1 is $z_i(t_j)$, that is, the measured Zernike coefficients of the inbound wavefront, while the input to Kalman filter 2 is $z_m(t_j)$, that is, the measured Zernike coefficients of the reflected wavefront. Measurements $z_m(t_j)$ are included in this figure in case the metrological laser is used. Currently, a metrological laser is not used in the ABL and thus these measurements are not incorporated into the simulations. The blocks ACT and DM in Figure 25 represent the actuator dynamics and deformable mirror, respectively. Also, G_c^* and u^* represent the LQG controller gain and the cost minimizing control function. The atmospheric and DM models contain no coupling between each other, therefore, the

92

single augmented Kalman filter (atmospheric and DM models) can be decomposed into

the two decoupled filters, Kalman filter 1 and Kalman filter 2, displayed in Figure 25.

$$w_\alpha(t) \longrightarrow \boxed{\text{ATMOSPHERIC MODEL}} \xrightarrow{\overset{(a)}{a}(t_j)} \begin{bmatrix} 0 & 0 & 1 & 0 \\ 0 & 0 & 0 & 1 \end{bmatrix}$$

$$\overset{(o)}{a}(t_j)$$

$$\begin{bmatrix} 1 & 0 & 0 & 0 \\ 0 & 1 & 0 & 0 \end{bmatrix}$$

$$\overset{(i)}{a}(t_j)$$

LQG CONTROLLER

LQR

$$G_c^*$$

$$u^* \rightarrow \boxed{\text{ACT}} \rightarrow \boxed{\text{DM}} \xrightarrow{\overset{(m)}{a}(t_j)} \rightarrow y(t_j)$$

$$\boxed{\text{WFS2}}$$

$$\overset{\wedge(m)}{a}(t_j) \rightarrow \boxed{\begin{array}{c}\text{KALMAN FILTER 2} \\ \text{DM AND ACTUATOR} \\ \text{BASED MODELS}\end{array}}$$

$$z_m(t_j) = H_m \overset{(m)}{a}(t_j) + v_m(t_j) \qquad v_m(t_j)$$

$$\overset{\wedge(a)}{a}(t_j) \rightarrow \boxed{\begin{array}{c}\text{KALMAN FILTER 1} \\ \text{ATMOSPHERICS}\end{array}}$$

$$\boxed{\text{WFS1}}$$

$$z_i(t_j) = H_i \overset{(i)}{a}(t_j) + v_i(t_j) \qquad v_i(t_j)$$
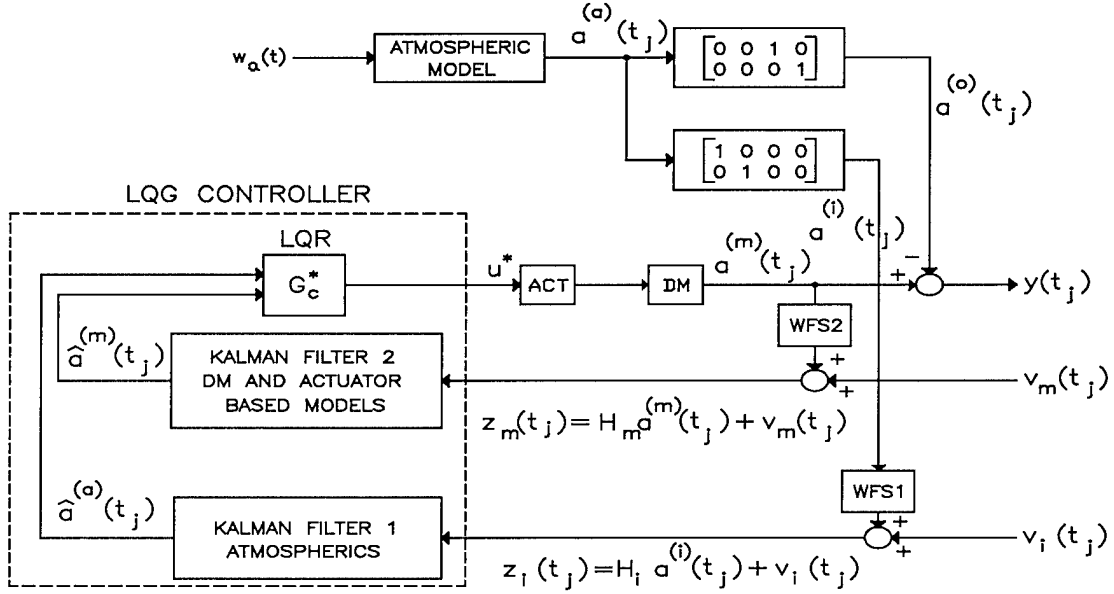
Figure 25. Adaptive optics control system.

The dimensionality of the variables associated with the control system is given in Tables

2a and 2b. In these tables, n is the number of Zernike modes used in the wavefront

expansions, p is the number of subapertures in the Hartmann wavefront sensor, and n_A is

the number of actuators.

Matrix/Vector	Dimension
$\mathbf{a}(t)$	3n-by-1
$\mathbf{a}^{(a)}(t)$	2n-by-1
$\mathbf{a}^{(m)}(t)$	n-by-1
$\mathbf{a}^{(i)}(t)$	n-by-1
$\mathbf{a}^{(o)}(t)$	n-by-1
$\mathbf{m}_i$	n_A-by-1
$\mathbf{M}$	n-by-n_A
$\mathbf{v}_a$	n_A-by-1
$\mathbf{r}_i$	n_A-by-1
$\mathbf{r}$	n_A-by-n
$\mathbf{DIAG}(1/\tau)$	n-by-n
$\mathbf{E}_i$ and $\mathbf{E}_m$	n-by-3n
$\mathbf{F}_a$	2n-by-2n
$\mathbf{F}_m$	n-by-n
$\mathbf{F}$	3n-by-3n
$\Phi(t_{j+1}, t_j)$	3n-by-3n
$\mathbf{B}_m$	n-by-n_A
$\mathbf{B}$	3n-by-n_A
$\mathbf{u}(t)$	n_A-by-1
$\mathbf{G}_a$	2n-by-2
$\mathbf{G}$	3n-by-2
$\mathbf{w}_a(t)$	2-by-1
$\mathbf{z}_i(t_j)$	2p-by-1
$\mathbf{H}_i$	2p-by-3n
$\mathbf{R}_i(t_j)$	2p-by-2p
$\mathbf{z}_m(t_j)$	2p-by-1
$\mathbf{v}_i(t_j)$	2p-by-1

Table 2a. Variable dimensions.

Matrix/Vector	Dimension
$\mathbf{H_m}$	2p-by-3n
$\mathbf{v_m}(t_j)$	2p-by-1
$\mathbf{R_m}(t_j)$	2p-by-2p
$\mathbf{z}(t_j)$	4p-by-1
$\mathbf{H}$	4p-by-3n
$\mathbf{v}(t_j)$	4p-by-1
$\mathbf{R}(t_j)$	4p-by-4p
$\mathbf{N}$	2p-by-n
$\mathbf{p_x}^T, \mathbf{p_y}^T$	1-by-n
$\mathbf{B_d}(t_j)$	3n-by-n_A
$\mathbf{w_d}(t_j)$	3n-by-1
$\mathbf{Q_d}(t_j)$	3n-by-3n
$\hat{\mathbf{a}}(t_{j-1}^+), \hat{\mathbf{a}}(t_j^-), \hat{\mathbf{a}}(t_j^+)$	3n-by-1
$\mathbf{P_f}(t_{j-1}^+), \mathbf{P_f}(t_j^-), \mathbf{P_f}(t_j^+)$	3n-by-3n
$\mathbf{K}(t_j)$	3n-by-4p
$\mathbf{z}_j$	4p-by-1
$\mathbf{E_c}$	n-by-3n
$\mathbf{y}(t_j)$	n-by-1
$\mathbf{U}(t_j)$	n_A-by-n_A
$\mathbf{A}(t_j), \mathbf{A_f}$	3n-by-3n
$\mathbf{u}^*(t_j)$	n_A-by-1
$\mathbf{G_c}^*(t_j)$	n_A-by-3n
$\mathbf{U}(t_j)$	n_A-by-n_A
$\mathbf{Y}(t_j), \mathbf{Y_f}$	n-by-n
$\mathbf{Y}(t_{N+1})$	n-by-n
$\mathbf{K_c}(t_j)$	3n-by-3n
$\mathbf{K_c}(t_{N+1})$	3n-by-3n

Table 2b. Variable dimensions.

6.4 Summary

A Kalman filter and LQG controller were designed in the last few sections. The filter produces estimates of the state variables while the controller is used to drive the controlled variables to zero. That is, the controller generates gains which are used to provide commands to the DM.

At this point, all of the analysis has been set into place. Therefore, the complete system, that is, atmospheric and mirror models, output equations, filter and controller can be simulated to evaluate performance. To accomplish this simulation, a phase screen, which will be discussed in Chapter 7, will be generated to provide the measured quantity. Simulation results involve the Root Mean Square (RMS) phase distortions, Strehl ratios, phase screen and estimated quantities, and Monte Carlo statistics. The next chapter addresses the simulations and analyzes the results.

VII. Simulations

7.1 Introduction

Now that all of the modeling has been performed, the entire system can be simulated to evaluate its performance. Before the simulations can be run, a few other items must be covered, including performance metrics, the phase screen, and development of the simulated correlation functions.

7.2 Performance Metrics

In this section, the metrics used to evaluate system performance are delineated. These quantities provide a measure of the performance of the controller. There are two metrics that will be used in this work. Imaging performance is specified by a quantity termed the Strehl Ratio (SR) and the Root Mean Square (RMS) phase distortion. The Strehl ratio is defined as the irradiance with wavefront aberrations present divided by the diffraction-limited irradiance on the optical axis [1]. A useful estimate of the Strehl ratio can be made if the aperture averaged, squared, residual wavefront phase, $\Phi_{res}^2(t)$, is less than $(2\pi / 10)^2$ rad^2 [23]. In this case, the Strehl ratio becomes

$$SR \approx \exp\left\{-\Phi_{res}^2(t)\right\}. \tag{188}$$

From eq. (188), it is obvious that if $\Phi_{res}^2(t) = 0$, that is, perfect correction of the wavefront phase deformations is performed, then SR = 1. This is the upper bound on the Strehl ratio. In most applications, a Strehl ratio of 0.6 or higher is adequate. However, it should be noted that the Strehl ratio is dependent on the seeing conditions (clear,

overcast, precipitation, etc.), AO hardware, and other factors. Hence, a measure of a "good" Strehl ratio is difficult to present.

There are three Strehl ratios that are of interest in this work. The first is the Strehl ratio of the outbound wavefront which provides a measure of the uncompensated system performance. The second is the Strehl ratio of the corrected wavefront using simple phase conjugation. Simple phase conjugation implies that measurements of the inbound wavefront's phase deformations (x- and y-tilts) are directly, negatively, applied to the DM. In this case, there are no correlation functions to determine. It is still a closed-loop system; however, anisoplanatism is not taken into account. This is the most rudimentary phase conjugation scheme available and is currently used in most AO applications. Simple phase conjugation provides an algorithm on which to base the performance of the AO tilt compensation algorithm developed in this work. The last Strehl ratio is that of the compensated wavefront obtained from the work in previous chapters. In this case, the necessary correlation functions are calculated, estimates of the outbound wavefront Zernike phase expansion coefficients are obtained, and the LQG controller attempts to drive the controlled variables to zero. Comparing these three Strehl ratios, which involve increasing system complexity, provides a measure of the performance enhancement that can be obtained using tilt compensation.

Since the wavefronts have been expanded using Zernike polynomials, the Strehl ratios take on a form involving the Zernike expansion coefficients. In particular, for the fully compensated wavefront, the residual wavefront phase becomes

$$\Phi_{res}(\vec{x},t) = -\Phi^{(o)}(\vec{x},t) + \Phi^{(m)}(\vec{x},t) \tag{189}$$

98

where $\Phi^{(o)}(\bar{x},t), \Phi^{(m)}(\bar{x},t)$ are the outbound wavefront phase and the phase correction applied by the DM, respectively. The aperture averaged, squared, residual wavefront phase is

$$\Phi_{res}^2(t) = \int W(\bar{x})\Phi_{res}^2(\bar{x},t)d\bar{x} \qquad (190)$$

where $\Phi_{res}^2(\bar{x},t)$ is the squared, residual wavefront phase. Using the Zernike polynomial expansions, that is,

$$\Phi^{(o)}(\bar{x},t) = \sum_j a_j^{(o)}(t)Z_j(\bar{x}) \quad , \quad \Phi^{(m)}(\bar{x},t) = \sum_k a_k^{(m)}(t)Z_k(\bar{x}) \qquad (191)$$

in eq. (190) produces

$$\Phi_{res}^2(t) = \int W(\bar{x})\left[-\sum_j a_j^{(o)}(t)Z_j(\bar{x}) + \sum_k a_k^{(m)}(t)Z_k(\bar{x})\right]^2 d\bar{x}. \qquad (192)$$

Up to this point, only x- and y-tilts have been considered in wavefront expansions. However, in terms of computing Strehl ratios, it is advantageous to use more Zernike modes in the inbound, and therefore, outbound, wavefront expansions. If the inbound wavefront was described entirely by tilts, then the Strehl ratios would be unusually high, since tilts are removed from the corrected wavefront. For example, assume that the inbound wavefront phase is only corrupted by tilts. Then, after compensating and applying the conjugate phase to the mirror, the residual wavefront phase would be near zero, assuming the filter/controller performed well. In this case, the Strehl ratio would be near one, that is, the diffraction limit. Unfortunately, this type of AO performance is not feasible. To rectify this situation, more Zernike modes can be used to expand the inbound and outbound wavefronts. In practice, an accurate representation of these actual

wavefronts would require an infinite number of Zernike modes. Obviously, the

expansion must be truncated at some point; however, tilts are not the only components of

atmospherically distorted wavefront phases. In fact, five modes, x- and y-tilts, focus, and

orthogonal components of astigmatism, were used to provide a more accurate

representation of the actual inbound and outbound wavefronts. The AO scheme

developed in this work only compensates for the tilt modes, therefore, the outbound

wavefront, after compensation, is still corrupted by the remaining three modes. In this

way, more accurate Strehl ratios will be obtained.

For n Zernike modes (n = 5 for tilts, coma, astigmatisms), eq. (192) becomes

$$\Phi_{res}^2(t) = \int W(\bar{x}) \left[-a_2^{(o)}(t)Z_2(\bar{x}) - \cdots - a_{n+1}^{(o)}(t)Z_{n+1}(\bar{x}) + a_2^{(m)}(t)Z_2(\bar{x}) + a_3^{(m)}(t)Z_3(\bar{x}) \right]^2 d\bar{x} . \quad (193)$$

Notice that tilt compensation results in including only $a_2^{(m)}(t)$ and $a_3^{(m)}(t)$. Expanding the

term in brackets in eq. (193) and using the orthonormality property of the Zernike

polynomials produces

$$\Phi_{res}^2(t) = \left[-a_2^{(o)}(t) + a_2^{(m)}(t) \right]^2 + \left[-a_3^{(o)}(t) + a_3^{(m)}(t) \right]^2 + \left[\left\{ a_4^{(o)}(t) \right\}^2 + \cdots + \left\{ a_{n+1}^{(o)}(t) \right\}^2 \right] . \quad (194)$$

Therefore, the third Strehl ratio becomes

$$SR_3 \approx \exp \left\{ (-1) \left(\left[-a_2^{(o)}(t) + a_2^{(m)}(t) \right]^2 + \left[-a_3^{(o)}(t) + a_3^{(m)}(t) \right]^2 + \left[\left\{ a_4^{(o)}(t) \right\}^2 + \cdots + \left\{ a_{n+1}^{(o)}(t) \right\}^2 \right] \right) \right\} . \quad (195)$$

For the Strehl ratio of the outbound wavefront, the residual wavefront phase is

$$\Phi_{res}(\bar{x}, t) = \Phi^{(o)}(\bar{x}, t) = \sum_j a_j^{(o)}(t)Z_j(\bar{x}) . \quad (196)$$

Then,

$$\Phi_{res}^2(t) = \int W(\bar{x})\left[\sum_j a_j^{(o)}(t)Z_j(\bar{x})\right]^2 d\bar{x} = \int W(\bar{x})\left[a_2^{(o)}(t)Z_2(\bar{x})+\cdots+a_{n+1}^{(o)}(t)Z_{n+1}(\bar{x})\right]^2 d\bar{x}. \quad (197)$$

Applying the orthonormality property again produces

$$\Phi_{res}^2(t) = \left\{a_2^{(o)}(t)\right\}^2 + \left\{a_3^{(o)}(t)\right\}^2 +\cdots+\left\{a_{n+1}^{(o)}(t)\right\}^2. \quad (198)$$

Hence, the first Strehl ratio becomes

$$SR_1 \approx \exp\left\{(-1)\left[\left\{a_2^{(o)}(t)\right\}^2 + \left\{a_3^{(o)}(t)\right\}^2 +\cdots+\left\{a_{n+1}^{(o)}(t)\right\}^2\right]\right\}. \quad (199)$$

For the simple phase conjugation Strehl ratio, a little more analysis is needed. In the simple conjugation case, what is measured, that is, the set of inbound wavefront Zernike coefficients, is negatively applied to the DM. Therefore, it is desired to have

$$\mathbf{a}^{(m)}(t) = -\mathbf{a}^{(i)}(t). \quad (200)$$

In eq. (200), it is assumed that only tilt compensation is performed. Thus, even though five Zernike modes are used to represent the inbound wavefront, only the negatives of the tilt modes are applied to the mirror. For the simple phase conjugation case, the Kalman filter developed in Chapter 6 is not needed. Recall that the filter was used to estimate the outbound wavefront Zernike coefficients. With simple phase conjugation, no outbound wavefront estimates are required since only the set of inbound wavefront Zernike coefficients is applied to the mirror. Therefore, a weighted least squares algorithm can be used to estimate the inbound wavefront Zernike coefficients from the noisy measurements as described in that which follows. Of course, a Kalman filter could also be built to estimate the inbound wavefront Zernike coefficients, but the performance benefit over the least squares estimate probably would not be substantial.

Unfortunately, the inbound coefficients are not directly measured. Instead, recall that the measured quantity is

$$z_i(t_j) = H_i a^{(i)}(t_j) + v_i(t_j). \tag{201}$$

Therefore, it is necessary to generate an estimate, $\hat{a}^{(i)}(t_j)$, of $a^{(i)}(t_j)$. Hence the value of $\hat{a}^{(i)}(t_j)$ which minimizes the weighted sum of squares of the components of the vector

$$\left[z_i(t_j) - H_i \hat{a}^{(i)}(t_j) \right] \tag{202}$$

is desired. Stated in another fashion, the $\hat{a}^{(i)}(t_j)$, which minimizes the cost function

$$J_{sc} = \frac{1}{2} \left[z_i(t_j) - H_i \hat{a}^{(i)}(t_j) \right]^T W_{sc} \left[z_i(t_j) - H_i \hat{a}^{(i)}(t_j) \right], \tag{203}$$

must be evaluated. In eq. (203), the subscript 'sc' implies simple conjugation and W_{sc} is the weighting matrix. Minimization of the cost function in eq. (203) is accomplished by satisfying the following criteria:

$$\left. \frac{\partial J_{sc}}{\partial \hat{a}^{(i)}(t_j)} \right|_{a=\hat{a}} = \left[\frac{\partial J_{sc}}{\partial \hat{a}_2^{(i)}(t_j)} \quad \frac{\partial J_{sc}}{\partial \hat{a}_3^{(i)}(t_j)} \right]_{a=\hat{a}} = 0^T$$

$$\left. \frac{\partial^2 J_{sc}}{\partial^2 \hat{a}^{(i)}(t_j)} \right|_{a=\hat{a}} \geq 0 \tag{204}$$

where $\hat{a}_2^{(i)}(t_j), \hat{a}_3^{(i)}(t_j)$ are estimates of the x- and y-tilts of the inbound wavefront.

Performing the differentiation in eq. (204) yields

$$\hat{a}^{(i)}(t_j) = \left[H_i^T W_{sc} H_i \right]^{-1} H_i^T W_{sc} z_i(t_j). \tag{205}$$

Therefore, using eq. (200), the desired phase conjugation scheme becomes

$$a^{(m)}(t_j) = -\hat{a}^{(i)}(t_j) = -\left[H_i^T W_{sc} H_i \right]^{-1} H_i^T W_{sc} z_i(t_j). \tag{206}$$

102

The Strehl ratio for this case is the same as that given in eq. (195) with $\mathbf{a}^{(m)}(t)$ replaced by the expression in eq. (206).

The second performance metric that will be used is the RMS phase distortion. This quantity can be expressed as

$$\Phi_{RMS}(t) = \sqrt{\int W(\bar{x})\Phi^2(\bar{x},t)d\bar{x}} \ . \tag{207}$$

For the outbound wavefront,

$$\Phi_{RMS}^{(o)}(t) = \sqrt{\int W(\bar{x})\left[\sum_j a_j^{(o)}(\bar{x})Z_j(\bar{x})\right]^2 d\bar{x}}$$

$$= \sqrt{\int W(\bar{x})\left[a_2^{(o)}(\bar{x})Z_2(\bar{x}) + \cdots + a_{n+1}^{(o)}(\bar{x})Z_{n+1}(\bar{x})\right]^2 d\bar{x}} \ . \tag{208}$$

Expanding the term in brackets and once again using the orthonormality property of the Zernike polynomials gives

$$\Phi_{RMS}^{(o)}(t) = \sqrt{\left\{a_2^{(o)}(t)\right\}^2 + \cdots + \left\{a_{n+1}^{(o)}(t)\right\}^2} = \sqrt{\sum_j \left\{a_j^{(o)}(t)\right\}^2} \ . \tag{209}$$

For the corrected image,

$$\Phi^{(corrected)}(\bar{x},t) = \sum_j -a_j^{(o)}(t)Z_j(\bar{x}) + \sum_k a_k^{(m)}(t)Z_k(\bar{x}). \tag{210}$$

Substituting this expression into eq. (207) yields

$$\Phi_{RMS}^{(corrected)}(t) = \sqrt{\int W(\bar{x})\left[\sum_j -a_j^{(o)}(t)Z_j(\bar{x}) + \sum_k a_k^{(m)}(t)Z_k(\bar{x})\right]^2 d\bar{x}} \ . \tag{211}$$

Performing some simplifications, as detailed in Appendix B, produces the desired result, that is,

$$\Phi_{\text{RMS}}^{(\text{corrected})}(t) = \sqrt{\left[-a_2^{(o)}(t) + a_2^{(m)}(t)\right]^2 + \left[-a_3^{(o)}(t) + a_3^{(m)}(t)\right]^2 + \left\{a_4^{(o)}(t)\right\}^2 + \cdots + \left\{a_{n+1}^{(o)}(t)\right\}^2} \; . \quad (212)$$

This then provides a set of rather simple equations to be used as the metrics in evaluating system performance. The next section discusses the simulations in more detail along with a description of the phase screen.

7.3 Simulation Methodology

A digital simulation of the adaptive optics system was desired in order to evaluate the effectiveness of the LQG controller. This simulation was performed using code written in MATLAB [15]. To begin the simulation, the time history of the covariance matrices was developed. This was accomplished in the following manner: given the form of the system, input, and covariance matrices, $\mathbf{F}$, $\mathbf{G}$, and $\mathbf{P}(t)$,

$$\mathbf{P}(t) = \begin{bmatrix} p_{11}(t) & 0 & p_{13}(t) & 0 \\ 0 & p_{22}(t) & 0 & p_{24}(t) \\ p_{13}(t) & 0 & p_{33}(t) & 0 \\ 0 & p_{24}(t) & 0 & p_{44}(t) \end{bmatrix}, \; \mathbf{F} = \begin{bmatrix} f_{11} & 0 & f_{13} & 0 \\ 0 & f_{22} & 0 & f_{24} \\ f_{31} & 0 & f_{33} & 0 \\ 0 & f_{42} & 0 & f_{44} \end{bmatrix}, \; \mathbf{G} = \begin{bmatrix} g_1 & 0 \\ 0 & g_2 \\ g_3 & 0 \\ 0 & g_4 \end{bmatrix}, \quad (213)$$

form the system of equations $\dot{\mathbf{P}}(t) = \mathbf{F}\mathbf{P}(t) + \mathbf{P}(t)\mathbf{F}^{\mathrm{T}} + \mathbf{G}\mathbf{G}^{\mathrm{T}}$. Performing the algebra required by the differential equation discussed above provides

$$\dot{\mathbf{P}}(t) = \begin{bmatrix} \mathbf{COL1} & \mathbf{COL2} & \mathbf{COL3} & \mathbf{COL4} \end{bmatrix} \quad (214)$$

where

$$\mathbf{COL1} = \begin{bmatrix} 2f_{11}p_{11}(t) + 2f_{13}p_{13}(t) + g_1^2 & 0 & f_{31}p_{11}(t) + (f_{11} + f_{33})p_{13}(t) + f_{13}p_{33}(t) & 0 \end{bmatrix}^{\mathrm{T}}$$
$$\mathbf{COL2} = \begin{bmatrix} 0 & 2f_{22}p_{22}(t) + 2f_{24}p_{24}(t) + g_2^2 & 0 & f_{42}p_{22}(t) + (f_{22} + f_{44})p_{24}(t) + f_{24}p_{44}(t) \end{bmatrix}^{\mathrm{T}} \quad (215)$$
$$\mathbf{COL3} = \begin{bmatrix} f_{31}p_{11}(t) + (f_{11} + f_{33})p_{13}(t) + f_{13}p_{33}(t) & 0 & 2f_{33}p_{33}(t) + 2f_{31}p_{31}(t) + g_3^2 & 0 \end{bmatrix}^{\mathrm{T}}$$
$$\mathbf{COL4} = \begin{bmatrix} 0 & f_{42}p_{22}(t) + (f_{22} + f_{44})p_{24}(t) + f_{24}p_{44}(t) & 0 & 2f_{44}p_{44}(t) + 2f_{42}p_{42}(t) + g_4^2 \end{bmatrix}^{\mathrm{T}} \; .$$

Now, form the linear system

$$\begin{pmatrix} \dot{p}_{11} & \dot{p}_{13} & \dot{p}_{22} & \dot{p}_{24} & \dot{p}_{33} & \dot{p}_{44} \end{pmatrix}^T (t) = \mathbf{A}_{sim} \begin{pmatrix} p_{11} & p_{13} & p_{22} & p_{24} & p_{33} & p_{44} \end{pmatrix}^T (t) + \mathbf{B}_{sim} \mathbf{u} \quad (216)$$

where

$$\mathbf{A}_{sim} = \begin{pmatrix} 2f_{11} & 2f_{13} & 0 & 0 & 0 & 0 \\ f_{31} & f_{11} + f_{33} & 0 & 0 & f_{13} & 0 \\ 0 & 0 & 2f_{22} & 2f_{24} & 0 & 0 \\ 0 & .0 & f_{42} & f_{22} + f_{44} & 0 & f_{24} \\ 0 & 2f_{31} & 0 & 0 & 2f_{33} & 0 \\ 0 & 0 & 0 & 2f_{42} & 0 & 2f_{44} \end{pmatrix}, \quad \mathbf{B}_{sim} = \begin{pmatrix} g_1^2 \\ 0 \\ g_2^2 \\ 0 \\ g_3^2 \\ g_4^2 \end{pmatrix}, \quad (217)$$

and $\mathbf{u} = 1 \; \forall$ time. The linear system in eq. (216) can then be simulated which results in the time history of the covariance matrix. The MATLAB command LSIM [15] can be used, along with other routines, to solve eq. (216).

Having obtained the covariance matrix for each time instant, a phase screen [23] must be generated. This screen represents the random effects of the atmosphere on a wavefront and provides random draws of wavefront phase for each time instant. It is desired that the phase screens have the correct spatial-temporal statistics; that is, those given by the covariance matrices. To achieve this, consider the Cholesky factorization [16] of $\mathbf{P}(t)$,

$$\mathbf{P}(t) = \mathbf{R}_p(t)\mathbf{R}_p^T(t), \quad (218)$$

which can be performed since the covariance matrix is guaranteed to be positive definite. Consider now a random draw of a vector of zero-mean, uncorrelated, unit-variance, Gaussian random variables, $\mathbf{b}(t)$. The covariance of $\mathbf{b}(t)$ is

$$E\left\{\mathbf{b}(t)\mathbf{b}^T(t)\right\} = \mathbf{I} \quad (219)$$

105

where $\mathbf{I}$ is the identity matrix.

Recall that a realization of the wavefront phase can be written as

$\Phi(R\vec{x}, t) = \sum_i a_i(t) Z_i(\vec{x})$. Now consider a random draw of the vector

$\mathbf{a}(t) = \begin{bmatrix} a_2(t) & a_3(t) & \cdots & a_{n+1}(t) \end{bmatrix}$. Note that $a_1(t)$ is not included since only piston

removed quantities are considered. This random draw is accomplished using the vector

$\mathbf{b}(t)$ in the following manner:

$$\mathbf{a}(t) = \mathbf{R}_p(t)\mathbf{b}(t) . \qquad (220)$$

Then, the covariance of $\mathbf{a}(t)$ will match the desired covariance given by $\mathbf{P}(t)$. This can be

seen by considering

$$E\left\{\mathbf{a}(t)\mathbf{a}^T(t)\right\} = E\left\{\mathbf{R}_p(t)\mathbf{b}(t)\left(\mathbf{R}_p(t)\mathbf{b}(t)\right)^T\right\} = E\left\{\mathbf{R}_p(t)\mathbf{b}(t)\mathbf{b}^T(t)\mathbf{R}_p^T(t)\right\}$$

$$= \mathbf{R}_p(t) E\left\{\mathbf{b}(t)\mathbf{b}^T(t)\right\}\mathbf{R}_p^T(t) = \mathbf{R}_p(t)\mathbf{I}\mathbf{R}_p^T(t) = \mathbf{R}_p(t)\mathbf{R}_p^T(t) = \mathbf{P}(t) . \quad (221)$$

By repeated application of this algorithm, a phase screen is generated which has the

desired covariance time history. The vector $\mathbf{a}(t)$, for each time instant, provides the truth

model for the AO system. In the development of the phase screen, the covariance matrix,

not the covariance kernel matrix, was used. Recall that in deriving the atmospheric

model in Chapter 4, the covariance kernel matrix was used. Therefore, the atmospheric

model contains the kernel information. For the phase screen, the Cholesky factorization

requires a positive definite matrix. Since the covariance matrix is positive definite, it was

decided to use this information instead of the covariance kernel matrix; however, the

covariance kernel matrix information is embedded in the phase screen since this was used

to determine the atmospheric model.

Outputs from the simulation consist of time histories of the state variables, the filter's estimate of these states, and filter covariance matrices. Post-simulation data processing produces plots of the outbound wavefront's RMS phase distortion, the RMS phase distortion after wavefront correction, and the Strehl ratios. In addition to these single realizations, a Monte Carlo analysis consisting of 10 runs was conducted to generate ensemble statistics. In terms of ensemble statistics, the following equations were used:

$$\mathbf{m}_e(t) \approx \frac{1}{NR} \sum_{k=1}^{NR} \mathbf{e}_k(t), \tag{222}$$

$$\mathbf{s}_e^2(t) = \frac{1}{NR-1} \sum_{k=1}^{NR} [\mathbf{e}_k(t) - \mathbf{m}_e(t)][\mathbf{e}_k(t) - \mathbf{m}_e(t)]^T, \tag{223}$$

where

NR = number of Monte Carlo runs,

$\mathbf{e}_k(t) = \mathbf{a}_k(t) - \hat{\mathbf{a}}_k(t)$ = error,

k = sample number realization,

$\mathbf{m}_e(t)$ = mean of random process $\mathbf{e}_k(t)$,

and

$\mathbf{s}_e^2(t)$ = variance of random process $\mathbf{e}_k(t)$.

7.4 Simulation Results

In this section, the plots obtained from the simulation will be displayed. Since it is expected that shot noise and photon count entering the HWFS will vary greatly and these are the main components of measurement noise, a parameter study was performed

107

on the noise variance. The robustness of the controller, to a parameter variation, was also evaluated by varying the process noise in the truth model. Recall, when synthesizing the atmospheric model, that the process noise strength was set to $Q_a = I$. In the simulations, Q_a of the truth model was set to I, $10I$, and $20I$. For the larger strengths, the simulation is being conducted with a mismatched model. If the system performs well in these cases, it can be concluded that the complete model is accurate and robust to variations in the Q_a parameter. Lastly, the actuator time constant was varied. It is expected that the actuators for the ABL will be very fast. In fact, it may be possible to model the actuators as a constant gain multiplier, i.e., able to respond instantaneously to changes in command inputs. However, in order to simulate a basic time delay, the actuator time constant was made larger by five orders of magnitude. By no means does this represent a transport delay. In fact, the larger time constant simply delays the application of the conjugate phase to the mirror. Table 3 lists the parameters for the simulations.

	R_i	Q_a	τ_a (sec.)
SIMULATION #1	54.74	I	0.0000075
SIMULATION #2	25.16	I	0.0000075
SIMULATION #3	25.16	10I	0.0000075
SIMULATION #4	25.16	20I	0.0000075
SIMULATION #5	25.16	I	0.75

Table 3. Simulation parameters.

In Table 3, the values of $\mathbf{R}_i$ were determined by the MATLAB [15] simulation. The desired values were 50 and 25. However, with a finite number of samples, precise values are unobtainable.

7.4.1 Simulation Run #1

The first plots shown here are a sample realization of the outbound wavefront's x- and y-tilts from the phase screen with the filter's estimates superimposed. In this figure, the phase screens are in red while the filter estimates are in blue.

Filter error is defined as the true state minus the filter's estimate of the state (state refers to the Zernike coefficients). The filter covariance, $\mathbf{P}_f$, is the filter's indication of the uncertainty in its estimates, as in Eq. (174). The square root of the (j, j) element of the $\mathbf{P}_f$ matrix is what the filter believes to be the one sigma value of its error.
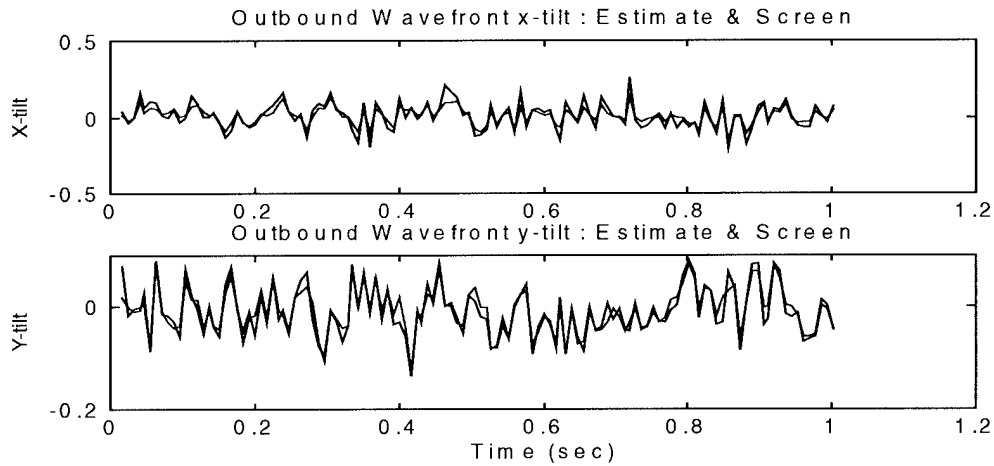
Figure 26. Outbound wavefront tilts: estimates and screen.

Although Figure 26 shows that the filter appears to be tracking the true state, it does not

indicate how the filter error compares with what it thinks are its one sigma values.

Figures 27 and 28 show a single sample time history of the filter error for the x- and y-

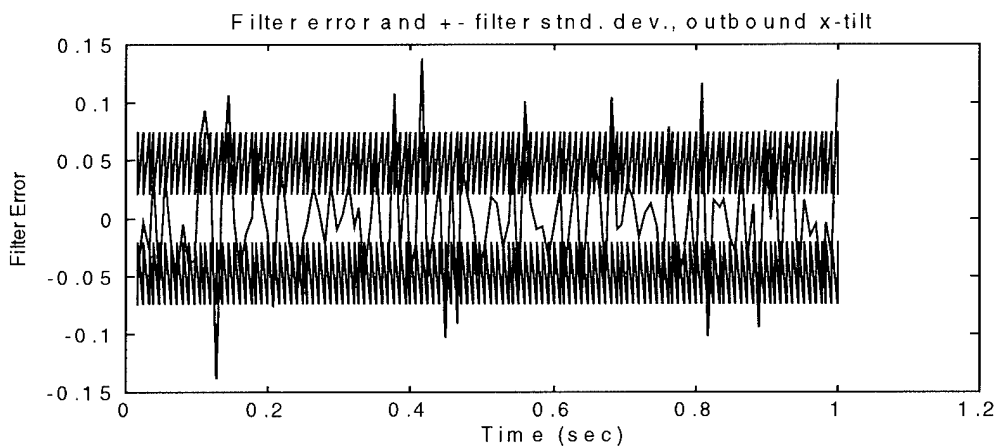tilts, along with the filter computed one sigma values.

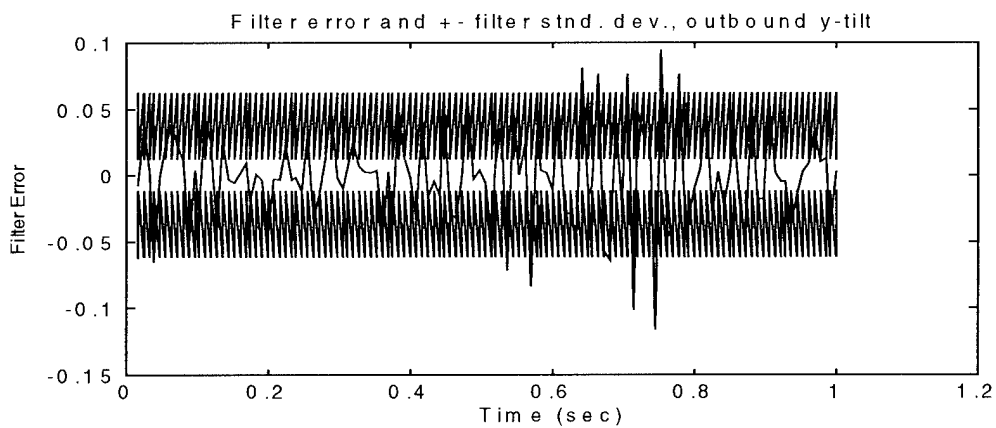Figure 27. Outbound x-tilt filter error and filter standard deviation.

Figure 28. Outbound y-tilt filter error and filter standard deviation.

Looking at these single sample realizations of filter error, it appears that

$\pm\sqrt{\mathbf{P}_f(3,3)}$ and $\pm\sqrt{\mathbf{P}_f(4,4)}$ are reasonable one sigma values for the error and that the

error is zero-mean. Note that the (3,3) and (4,4) elements of the $\mathbf{P}_f$ matrix are used since

the outbound wavefront tilts are the third and fourth components of the state vector $\mathbf{a}(t)$.

The actual values for the filter standard deviations are $\sqrt{\mathbf{P}_f^-(3,3)} = 0.074$ and $\sqrt{\mathbf{P}_f^+(3,3)}$

$= 0.020$ where the superscripts '-' and '+' designate values before measurement update (-

) and after measurement update (+). Also, $\sqrt{\mathbf{P}_f^-(4,4)} = 0.063$ while $\sqrt{\mathbf{P}_f^+(4,4)} = 0.012$.

Time-averaged means and standard deviations of the filter errors were also computed.

For the x-tilt case, the mean error is -0.00023, while for the y-tilt, the mean error is

0.00021. The standard deviation of the x-tilt error is 0.045 and that of the y-tilt error is

0.026. These statistics were computed using the single sample run errors. Thus, they do

not accurately portray the average system performance. In order to get a true description

of the errors, a Monte Carlo analysis must be conducted.

In order to obtain the true error mean and variance, a Monte Carlo analysis

consisting of 10 runs was performed. Statistics were computed using eqs. (222) and

(223). Figures 29 and 30 show the mean and mean ± one standard deviation of the filter

error for the outbound wavefront x- and y- tilts. It appears that the error process is

approximately zero-mean with standard deviations less than the $\pm\sqrt{\mathbf{P}_f(3,3)}$ and

$\pm\sqrt{\mathbf{P}_f(4,4)}$ values from Figures 27 and 28. Hence, it appears that the filter is not

properly tuned. The time-average of the mean x-tilt error is -0.0011, the time-average of

the mean y-tilt error is 0.00093, and the time-averaged standard deviations are 0.037 for

the mean x-tilt error and 0.019 for the mean y-tilt error. Hence, the standard deviations

are much less than the average $\sqrt{P_f^+(j,j)}$ and $\sqrt{P_f^-(j,j)}$ values. Thus, the filter is not
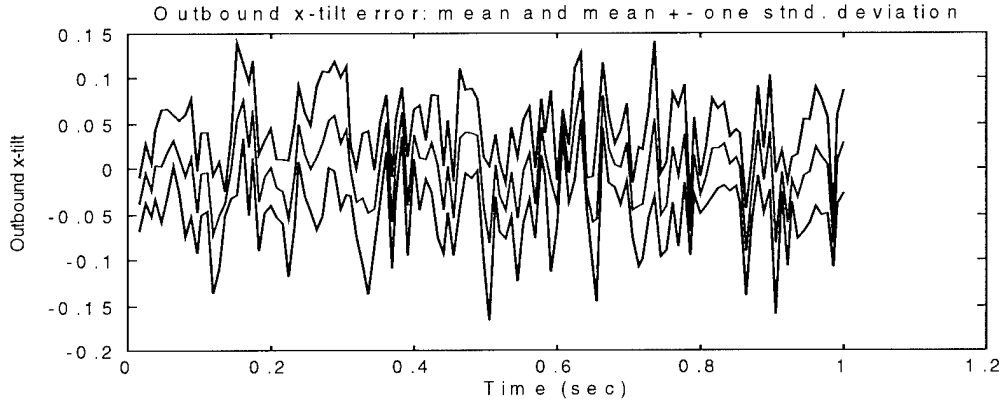
properly tuned.

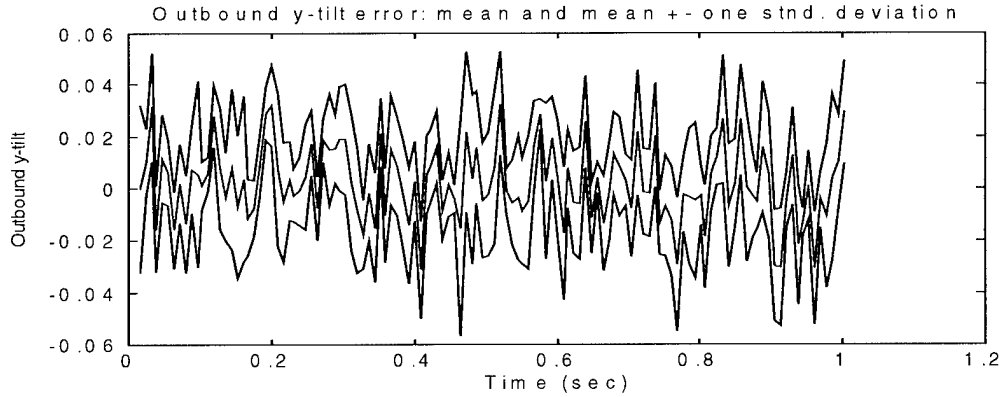Figure 29. Outbound x-tilt, mean and mean ± one standard deviation.

Figure 30. Outbound y-tilt, mean and mean ± one standard deviation.

Figures 31-33 show single sample realizations of the controlled variables. Recall

that it is desired to drive the controlled variables to zero, that is, to have $-a_2^{(o)}(t) = a_2^{(m)}(t)$

and $-a_3^{(o)}(t) = a_3^{(m)}(t)$. Notice that there is a little error in the x-tilt case, but almost zero

error in the y-tilt case. This is because of the planar engagement geometry discussed in Chapter 3. In this engagement, dynamic motion occurs only in the x-direction. Figures 32 and 33 show a sample realization of the controlled variables before (blue) and after (red) correction.
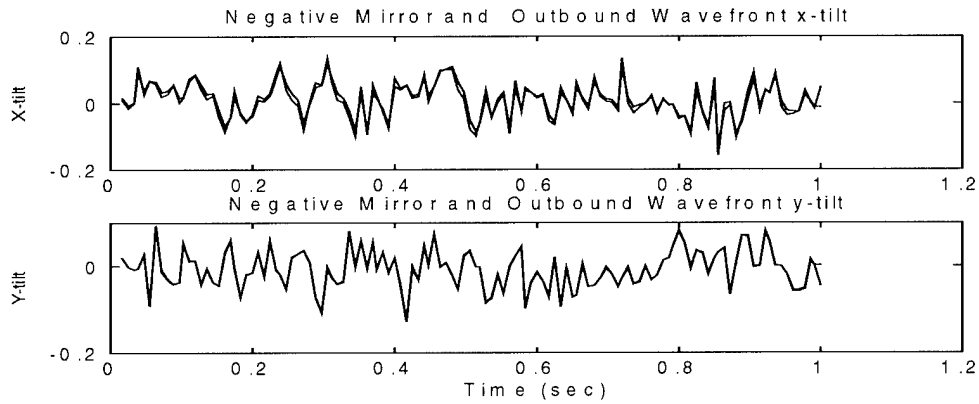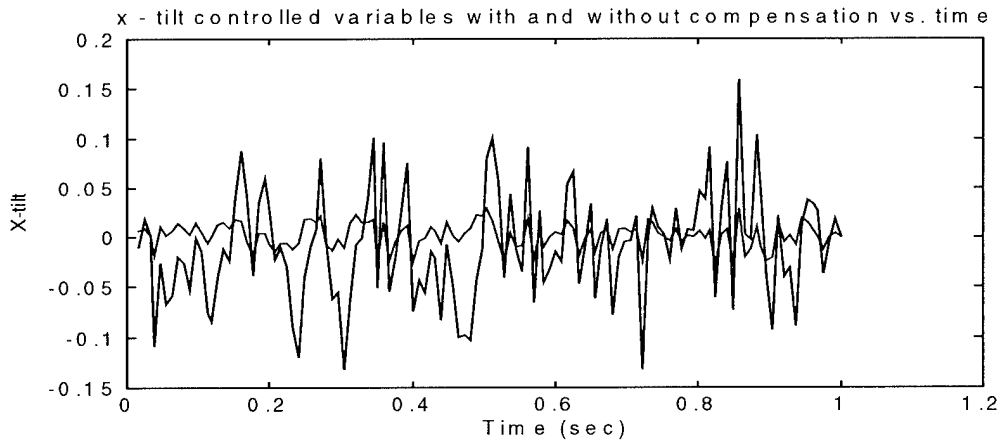

Figure 31. Controlled variables.

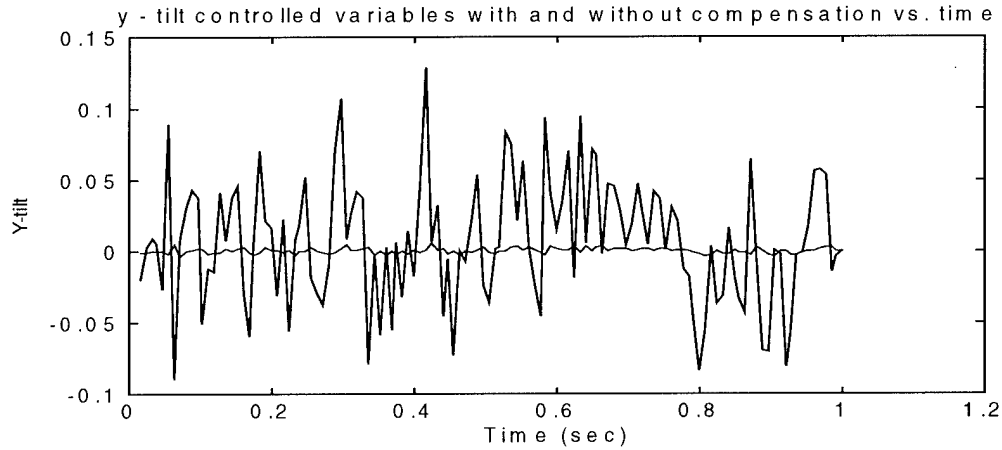Figure 32. X-tilt controlled variables.

Figure 33. Y-tilt controlled variables.

It appears that, after compensation, the tilt variables are much nearer their desired set

point, namely, zero; however, ensemble statistics must also be computed. Figures 34 and

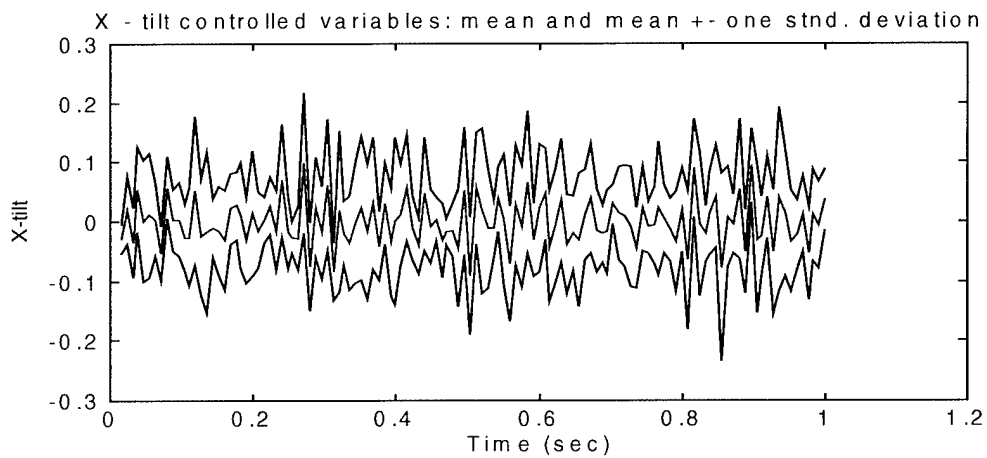35 show the mean and mean ± one standard deviation of the x- and y-tilt controlled

variables.

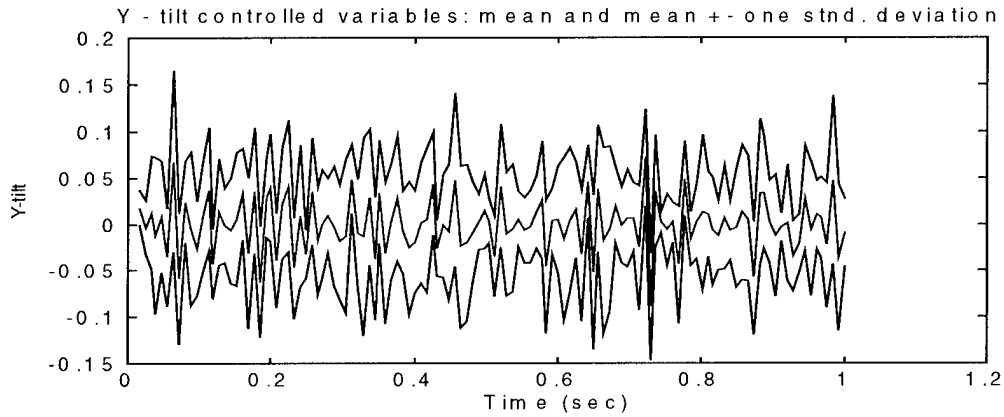Figure 34. X-tilt controlled variables: mean and mean ± one standard deviation.

Figure 35. Y-tilt controlled variables: mean and mean ± one standard deviation.

From these figures, it can be seen that the controlled variables are nearly zero-mean. The y-tilt variance is smaller than that of the x-tilt. Again, this can be attributed to the planar engagement geometry. The time-averaged mean and standard deviation of the x-tilt controlled variables are -0.00096 and 0.031, while the time-averaged mean and standard deviation of the y-tilt controlled variables are -0.00017 and 0.023. Thus, the standard deviation on the y-tilt controlled variables is less than those of the x-tilt controlled variables, with both processes being nearly zero-mean.

Figures 36 and 37 show the Strehl ratio after tilt compensation minus the outbound wavefront Strehl ratio and the simple conjugation Strehl ratio, respectively, along with a zero line for reference. These figures were generated using a single sample realization.
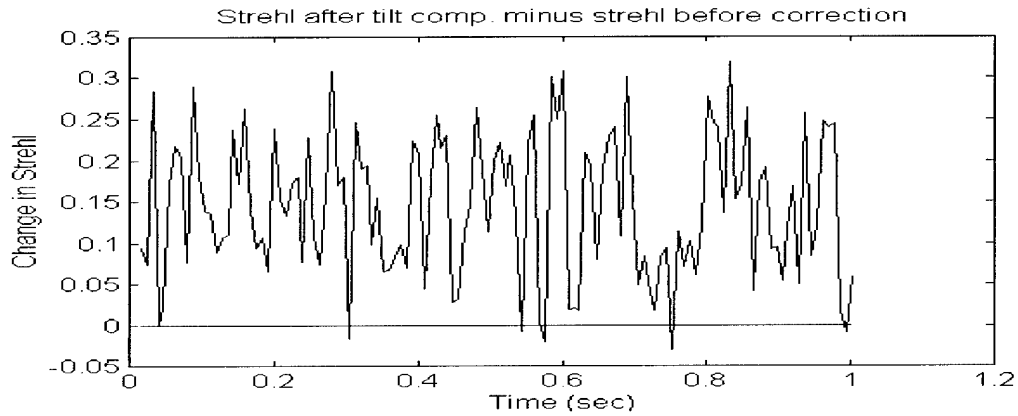
115

Figure 36. Strehl ratio after tilt compensation minus Strehl ratio before correction.
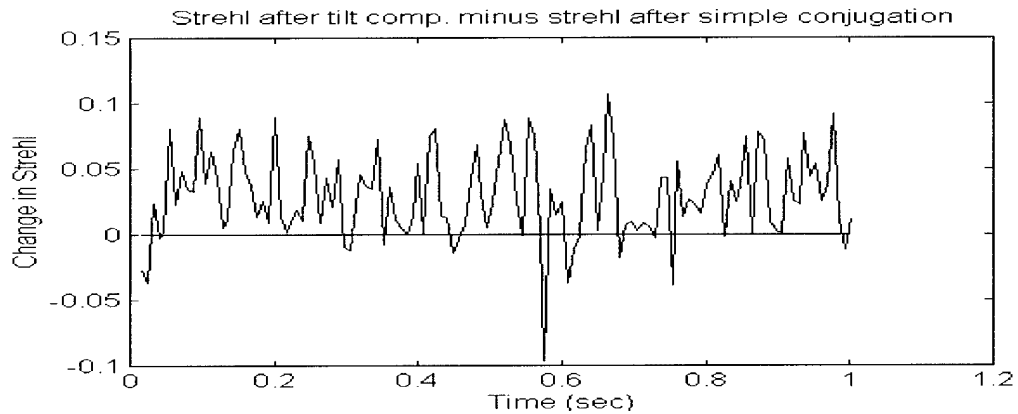

Figure 37. Strehl ratio after tilt compensation minus Strehl ratio after simple conjugation.

Figures 36 and 37 show the improvement in Strehl ratio by using the tilt compensation scheme. From the last two figures, it can be seen that, for this particular single sample realization, the Strehl is increased by an average of 0.144 for the no compensation case and about 0.031 for the simple conjugation case.

116

Figures 38-40 show the mean and mean ± one standard deviation of the three

Strehl ratios. The mean Strehl is 0.484 for the uncompensated case, 0.638 for tilt

compensation, and 0.591 for simple conjugation. Hence, better Strehl ratios are obtained

when the tilt compensation scheme is used. Also, the standard deviation decreases

slightly from the uncompensated case (standard deviation of 0.293), to simple

conjugation (standard deviation = 0.267), to the tilt compensation case (standard
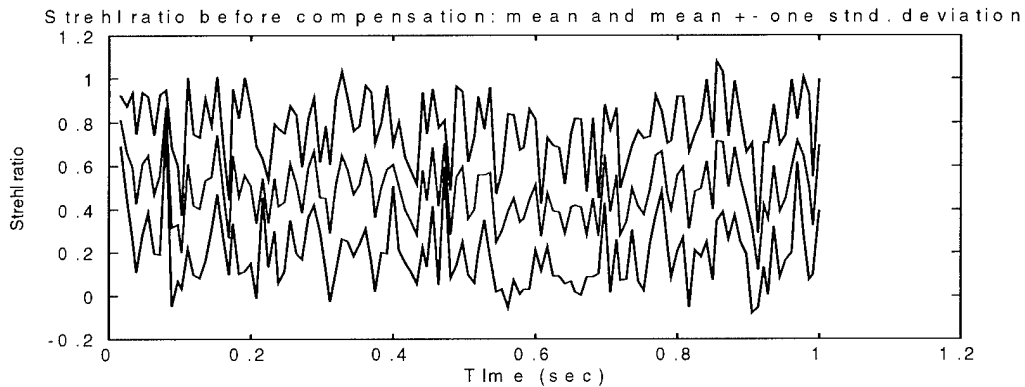
deviation = 0.245).
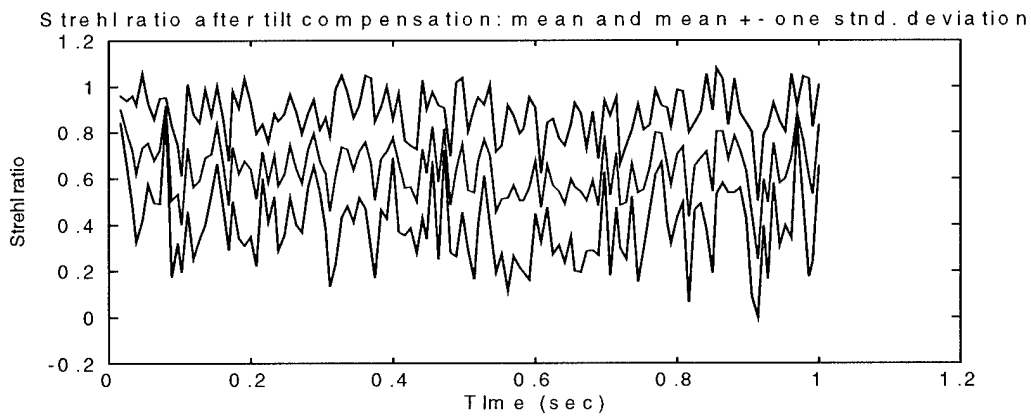

Figure 38. Uncompensated Strehl ratio.

Figure 39. Tilt compensation Strehl ratio.

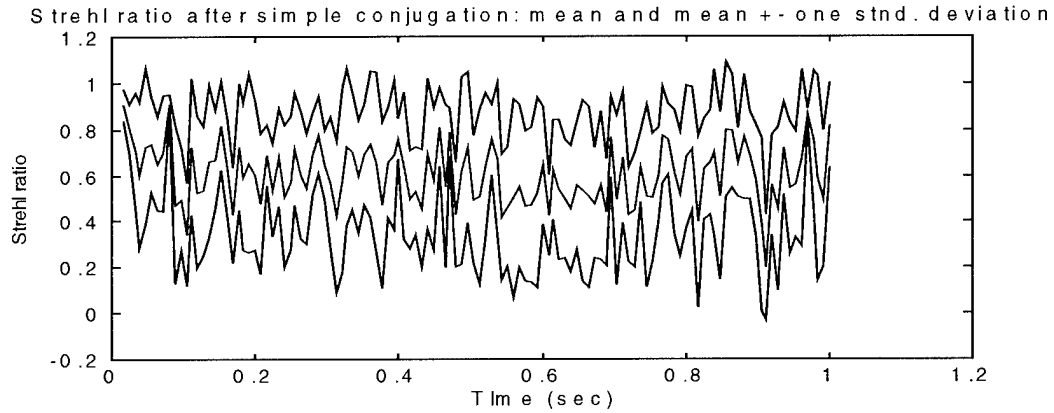Strehl ratio after simple conjugation: mean and mean +- one stnd. deviation

Figure 40. Simple phase conjugation Strehl ratio.

Figure 41 shows a single sample realization of the RMS phase distortion of the outbound (red) and compensated (blue) wavefronts.
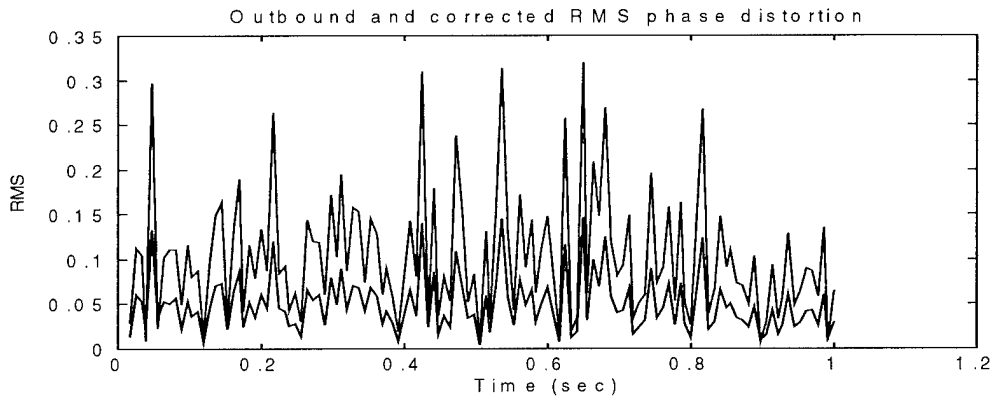

Figure 41. RMS phase distortions.

It appears that the RMS phase distortion is decreased using tilt compensation. Figures 42 and 43 show the RMS statistics from the Monte Carlo analysis. It can be seen that the mean and variance are significantly reduced by employing tilt compensation.
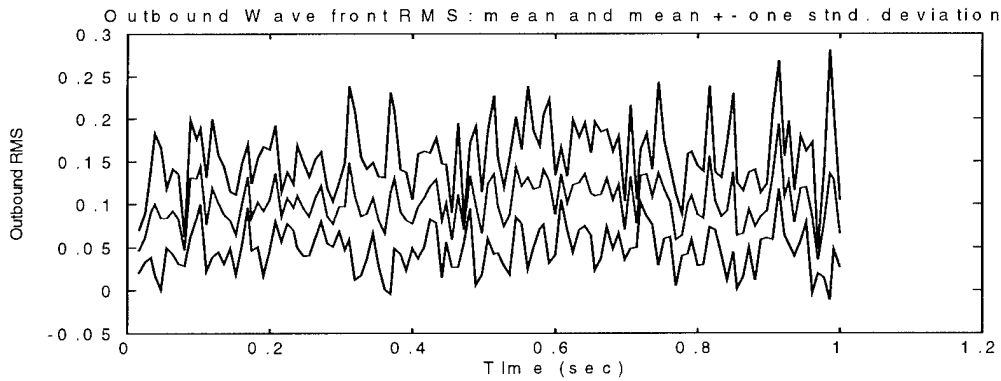
Outbound Wavefront RMS: mean and mean +- one stnd. deviation

Figure 42. Outbound wavefront RMS statistics.

Corrected Wavefront RMS: mean and mean +- one stnd. deviation
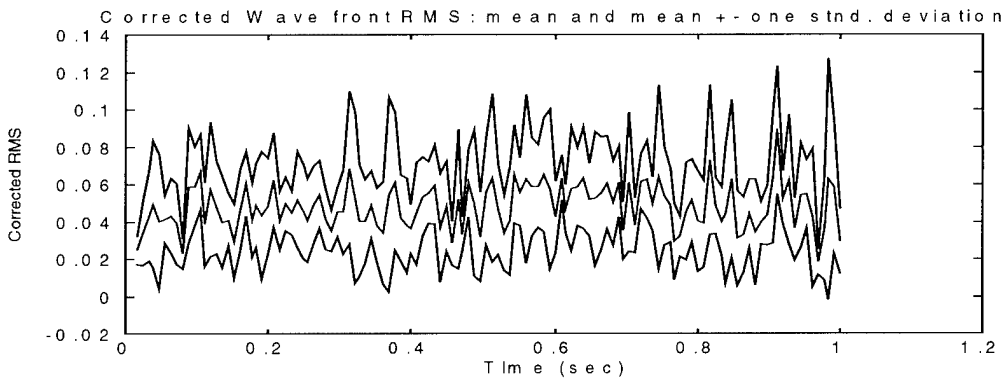
Figure 43. Corrected wavefront RMS statistics.

For the outbound wavefront, the time-averaged mean and standard deviation are 0.102

and 0.055, respectively. For the corrected wavefront, the time-averaged mean and

standard deviation are 0.048 and 0.024. Hence, the RMS means and variances are

reduced using tilt compensation.

In conclusion, the system seems to be performing adequately for this particular

set of parameters, i.e., measurement and process noise strength and actuator time

constant. That is, the Strehl ratios and RMS phase distortions are notably better when tilt compensation is applied. Table 4 displays the time-averaged means and standard deviations of the plots displayed in this section.

However, since the measurement noise variance is unknown, more simulations must be run. Simulation set #2 examines the effects of decreasing the measurement noise variance. In this case, the filter will weigh the measurements more heavily and place less emphasis on the internal model.

Figure #	Variable Name	Mean	Std. Deviation
27	X-tilt filter error	-0.00023	0.045
28	Y-tilt filter error	0.00021	0.026
29	Outbound x-tilt	-0.0011	0.037
30	Outbound y-tilt	0.00093	0.019
34	X-tilt controlled variables	-0.00096	0.031
35	Y-tilt controlled variables	-0.00017	0.023
38	Uncompensated Strehl ratio	0.484	0.293
39	Tilt compensation Strehl ratio	0.638	0.245
40	Simple phase conjugation Strehl ratio	0.591	0.267
42	Outbound wavefront RMS	0.102	0.055
43	Corrected wavefront RMS	0.048	0.024

Table 4. Statistics for run #1 plots.

7.4.2 Simulation Run #2

In this case, R_i is nearly one-half that of run #1. Figure 44 shows a single sample realization of tilts while Figures 45 and 46 show single sample realizations of filter error and filter computed one sigma values.
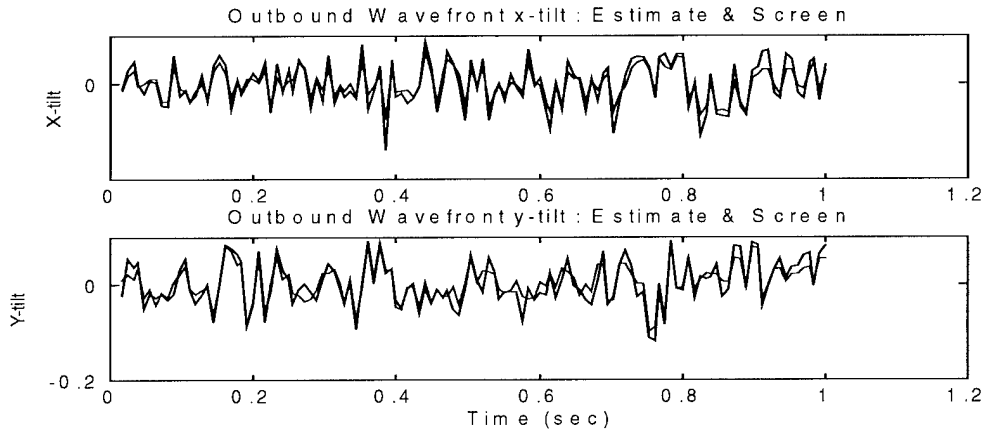
Figure 44. Outbound wavefront tilts: estimates and screen.

The mean errors are 0.00019 and -0.0002 for the x- and y-tilts, respectively. In this case, the filter error standard deviations are smaller than those of the filter errors shown in Figures 27 and 28. Recall that in simulation run #1, the standard deviations were 0.045 (x-tilt) and 0.026 (y-tilt). Here, the standard deviation of the x-tilt filter error is 0.033 while that of the y-tilt is 0.018. The filter computed standard deviations are: $\sqrt{\mathbf{P}_f^+(3,3)} =$ 0.014, $\sqrt{\mathbf{P}_f^-(3,3)} = 0.052$, $\sqrt{\mathbf{P}_f^+(4,4)} = 0.008$, and $\sqrt{\mathbf{P}_f^-(4,4)} = 0.045$. As compared to simulation run #1, the filter computed standard deviations are less which implies that the filter is more confident about its estimates.
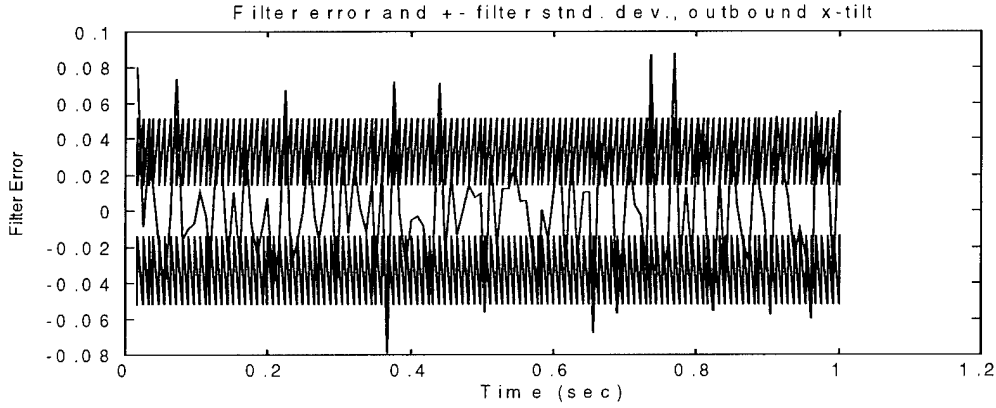
121

Figure 45. Outbound x-tilt filter error and filter standard deviation.
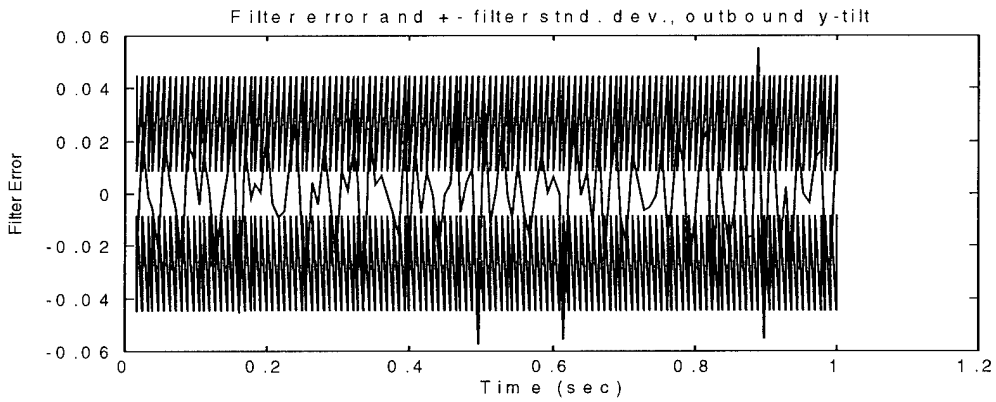
Figure 46. Outbound y-tilt filter error and filter standard deviation.

Figures 47 and 48 show the mean and mean ± one standard deviation of the outbound tilts. The errors are approximately zero-mean and once again, the variances are smaller than those displayed in simulation run #1. For run #2, the standard deviations of the error are 0.03 (x-tilt) and 0.017 (y-tilt). Those for run #1 were 0.037 (x-tilt) and 0.019 (y-tilt). Also, the standard deviations are nearly equal to the $\pm\sqrt{\mathbf{P}_f(3,3)}$ and $\pm\sqrt{\mathbf{P}_f(4,4)}$ values. This would imply that the filter is better tuned.
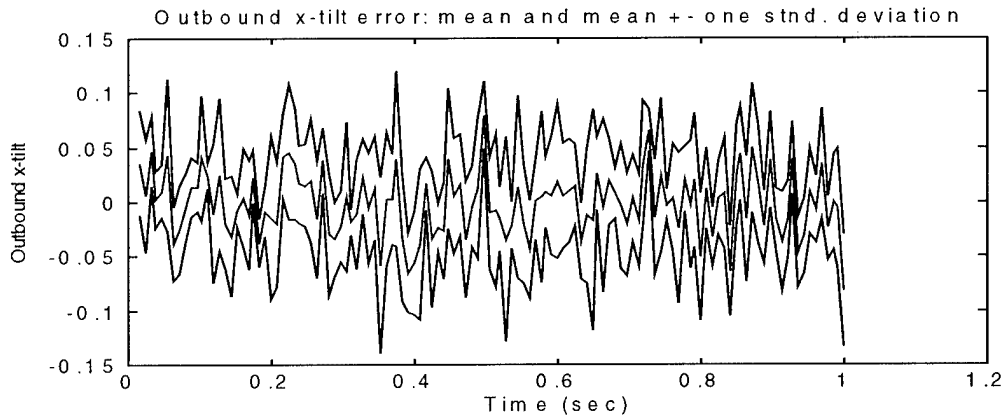
Figure 47. Outbound x-tilt, mean and mean ± one standard deviation.
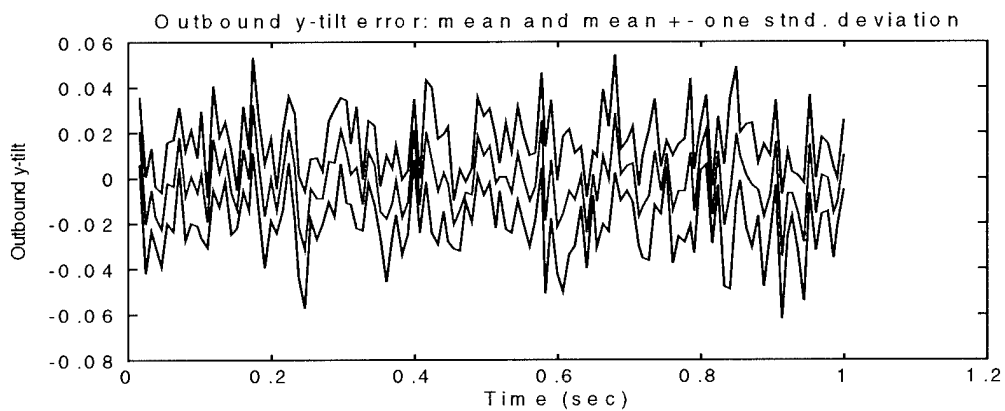
Figure 48. Outbound y-tilt, mean and mean ± one standard deviation.

Figure 49 shows a single sample realization of the controlled variables, while

Figures 50 and 51 show the mean and mean ± one standard deviation of the controlled

variables. Here, the means and variances are smaller than those displayed in run #1. The

time-averaged means of the controlled variables are as follows (those from run #1 are in

parenthesis): -0.00016 (-0.00096) for x-tilt and 0.00015 (-0.00017) for y-tilt. The time-

averaged standard deviations are (run #1 values in parenthesis): 0.027 (0.031) for x-tilt

and 0.017 (0.023) for y-tilt.
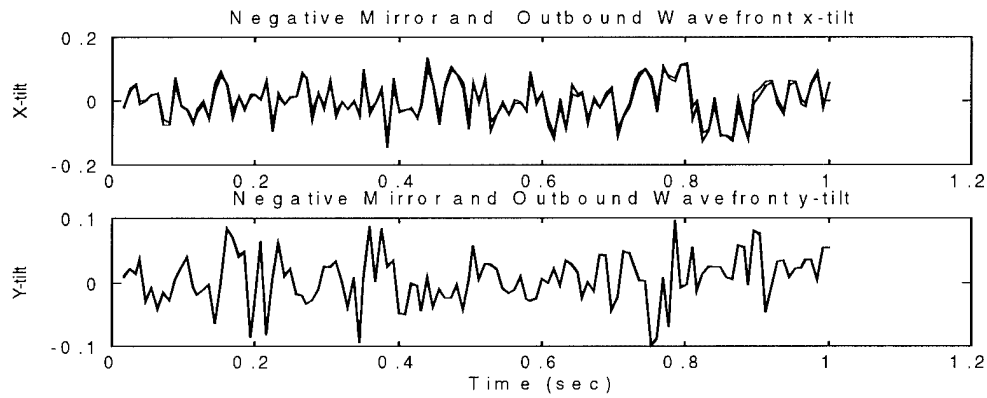
Figure 49. Controlled variables.
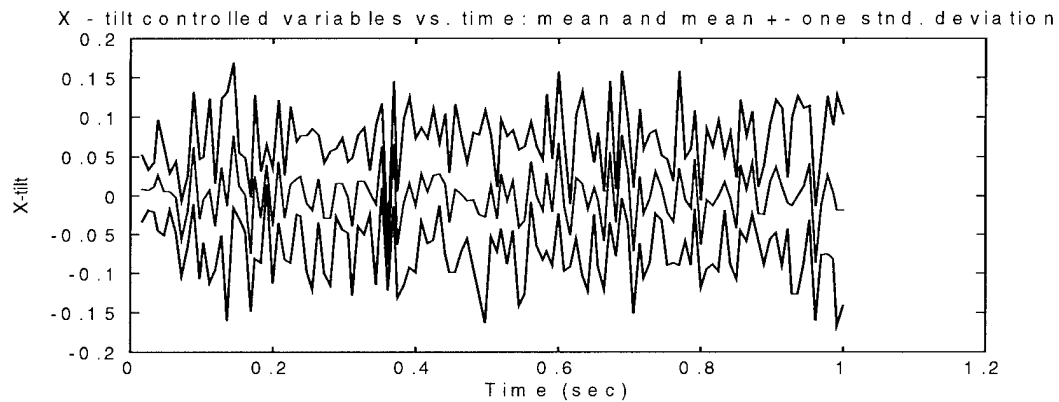
Figure 50. X-tilt controlled variables.
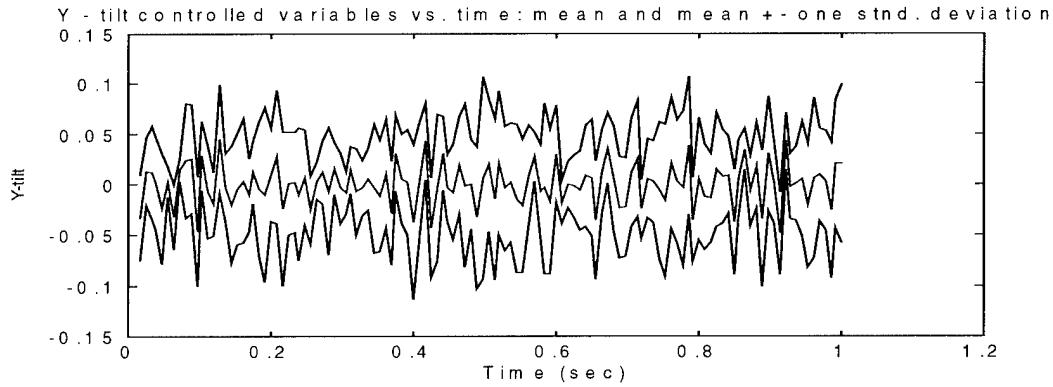
Figure 51. Y-tilt controlled variables.

Figures 52 and 53 show the differences in Strehl ratios from a single sample

realization. There is an increase in the gain in Strehl in this situation as compared to run

#1. Hence, the controller seems to perform better with this set of simulation parameters.

This performance should be expected since the measurements are more precise. In fact,

the average change in Strehl ratio is 0.164 for no compensation and 0.038 for simple

conjugation. For run #1, the increases were 0.144 and 0.031.
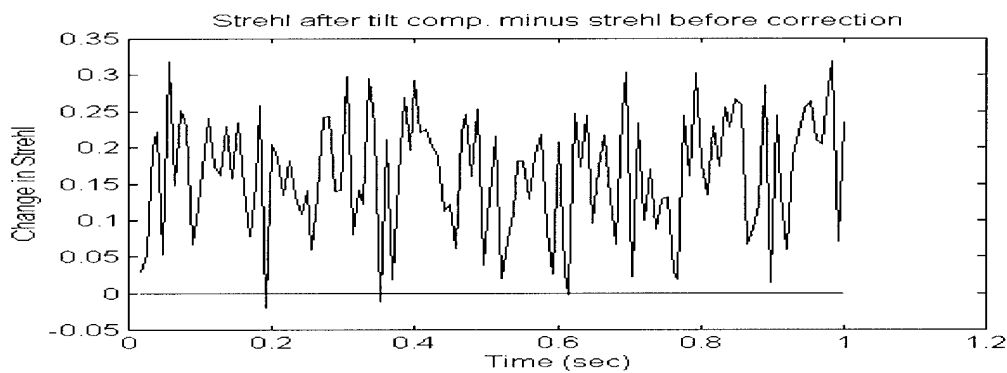
Figure 52. Strehl ratio after tilt compensation minus Strehl ratio before correction.
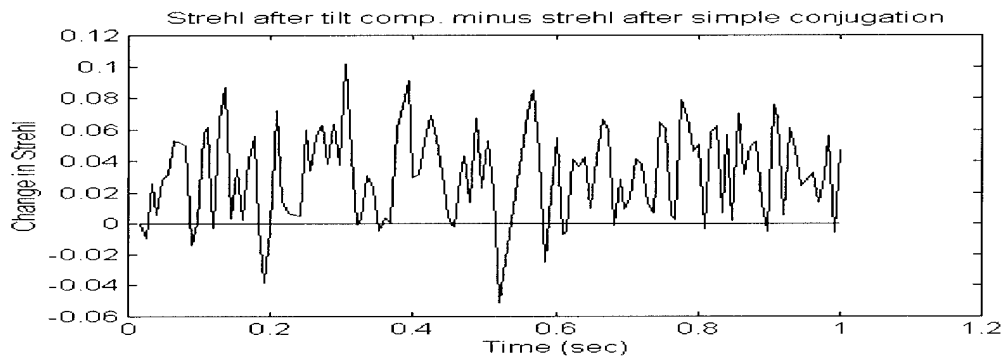
Figure 53. Strehl ratio after tilt compensation minus Strehl ratio after simple conjugation.

Figures 54-56 show the mean and mean ± one standard deviation of the Strehl ratios.
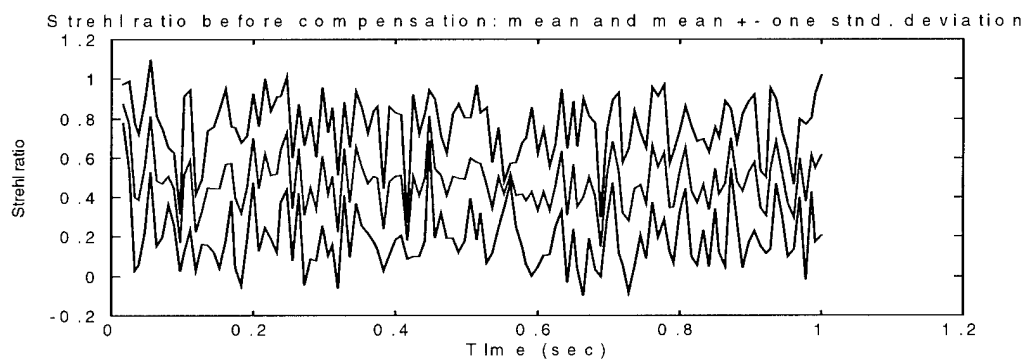
Figure 54. Uncompensated Strehl ratio.
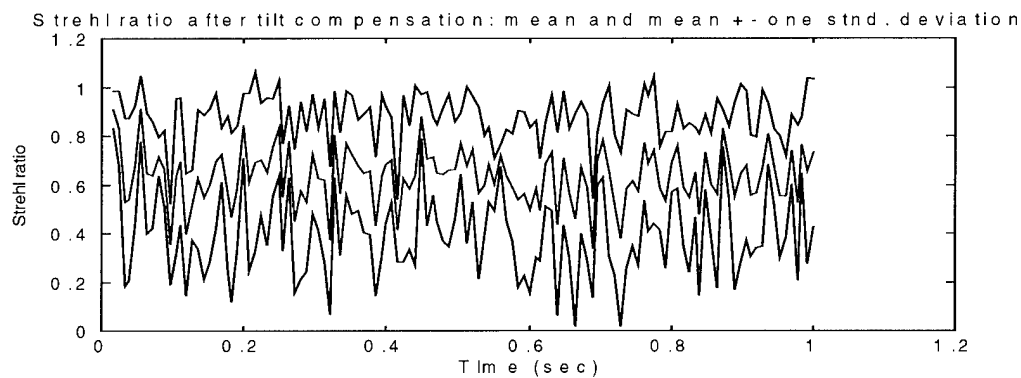
Figure 55. Tilt compensation Strehl ratio.
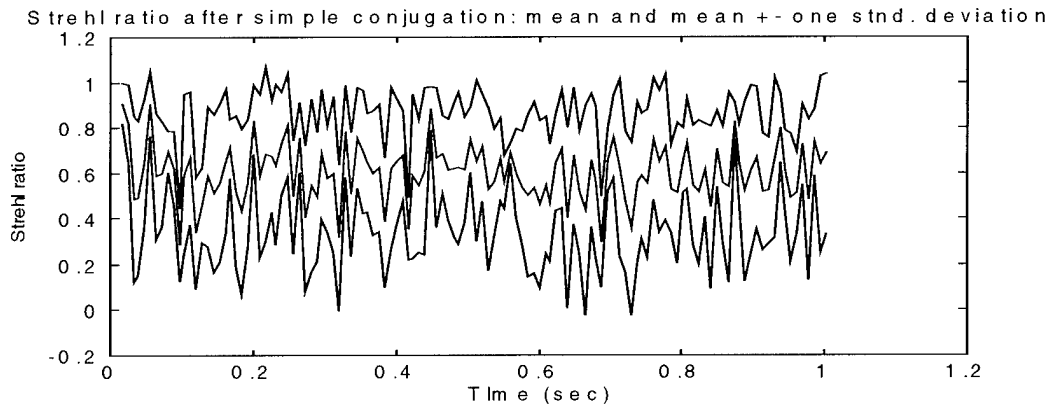
Figure 56. Simple phase conjugation Strehl ratio.

The time-averaged mean Strehl ratios are (run #1 values in parenthesis): 0.481 uncompensated, 0.621 (0.591) simple phase conjugation, and 0.643 (0.638) for tilt compensation. Hence, the Strehl ratios have increased. The time-averaged standard deviations are (run #1 values in parenthesis) are: 0.285 uncompensated, 0.265 (0.267) simple conjugation, and 0.242 (0.245) for tilt compensation. Thus, the Strehl ratios have increased and the variances decreased as compared to run #1.

Figures 57-59 show the RMS phase distortion and the associated Monte Carlo statistics. Note that the corrected RMS values are smaller than those in run #1. Recall that with $R_i = 25.16$ instead of 54.74, more emphasis is placed on the measurements and less is placed on the internal model.
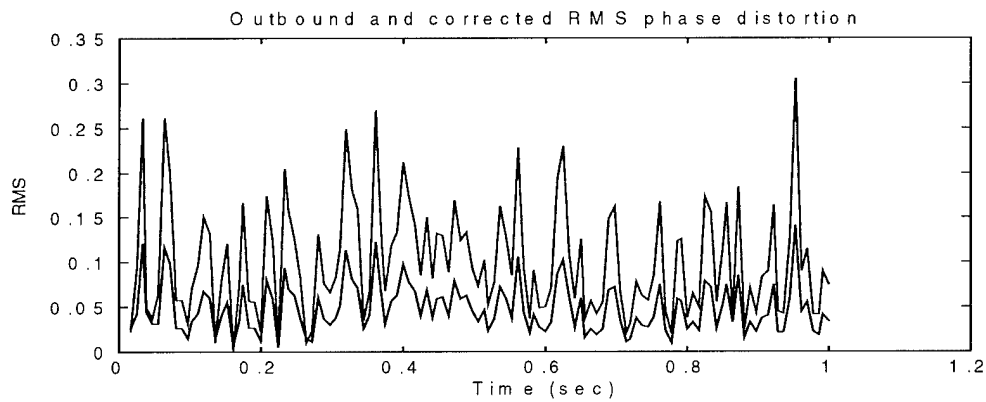
Figure 57. RMS phase distortions.
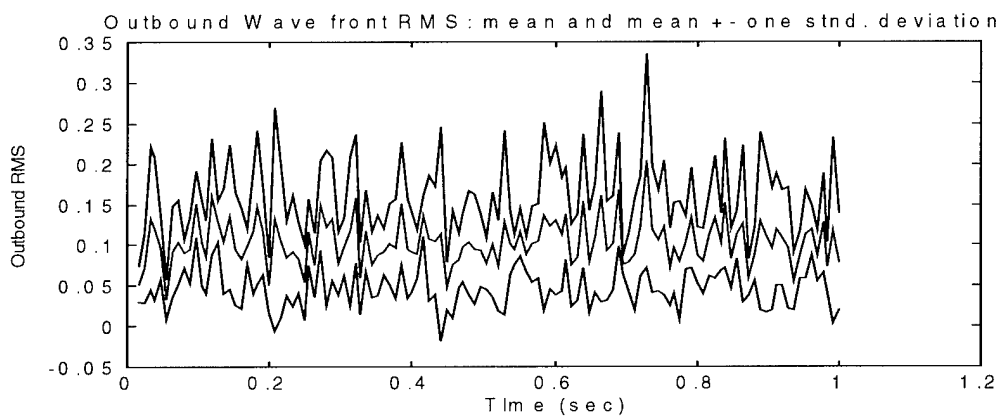
Figure 58. Outbound wavefront RMS statistics.
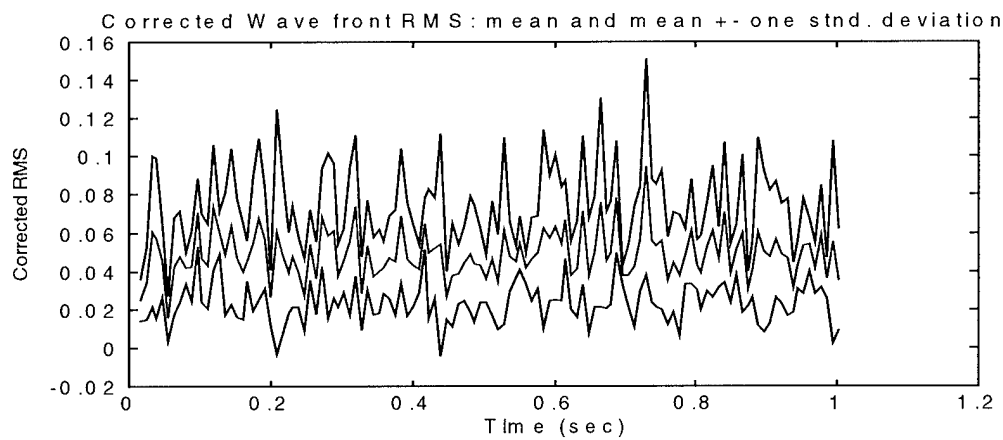
Figure 59. Corrected wavefront RMS statistics.

128

The time-averaged mean RMS values are (run #1 values in parenthesis): 0.104 for the

outbound wavefront and 0.045 (0.048) for the corrected wavefront. The time-averaged

RMS standard deviations are: 0.051 (0.055) for the outbound wavefront and 0.021

(0.024) for the corrected wavefront.

In this case, system performance is better than in run #1. That is, more accurate

estimates of the outbound wavefront Zernike coefficients are made. This, in turn, results

in better regulation of the controlled variables and hence, better Strehl ratios and RMS

phase distortions. Table 5 summarizes the results of this simulation run.

Figure #	Variable Name	Mean	Std. Deviation
45	X-tilt filter error	0.00019	0.033
46	Y-tilt filter error	-0.0002	0.018
47	Outbound x-tilt	-0.00022	0.03
48	Outbound y-tilt	0.00015	0.017
50	X-tilt controlled variables	-0.00016	0.027
51	Y-tilt controlled variables	0.00015	0.017
54	Uncompensated Strehl ratio	0.481	0.285
55	Tilt compensation Strehl ratio	0.643	0.242
56	Simple phase conjugation Strehl ratio	0.621	0.265
58	Outbound wavefront RMS	0.104	0.051
59	Corrected wavefront RMS	0.045	0.021

Table 5. Statistics for run #2 plots.

Now, the robustness of the Kalman filter to variations in the process noise strength will

be tested. This simulation is used to determine the effects of model mismatches upon the

operation of the system. Simulation run #3 displays these results.

7.4.3 Simulation Run #3

Recall that in this case, the process noise of the truth model, Q_a, was set to $10I$, while the filter was run with $Q_a = I$. Therefore, the simulation is being run to evaluate the robustness of the filter to variations in the process noise strength. Figure 60 shows a sample realization of the outbound tilts.
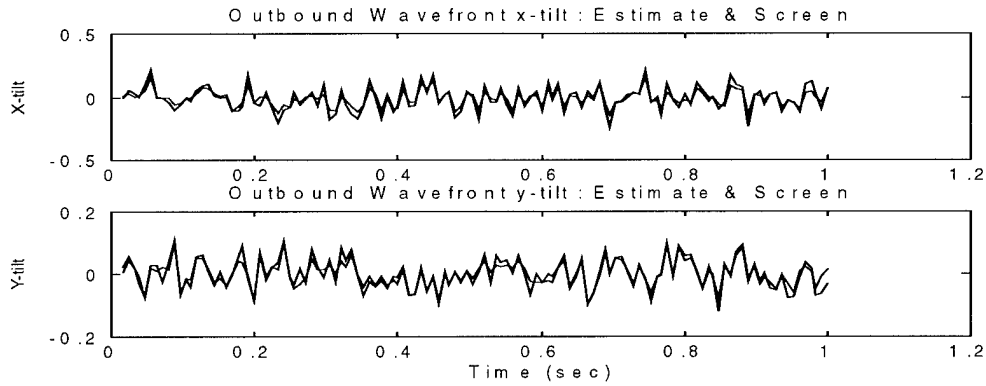
Figure 60. Outbound wave front tilts: estimates and screen.

It still appears that the filter is accurately estimating the outbound wavefront coefficients. Figures 61 and 62 show a single realization of filter error along with the filter computed one sigma values. The mean errors are -0.00021 for x-tilt and 0.00041 for y-tilt. Thus, the errors are still nearly zero-mean; however, the standard deviations of the errors are much greater than in the previous simulation run. In fact, the x-tilt standard deviation is 0.057 while the y-tilt standard deviation is 0.036. For run #2, the standard deviations were 0.033 (x-tilt) and 0.018 (y-tilt). Hence, the model inadequacies are causing problems with the estimation of the outbound wavefront Zernike coefficients. In other

130

words, the filter underestimates the size of its own errors since $Q_a = 10\,I$ for the truth

model and $Q_a = I$ for the filter.
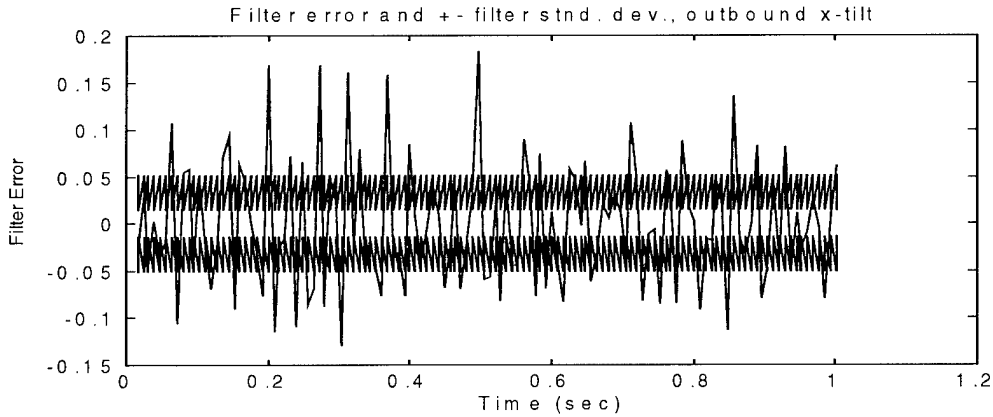
Figure 61. Outbound x-tilt filter error and filter standard deviation.
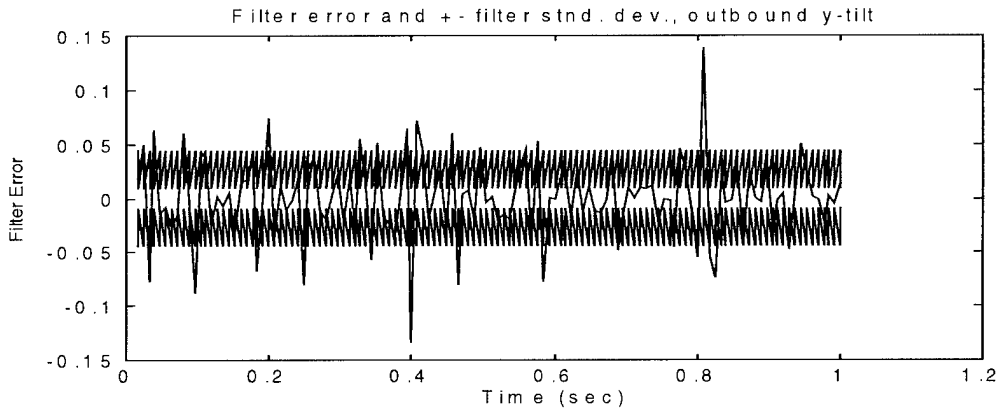
Figure 62. Outbound y-tilt filter error and filter standard deviation.

Figures 63 and 64 show the mean and mean $\pm$ one standard deviation of the error in the

outbound tilts. The errors are zero-mean, but the error variances are larger than those in

run #2. The error standard deviations for this run are (run #2 values in parenthesis):

0.054 (0.03) for the x-tilt and 0.032 (0.017) for the y-tilt.

131
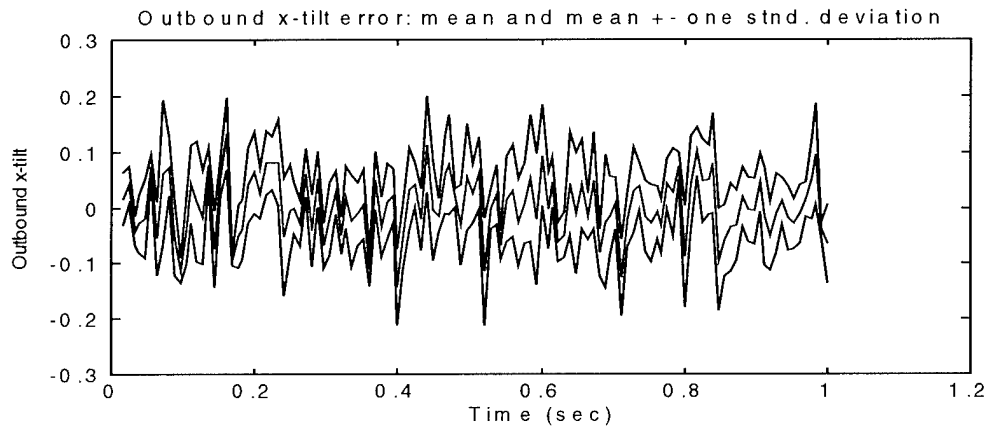
Figure 63. Outbound x-tilt error.
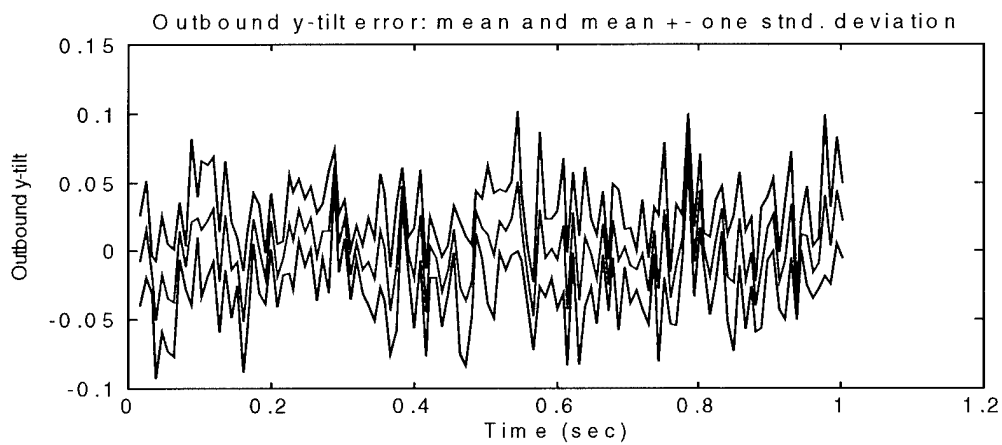
Figure 64. Outbound y-tilt error.

Figures 65-67 display the controlled variables. The controlled variables are approximately zero-mean, however, the variances are significantly greater as compared to run #2.
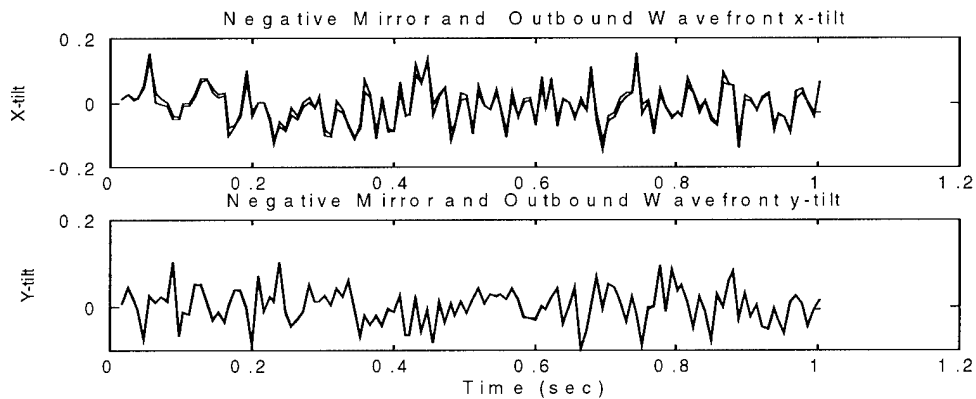
Figure 65. Controlled variables.
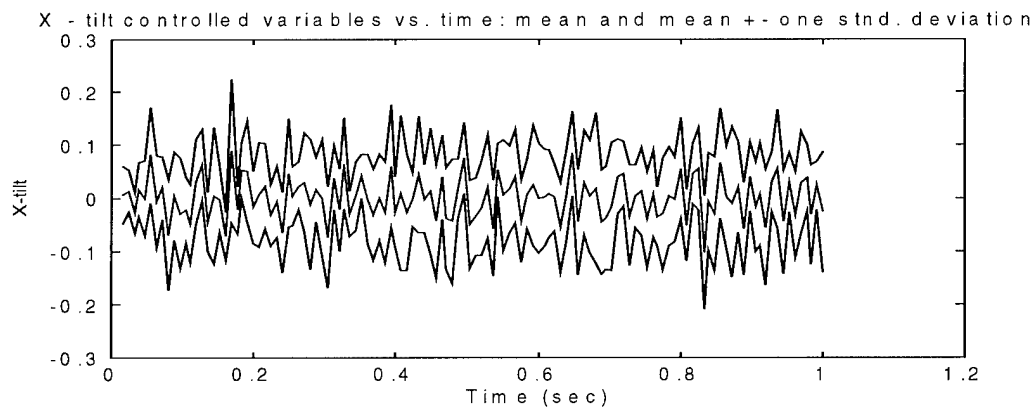
Figure 66. X-tilt controlled variables.
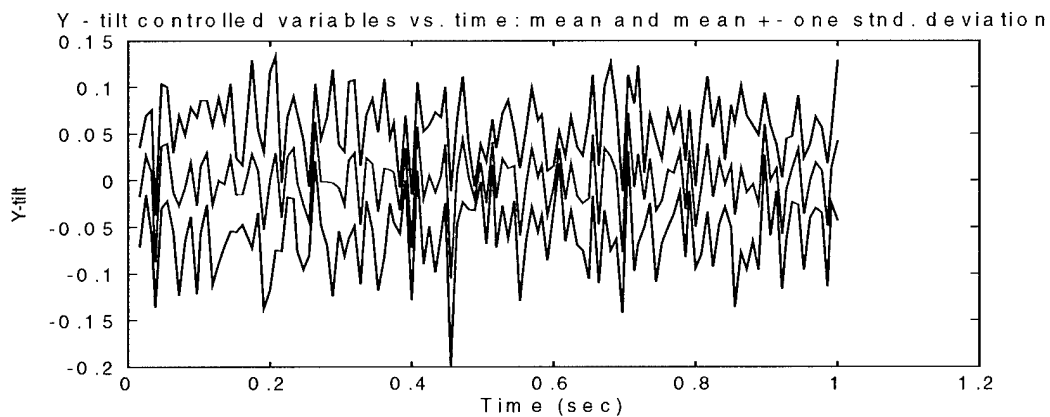
Figure 67. Y-tilt controlled variables.

133

Although the standard deviations of the controlled variables are larger than those

displayed in simulation run #2, the controller is still regulating the controlled variables to

zero. The standard deviations of the controlled variables are (run #2 values in

parenthesis): 0.039 (0.027) for the x-tilt and 0.031 (0.017) for the y-tilt.

Figures 68-70 show ensemble statistics of the Strehl ratios. Although the

compensated Strehl ratios are still high, they are worse than in the previous two cases.

The tilt compensated time-averaged mean Strehl ratio is 0.495, while for run #2 the value

was 0.643. The simple phase conjugation Strehl ratio is 0.47, while for run #2 it was

0.621. However, the compensated Strehls are better than the uncompensated case (Strehl

of 0.44). This would imply that even with model inadequacies of the magnitude

described in this simulation run, tilt compensation and simple conjugation are better than

no compensation.
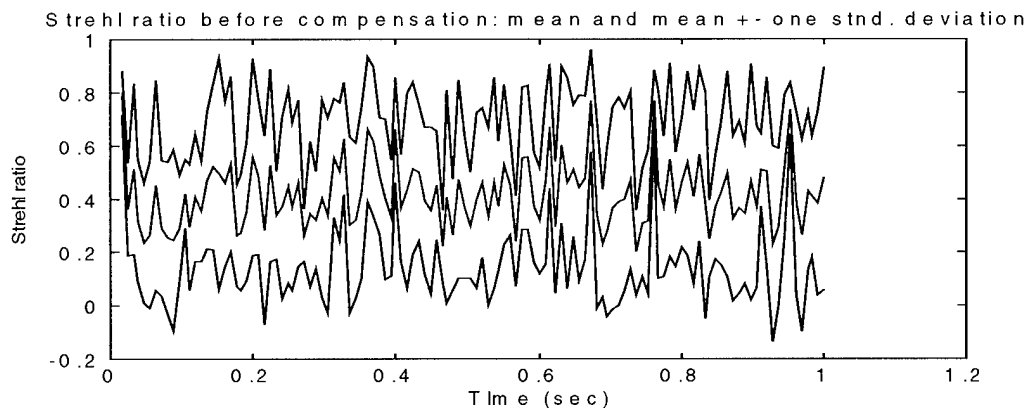
Figure 68. Uncompensated Strehl ratio.
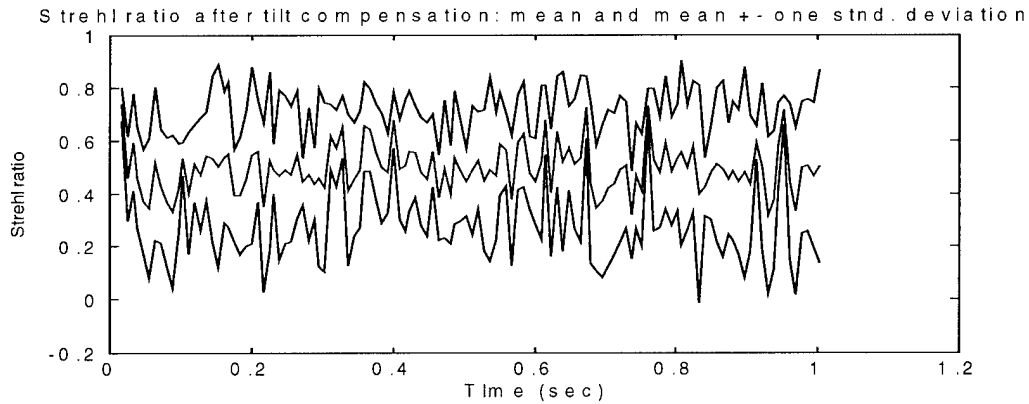
Figure 69. Tilt compensation Strehl ratio.
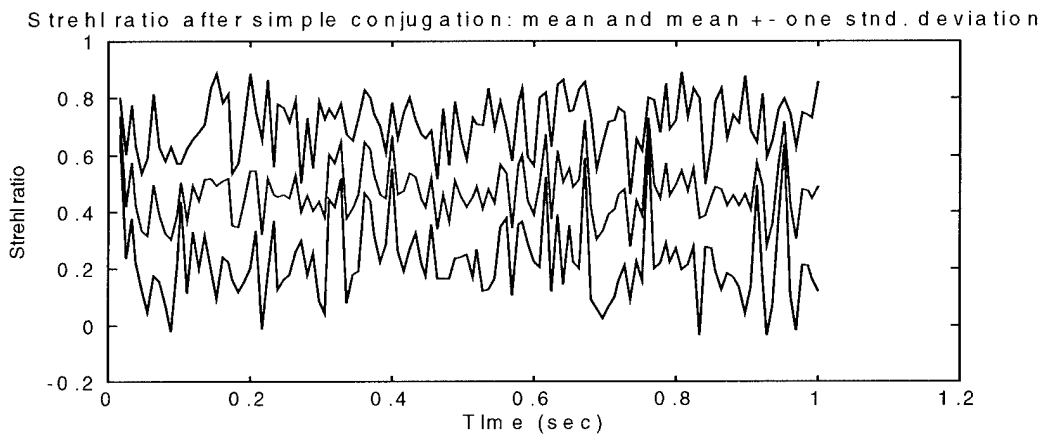
Figure 70. Simple conjugation Strehl ratio.

System performance is definitely worse in this case as compared to run #2, however, it appears that the controller is rather robust to variations in the Q_a parameter. That is, the Strehl ratios are higher for the tilt compensation and simple conjugation cases as compared to no compensation. Hence, even if the atmospheric model does not provide a precise representation of the physical plant, system performance can be enhanced by applying tilt compensation. Table 6 summarizes this simulation run.

Figure #	Variable Name	Mean	Std. Deviation
61	X-tilt filter error	-0.00021	0.057
62	Y-tilt filter error	0.00041	0.036
63	Outbound x-tilt	-0.00029	0.054
64	Outbound y-tilt	0.00026	0.032
66	X-tilt controlled variables	-0.00082	0.039
67	Y-tilt controlled variables	-0.00021	0.031
68	Uncompensated Strehl ratio	0.44	---
69	Tilt compensation Strehl ratio	0.495	---
70	Simple phase conjugation Strehl ratio	0.47	---

Table 6. Statistics for run #3 plots.

7.4.4 Simulation Run #4

In this case, Q_a of the truth model was set to 20**I**. Hence, the model uncertainties

are more severe than those in simulation run #3. Figure 71 shows a single sample

realization of the x- and y- tilts.
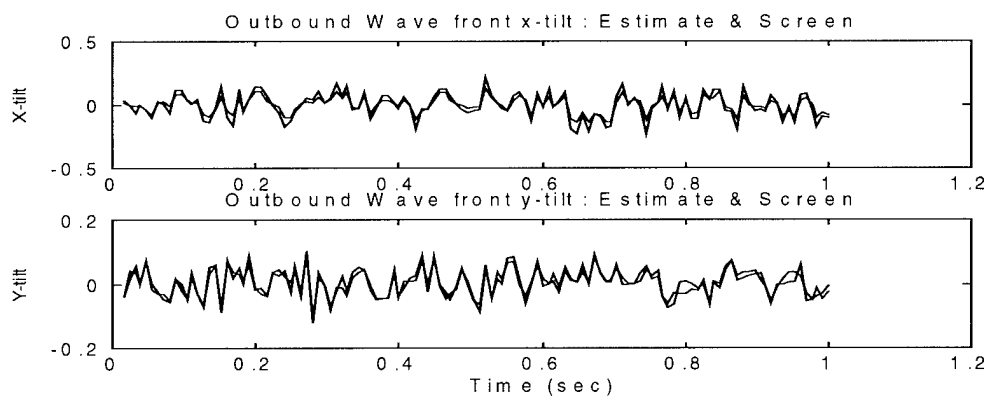
Figure 71. Outbound wavefront tilts: estimate and screen.

Figures 72 and 73 show a single realization of filter error along with the filter computed

one sigma values while Figures 74 and 75 show the mean and mean ± one standard

deviation of the error in the outbound tilts.
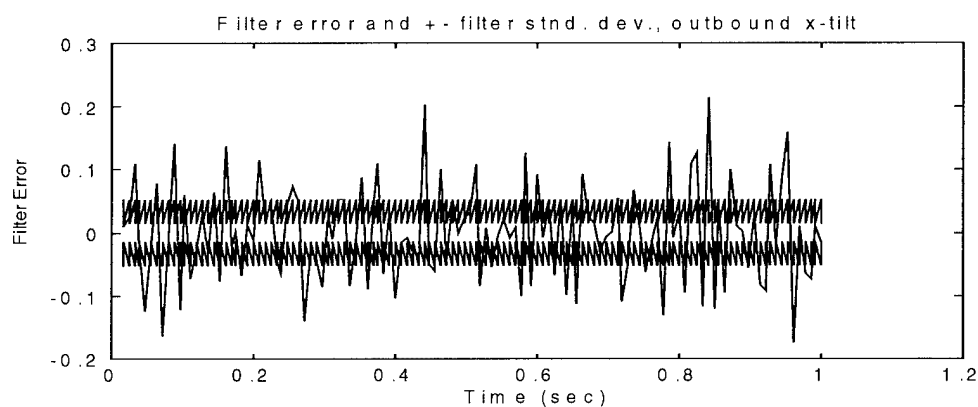
Figure 72. Outbound x-tilt filter error and filter standard deviation.
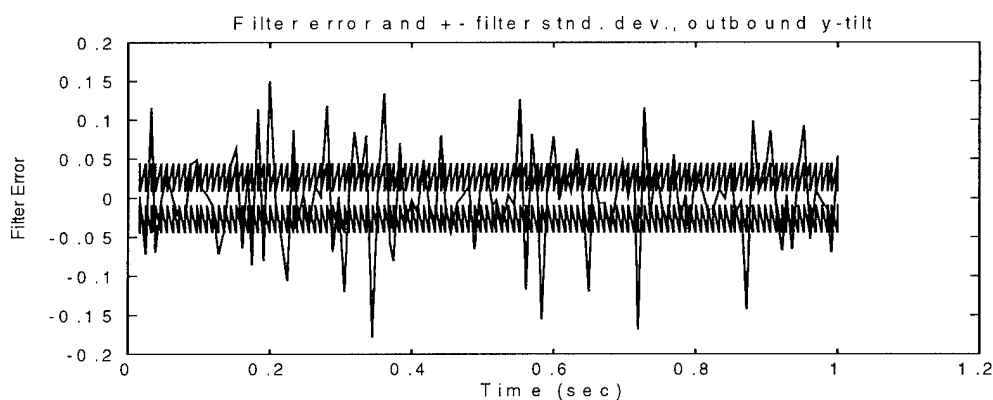
Figure 73. Outbound y-tilt filter error and filter standard deviation.

The mean x-tilt filter error is -0.0003, while the mean y-tilt filter error is 0.00013. The

standard deviation of the x-tilt filter error is 0.07 and the standard deviation of the y-tilt

filter error is 0.045. Recall that these standard deviations were 0.033 (run #2 x-tilt),

0.057 (run #3 x-tilt), 0.018 (run #2 y-tilt), and 0.036 (run #3 y-tilt). Hence, the standard

deviations are larger which implies more uncertainty in the errors.

Outbound x-tilt error: mean and mean +- one stnd. deviation
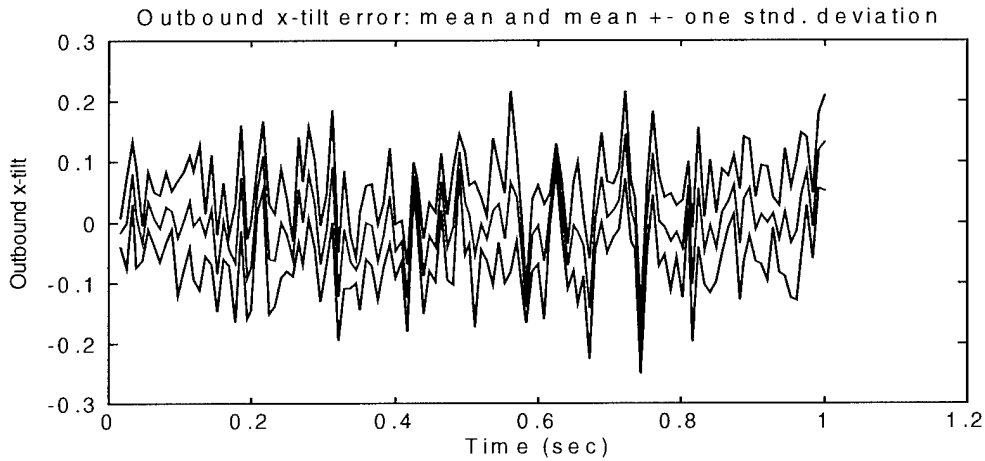
Figure 74. Outbound x-tilt error.

Outbound y-tilt error: mean and mean +- one stnd. deviation
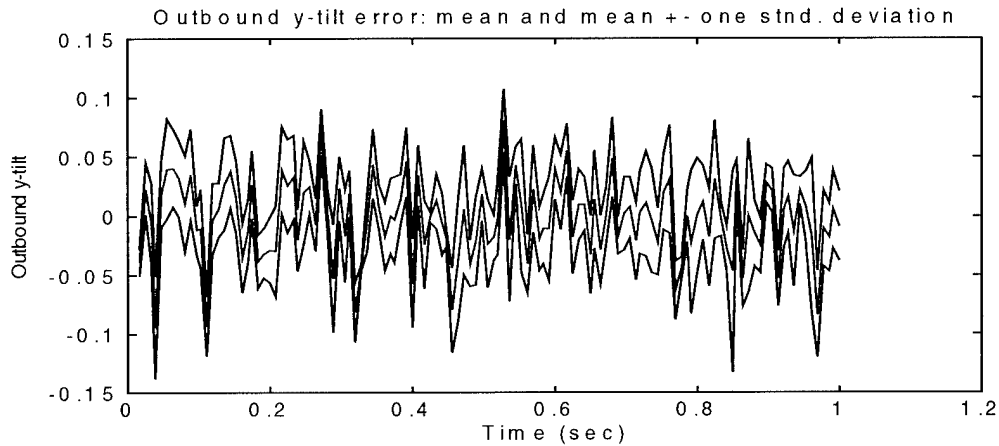
Figure 75. Outbound y-tilt error.

Also, the outbound wavefront tilt errors are much larger than in the previous cases. The

time-averaged standard deviation of the mean x-tilt error is 0.067 and the time-averaged

standard deviation of the mean y-tilt error is 0.038. Previously, these values were 0.03

(run #2 x-tilt), 0.054 (run #3 x-tilt), 0.017 (run #2 y-tilt), and 0.032 (run #3 y-tilt).

Hence, the model inaccuracies are degrading the performance of the controller; however,

the errors are still zero-mean.

Figures 76 and 77 show the mean and mean ± one standard deviation of the

controlled variables. Although the mean and variances have increased from the case

when $Q_a = 10I$, the controlled variables are zero-mean.
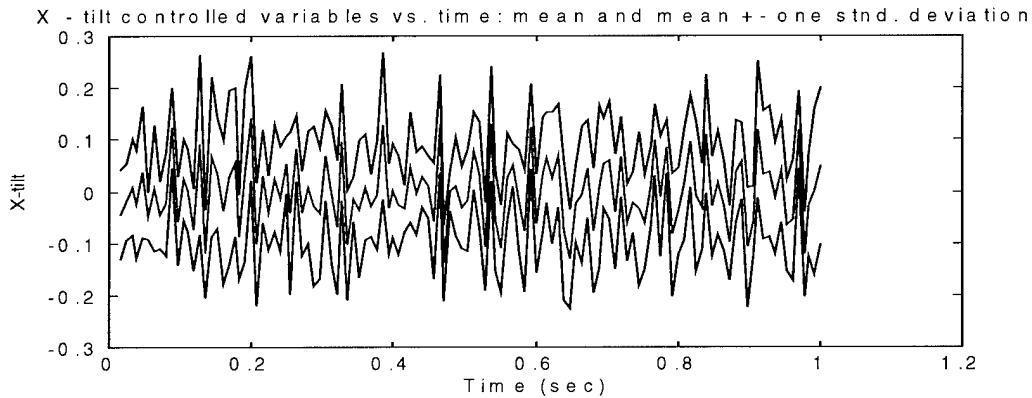
Figure 76. X-tilt controlled variables.
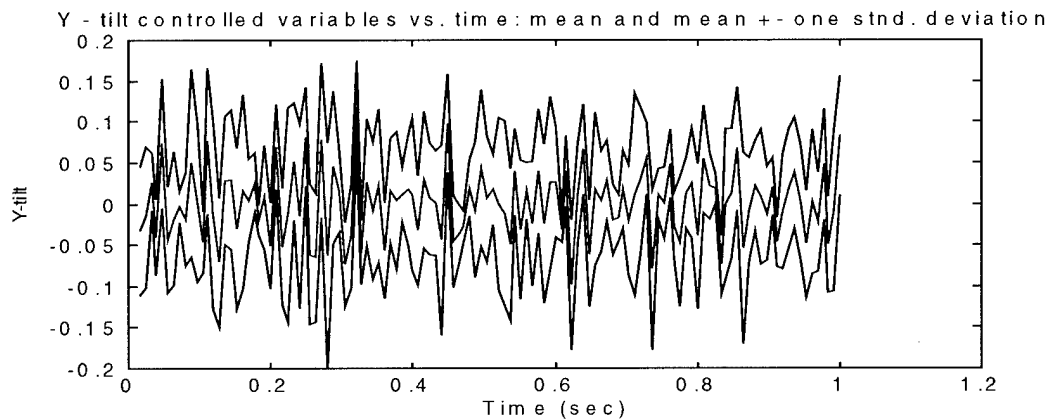
Figure 77. Y-tilt controlled variables.

The standard deviation of the x-tilt controlled variables is 0.064 and for the y-tilt the standard deviation is 0.04. For the last two runs, the standard deviations were 0.027 (run #2 x-tilt), 0.017 (run #2 y-tilt), 0.039 (run #3 x-tilt), and 0.031 (run #3 y-tilt).

Figures 78-80 show the three Strehl ratios. In this case, the compensated Strehl values are about the same as the uncompensated Strehl values. The time-averaged mean uncompensated Strehl ratio is 0.431, while the time-averaged means of the tilt compensation and simple conjugation Strehl ratios are 0.444 and 0.421, respectively. From run #3, the Strehl ratios were 0.495 (tilt compensated) and 0.47 (simple conjugation).

Strehl ratio before compensation: mean and mean +- one stnd. deviation
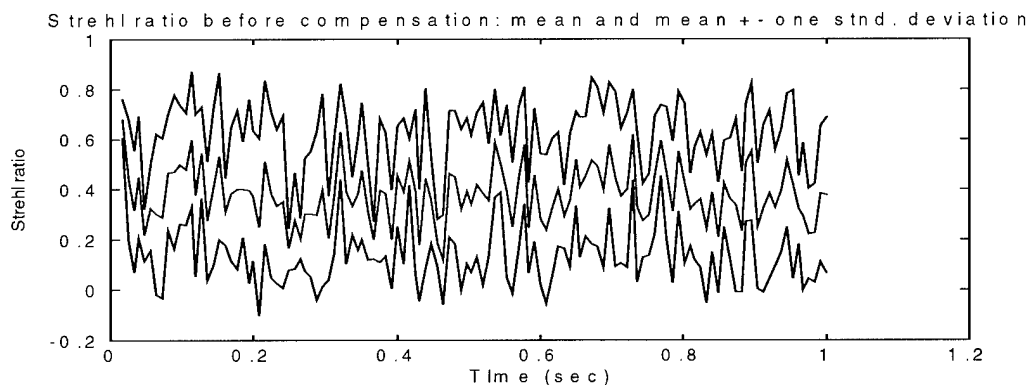
Figure 78. Uncompensated Strehl ratio.

140
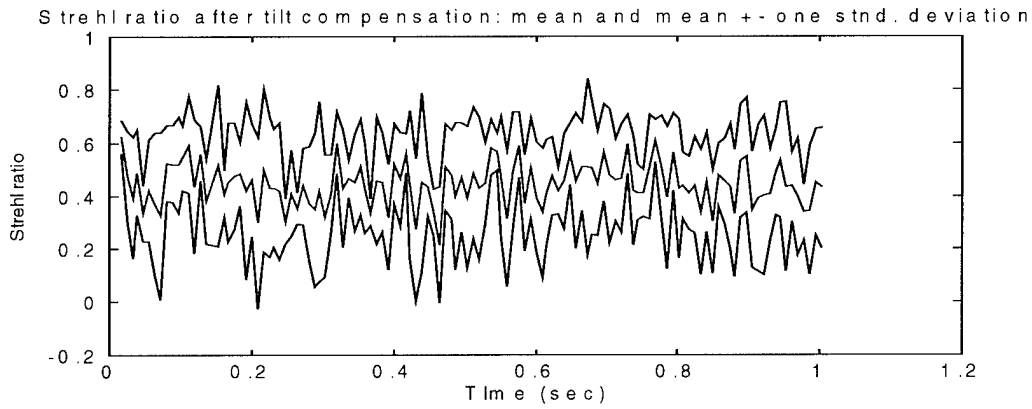
Figure 79. Tilt compensation Strehl ratio.
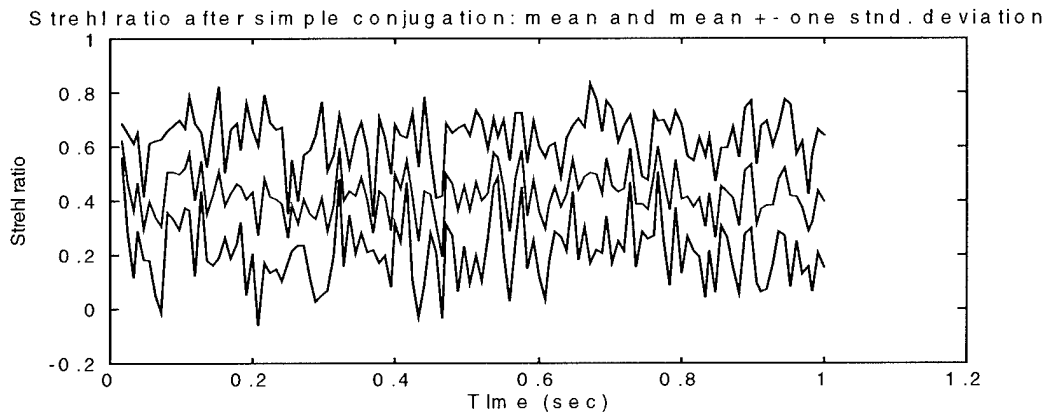
Figure 80. Simple conjugation Strehl ratio.

In conclusion, the severe model inaccuracies investigated in this simulation run do hamper the system's performance. In a number of cases, the filter's errors are large. These have the effect of applying the incorrect phase compensation to the deformable mirror. Hence, at some time instants, the Strehl ratios can actually be less when applying compensation with these model inadequacies. Table 7 displays the results of this simulation run.

141

Figure #	Variable Name	Mean	Std. Deviation
72	X-tilt filter error	-0.0003	0.07
73	Y-tilt filter error	0.00013	0.045
74	Outbound x-tilt	0.00026	0.067
75	Outbound y-tilt	-0.00017	0.038
76	X-tilt controlled variables	-0.00071	0.064
77	Y-tilt controlled variables	-0.00029	0.04
78	Uncompensated Strehl ratio	0.431	---
79	Tilt compensation Strehl ratio	0.444	---
80	Simple phase conjugation Strehl ratio	0.421	---

Table 7. Statistics for run #4 plots.

7.4.5 Simulation Run #5

In this scenario, the actuator time constant was set to 0.75 sec. This simulates a coarse approximation to a time delay. In fact, the delay occurs in the actuation of the DM. Because the time delay only affects actuation of the DM, the only variables that change in this simulation run are the controlled variables, and the ones they affect. That is, the outbound wavefront tilts do not change since they depend only on the performance of the filter. However, Strehl ratios and controlled variables are affected since they require actuation of the DM. Thus, only those plots which change will be shown. For the others, see simulation run #2.

The first plot shown is a single sample realization of the controlled variables.
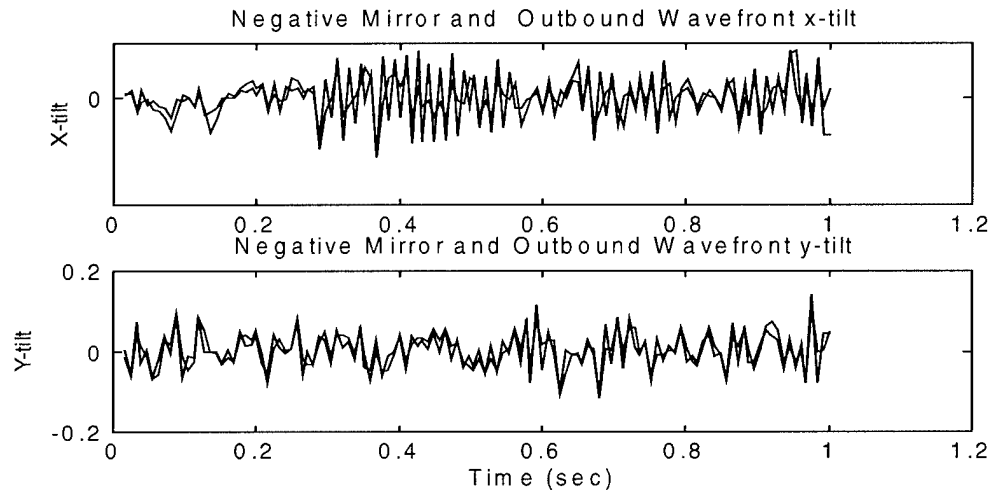
Figure 81. Controlled variables.

It appears that there is much more error in the controlled variables as compared to those

displayed in run #2. Figures 82 and 83 display ensemble statistics of the controlled
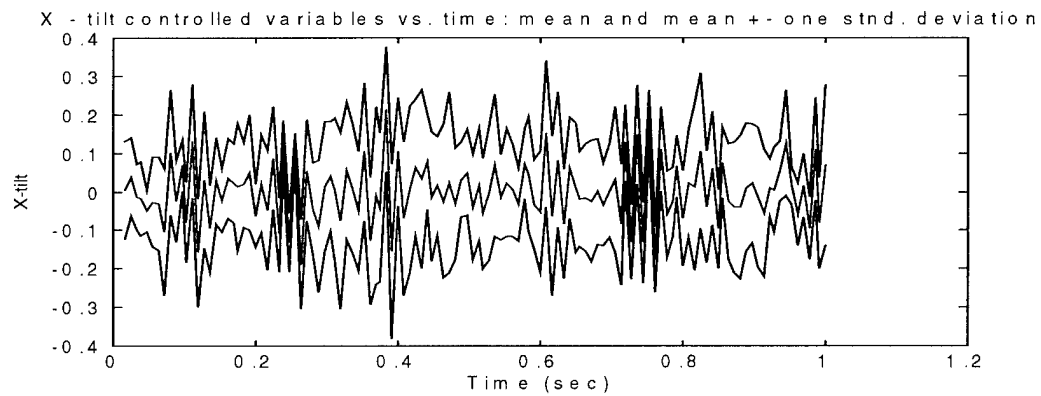
variables.

Figure 82. X-tilt controlled variables.
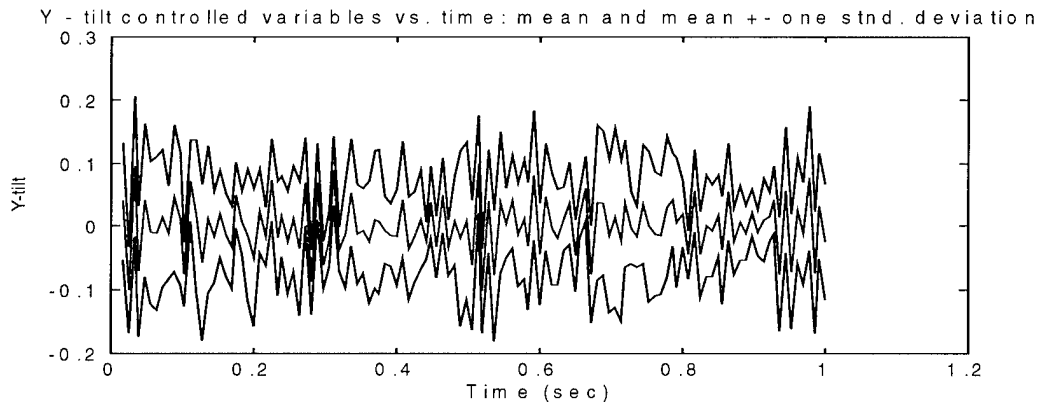
Figure 83. Y-tilt controlled variables.

Here, it can be seen that the variances of the controlled variables are much larger than in

the previous cases. The time-averaged standard deviation of the x-tilt controlled

variables is 0.075 while for the y-tilt the time-averaged standard deviation is 0.046.

Recall that in run #2, the time-averaged standard deviations were 0.027 (x-tilt) and 0.017

(y-tilt). In fact, as will be discussed shortly, applying AO with slow actuators may

actually degrade performance below that which is obtained in the uncompensated

system. To evaluate this statement, ensemble statistics of the Strehl ratios will be

examined. Figures 84-86 show the mean and mean ± one standard deviation of the

Strehl ratios.

144
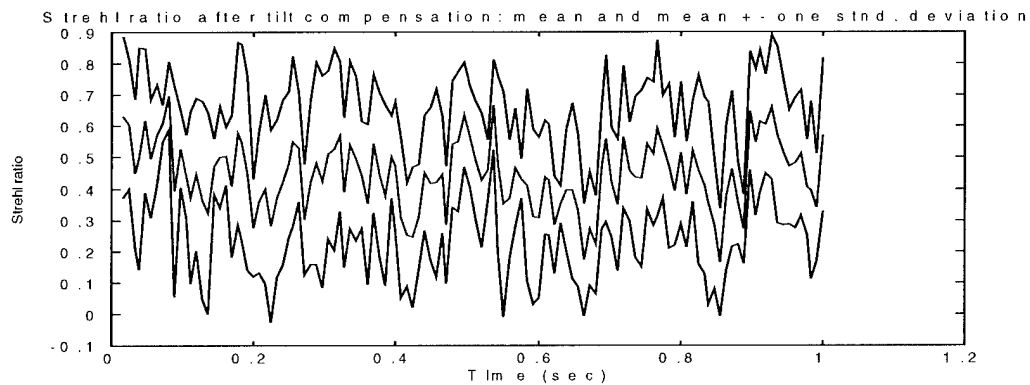
Figure 84. Strehl ratio before compensation.
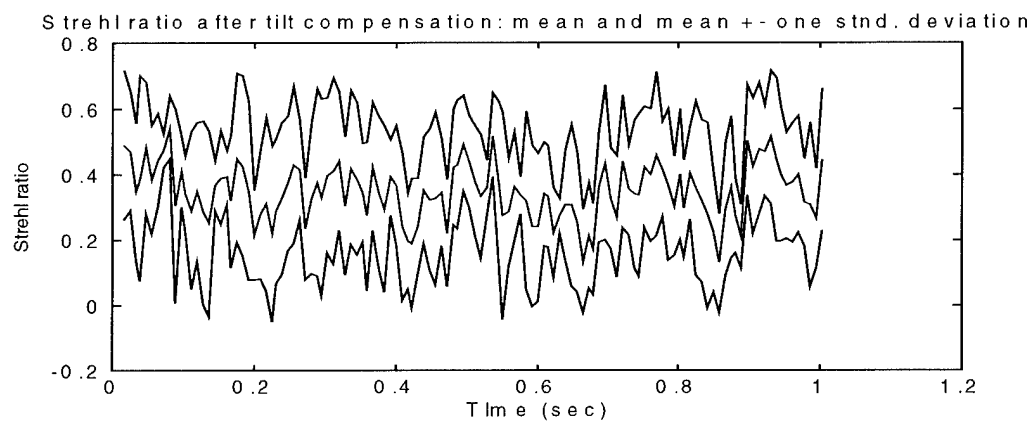
Figure 85. Strehl ratio after tilt compensation.
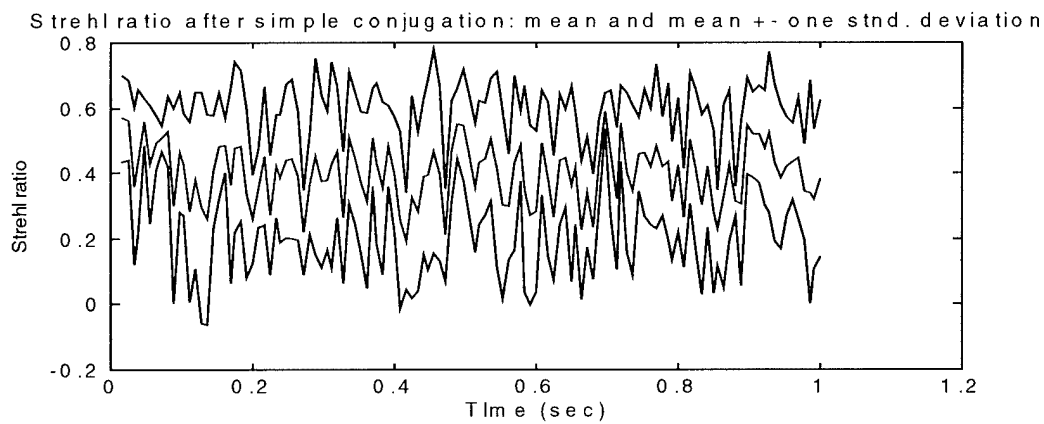
Figure 86. Simple conjugation Strehl ratio.

145

As can be seen in the last three figures, the Strehl ratio, at many time instants, is better in the uncompensated case. The time-averaged mean Strehl ratios are 0.44 (uncompensated), 0.37 (tilt compensation), and 0.39 (simple conjugation). The same information is also displayed in the RMS phase distortion.

In conclusion, with an actuator time constant which is too large, it appears that using AO can degrade system performance. What happens is as follows: measurements are taken and the outbound wave front Zernike coefficients are estimated. However, the estimated conjugate phase is not applied to the DM until a later time because of the actuator delay. Hence, compensation is being calculated for one propagation path while the actual compensation is applied to a different propagation path. In other words, anisoplanatism is not properly taken into account. Thus, with a large actuation delay, system performance can actually be degraded by applying AO. Table 8 shows the statistics of the variables in this simulation run.

Figure #	Variable Name	Mean	Std. Deviation
82	X-tilt controlled variables	-0.00083	0.075
83	Y-tilt controlled variables	-0.00032	0.046
84	Uncompensated Strehl ratio	0.44	---
85	Tilt compensation Strehl ratio	0.37	---
86	Simple phase conjugation Strehl ratio	0.39	---

Table 8. Statistics for run #5 plots.

146

7.5 Summary

In this chapter, the complete AO control system was simulated. A parameter study was performed on the measurement noise variance since it is expected that this value will vary greatly in a practical situation. The process noise strength of the truth model and the actuator time constant were also varied. In all cases, excluding the larger time constant, the controller performs adequately. Hence, accurate estimates of the outbound Zernike coefficients are made and the controlled variables are regulated near zero. With a time delay that is too large, performance can be substantially degraded.

VIII. Conclusions and Recommendations

8.1 Introduction

The principle objective in this research was to establish a unified approach to beam control for the application of AO to the ABL. The objective was motivated by the inadequacy of current analysis methods to address anisoplanatism, the specific ABL engagement geometry, and the correct development of the correlation between inbound and outbound wavefronts. Specifically, this research was intended to assess the effects of anisoplanatism, and to quantify the performance improvements that can be attained by applying tilt compensation to the AO system.

In Chapter 1 of this dissertation, an overview of AO systems and the ABL was presented, along with a historical background, problem statement, and key results. Chapter 2 provided an overview of atmospheric models and Zernike polynomials. The ABL specific engagement geometry was delineated in Chapter 3, including all of the necessary kinematic variable and geometrical relationships. The correlation between inbound and outbound wavefronts was determined in Chapter 4, along with calculations and stochastic modeling. Chapter 5 presented the deformable and complete system models, output equations, and the equivalent discrete-time system. A Kalman filter and LQG controller were constructed in Chapter 6, while simulations were performed in Chapter 7, including a discussion of the simulation results. In the present chapter, the significant advances of this research are summarized and suggestions for future research are offered.

8.2 Significant Advances

This research has led to the following significant advances regarding tilt compensation for the ABL.

- A unified approach to applying tilt compensation to the ABL, which accounts for anisoplanatism and system time delays.

- A fully developed engagement geometry for the ABL encompassing target and aperture motion as well as wind effects.

- A modified frozen flow hypothesis (FFH) which takes into account translation and rotation of the aperture and target.

- A new approach to developing an atmospheric model which directly uses correlation kernel data instead of designing shaping filters for the atmospheric states. This results in a lower-order, and therefore, more practical atmospheric model.

- Atmospheric model developed provides a good representation of the atmosphere. This is validated by examining the performance of the Kalman filter based upon this model and also upon less accurate representations of this model (varying the process noise strength).

- Significant improvement in the reduction of wavefront phase deformations can be obtained by simply performing tilt correction. This result is displayed using simulations of the entire ABL AO control system.

8.3 Summary of Results

The analysis conducted in the dissertation has led to a number of key results. A summary of these results is presented in this section.

- Tilt compensation can significantly improve the ABL's AO system. In terms of Strehl ratios, an improvement of 0.15 was achieved by using tilt compensation as compared to the case in which no compensation was used. In comparison to the simple phase conjugation case, the improvement was smaller, approximately 0.04. However, for a Strehl of 0.5, a 0.04 increase results in a 8% improvement.

- Tilt compensation reduces the RMS phase distortions by about 50%. Therefore, it is clear that tilts are a major factor in wavefront phase deformations.

- The required control system bandwidth for this application is greater than 1 kHz. This is much greater than the bandwidth of current astronomical imaging systems employing AO. The bandwidth requirement increases because the control system must be updated at rates commensurate with the wavefront phase variations.

- A Kalman filter's estimates, with an accurate internal model (plant and deformable mirror), can track the wavefront phase deformations. Therefore, the effects of anisoplanatism can be taken into account and accurate estimates of the outbound wavefront Zernike coefficients can be made.

- The atmospheric model designed in this work is robust to variations of the process noise strength; that is, the Kalman filter can provide reasonable estimates of the outbound wavefront Zernike coefficients.

8.4 Recommendations for Future Research

The research activity in this dissertation provided a description of the design of a control system for beam control in the ABL. While this research answered some important questions, there are many more that go as yet unanswered. There were several considerations that were outside the scope of this work. These issues are outlined in the following paragraphs.

- In this work, a planar engagement geometry was selected. In using this, dynamic motion occurred only in the x-direction. In the future, a full three-dimensional geometry should be investigated, including dynamic motion in both the x- and y-directions.

- Although tilts represent the majority of power in wavefront phase deformations, higher-order modes can be used to capture some of the remaining power. Hence, a model, using more than two Zernike modes, may be useful. However, it should be mentioned once again that more modes implies a higher-order Kalman filter which requires more computation time. Some analysis was conducted using more Zernike modes (5 modes to be precise), but the improvements in performance did not outweigh the additional computational loading.

- The atmospheric model generated here was for one particular engagement geometry and one set of atmospheric parameters. A unified modeling approach would be useful. Perhaps a multiple model type of adaptive estimator [17] could be used. In this case, multiple models would be constructed, one for each entry in a set of

geometrical and atmospheric parameters. Then, using an appropriate probability function, the filter estimates would be weighted to provide the final result.

- A better understanding of the WFS noise model would also be advantageous. Unfortunately, shot noise and photon count, each of which are engagement-specific, represent the majority of sensor noise.

In this section, it is desired to derive eq. (100). Recall, from Chapter 4, eq. (97), that the integral over $\tilde{\theta}$ was given as

$$\text{INT}_{\tilde{\theta}} = \frac{1}{2} \int_{\theta_\alpha}^{\theta_\alpha + 2\pi} e^{-j2\pi|\bar{\bar{\kappa}}_1||\bar{\alpha}|\cos(\tilde{\theta} - \theta_\alpha)} \left[\cos\left\{ (m_f + m_j)\tilde{\theta} + g \right\} + \cos\left\{ (m_f - m_j)\tilde{\theta} + h \right\} \right] d\tilde{\theta} \quad (224)$$

where

$$g = \left\{ \frac{\pi}{4} \left\{ (1 - \delta_{m_i 0})[(-1)^f - 1] + (1 - \delta_{m_j 0})[(-1)^j - 1] \right\} \right\} \quad (225)$$

and

$$h = \left\{ \frac{\pi}{4} \left\{ (1 - \delta_{m_i 0})[(-1)^f - 1] - (1 - \delta_{m_j 0})[(-1)^j - 1] \right\} \right\}. \quad (226)$$

By a change of variables, a trigonometric identity, and the definition for a Bessel function of the first kind [28], denoted by $J_*(\bullet)$, it is stated, in eq. (100), that

$$\text{INT}_{\tilde{\theta}} = \cos\left\{ (m_f + m_j)\theta_\alpha + g \right\} \pi (-1)^{\frac{3(m_f + m_j)}{2}} J_{(m_f + m_j)}\left(2\pi|\bar{\bar{\kappa}}_1||\bar{\alpha}| \right)$$

$$+ \cos\left\{ (m_f - m_j)\theta_\alpha + h \right\} \pi (-1)^{\frac{3(m_f - m_j)}{2}} J_{|m_f - m_j|}\left(2\pi|\bar{\bar{\kappa}}_1||\bar{\alpha}| \right). \quad (227)$$

In order to derive eq. (227), first consider a change of variables: let

$$\beta = \tilde{\theta} - \theta_\alpha \Rightarrow \tilde{\theta} = \beta + \theta_\alpha, \, d\beta = d\tilde{\theta}. \quad (228)$$

Applying this change of variables to eq. (224) gives

$$\text{INT}_{\tilde{\theta}} = \frac{1}{2} \int_0^{2\pi} e^{-j2\pi|\bar{\bar{\kappa}}_1||\bar{\alpha}|\cos\beta} [\bullet] d\beta \quad (229)$$

153

where

$$[\bullet] = \cos\left\{\left(m_f + m_j\right)\beta + \left(m_f + m_j\right)\theta_\alpha + g\right\} + \cos\left\{\left(m_f - m_j\right)\beta + \left(m_f - m_j\right)\theta_\alpha + h\right\}. \quad (230)$$

Considering the first cosine term only, using the identity

$$\cos(a+b) = \cos(a)\cos(b)-\sin(a)\sin(b), \quad (231)$$

and identifying a = $(m_f + m_j)\beta$, b = $(m_f + m_j)\theta\alpha + g$, the term can be rewritten as

$$\cos\left\{\left(m_f + m_j\right)\beta + \left(m_f + m_j\right)\theta_\alpha + g\right\} = \cos\left\{\left(m_f + m_j\right)\beta\right\}\cos\left\{\left(m_f + m_j\right)\theta_\alpha + g\right\}$$

$$-\sin\left\{\left(m_f + m_j\right)\beta\right\}\sin\left\{\left(m_f + m_j\right)\theta_\alpha + g\right\}. \quad (232)$$

Likewise, the second cosine term in eq. (229) can be written as

$$\cos\left\{\left(m_f - m_j\right)\beta + \left(m_f - m_j\right)\theta_\alpha + h\right\} = \cos\left\{\left(m_f - m_j\right)\beta\right\}\cos\left\{\left(m_f - m_j\right)\theta_\alpha + h\right\}$$

$$-\sin\left\{\left(m_f - m_j\right)\beta\right\}\sin\left\{\left(m_f - m_j\right)\theta_\alpha + h\right\}. \quad (233)$$

Therefore, eq. (229) becomes

$$INT_{\tilde{\theta}} = \frac{1}{2}\int_0^{2\pi} e^{-j2\pi\left|\tilde{\kappa}_1\right|\left|\tilde{\alpha}\right|\cos\beta}[\bullet]d\beta \quad (234)$$

where

$$[\bullet] = \cos\left\{\left(m_f + m_j\right)\beta\right\}\cos\left\{\left(m_f + m_j\right)\theta_\alpha + g\right\} - \sin\left\{\left(m_f + m_j\right)\beta\right\}\sin\left\{\left(m_f + m_j\right)\theta_\alpha + g\right\}$$

$$+\cos\left\{\left(m_f - m_j\right)\beta\right\}\cos\left\{\left(m_f - m_j\right)\theta_\alpha + h\right\} - \sin\left\{\left(m_f - m_j\right)\beta\right\}\sin\left\{\left(m_f - m_j\right)\theta_\alpha + h\right\}. \quad (235)$$

Hence, there are four integrals to evaluate. Consider the first integral which is

154

$$INT_{\tilde{\theta} part1} = \frac{1}{2} \int_0^{2\pi} e^{-j2\pi|\bar{\kappa}_1||\bar{\alpha}|\cos\beta} \left[\cos\left\{ \left(m_f + m_j \right)\beta \right\} \cos\left\{ \left(m_f + m_j \right)\theta_\alpha + g \right\} \right] d\beta$$

$$= \frac{1}{2} \cos\left\{ \left(m_f + m_j \right)\theta_\alpha + g \right\} \int_0^{2\pi} e^{-j2\pi|\bar{\kappa}_1||\bar{\alpha}|\cos\beta} \left[\cos\left\{ \left(m_f + m_j \right)\beta \right\} \right] d\beta . \quad (236)$$

From Gradshteyn and Ryzhik [9], a Bessel function can be expressed as

$$J_\lambda(z) = \frac{1}{2\pi(-1)^{3\lambda/2}} \int_0^{2\pi} e^{-jz\cos\beta} \cos(\lambda\beta) d\beta . \quad (237)$$

Identifying $z = 2\pi|\bar{\kappa}_1||\bar{\alpha}|$ and $\lambda = (m_f + m_j)$ and using eq. (237) in eq. (236) produces

$$INT_{\tilde{\theta} part1} = \cos\left\{ \left(m_f + m_j \right)\theta_\alpha + g \right\} \pi(-1)^{3(m_f + m_j)/2} J_{(m_f + m_j)} \left(2\pi|\bar{\kappa}_1||\bar{\alpha}| \right) . \quad (238)$$

Using another formula from Gradshteyn and Ryzhik [9], namely

$$\int_0^{2\pi} e^{-jz\cos\beta} \sin(\lambda\beta) d\beta = 0, \quad (239)$$

it can be seen that the integrals with sine terms are equal to zero. Performing the same procedure for the remaining cosine term in eq. (234) and putting the results together gives the desired final form:

$$INT_{\tilde{\theta}} = \cos\left\{ \left(m_f + m_j \right)\theta_\alpha + g \right\} \pi(-1)^{\frac{3(m_f + m_j)}{2}} J_{(m_f + m_j)} \left(2\pi|\bar{\kappa}_1||\bar{\alpha}| \right)$$

$$+ \cos\left\{ \left(m_f - m_j \right)\theta_\alpha + h \right\} \pi(-1)^{\frac{3(m_f - m_j)}{2}} J_{|m_f - m_j|} \left(2\pi|\bar{\kappa}_1||\bar{\alpha}| \right) \quad (240)$$

which is the same as eq. (100) in Chapter 4.

Appendix B: Evaluation of Discrete-Time System, M and N Matrices, and Derivation of RMS Phase Distortions

In this section, it is desired to evaluate some of the quantities discussed earlier, such as, the equivalent discrete-time system matrices (Section 5.6), **N** matrix (Section 5.5), and the **M** matrix (Section 5.2). Also, the details of deriving eq. (212) will be shown.

B.1 Discrete-Time System Matrices

To begin, consider the equivalent discrete-time system given by eq. (171). In this case, $\Phi(t_{j+1}, t_j)$, $\mathbf{B_d}(t_j)$, and $\mathbf{Q_d}(t_j)$ must be delineated. For the simulations, it has been determined that a sample rate of $t_{j+1} - t_j = 0.0008$ sec. is sufficient. With a constant sample period, evaluation of the discrete-time matrices is much simpler. In the case of $\Phi(t_{j+1}, t_j)$ and $\mathbf{Q_d}(t_j)$, an algorithm specified in Brown and Hwang [2] but developed by van Loan [31] will be used. The algorithm is as follows:

1. Form the matrix

$$\mathbf{A}_{ALG} = \begin{bmatrix} -\mathbf{F} & \mathbf{GG}^T \\ 0 & \mathbf{F}^T \end{bmatrix} \left(t_{j+1} - t_j \right). \tag{241}$$

2. Form $e^{\mathbf{A}_{ALG}}$ using the MATLAB command $expm(\mathbf{A}_{ALG})$ [15], or some other equivalent software tool:

$$\mathbf{B}_{ALG} = \exp m(\mathbf{A}_{ALG}) = \begin{bmatrix} \cdots & \Phi^{-1}\mathbf{Q_d} \\ 0 & \Phi^T \end{bmatrix} \tag{242}$$

where the time instants t_{j+1} and t_j have been eliminated since the sample period is a constant. The upper left partition of $\mathbf{B}_{ALG}$ is of no concern.

3. Transpose the lower right partition of $\mathbf{B}_{ALG}$ to obtain the state-transition matrix.

4. Lastly, $\mathbf{Q_d}$ is obtained as follows:

$$\mathbf{Q_d} = \Phi * (\text{upper right partition of } \mathbf{B}_{ALG}).$$

$\mathbf{B_d}(t_j)$ can be evaluated by solving the following differential equation over each interval $[t_j, t_{j+1})$ [16]:

$$\dot{\overline{\mathbf{B}}}(t,t_j) = \mathbf{F}\overline{\mathbf{B}}(t,t_j) + \mathbf{B}. \tag{243}$$

Equation (243) is integrated forward from $\overline{\mathbf{B}}(t_j,t_j) = \mathbf{0}$ to time t_j to yield

$$\mathbf{B_d}(t_j) = \overline{\mathbf{B}}(t_{j+1},t_j) \quad [16].$$

B.2 Mirror Matrix M

In this section, the matrix $\mathbf{M}$ in eq. (125) will be developed. Recall that $\mathbf{M}$ is

$$\mathbf{M} = \begin{bmatrix} \mathbf{m}_2 & \mathbf{m}_3 & \cdots & \mathbf{m}_{n+1} \end{bmatrix}^T.$$

For the case of x- and y- tilts, $\mathbf{M}$ becomes

$$\mathbf{M} = \begin{bmatrix} \mathbf{m}_2 & \mathbf{m}_3 \end{bmatrix}^T \tag{244}$$

where

$$\mathbf{m}_i^T = \begin{bmatrix} \int W(\overline{x})Z_i(\overline{x})I_1(\overline{x})d\overline{x} & \int W(\overline{x})Z_i(\overline{x})I_2(\overline{x})d\overline{x} & \cdots & \int W(\overline{x})Z_i(\overline{x})I_{n_A}(\overline{x})d\overline{x} \end{bmatrix}. \tag{245}$$

In order to develop this matrix, the influence functions must be specified. There are many different suitable influence functions, i.e., pyramids, cones, etc. A right circular cone will be used in this work. It is suitable for describing influence functions since it tapers off at the radius of influence and has a peak at the center of the actuator. An influence function is displayed in Figure 87, where I_r represents the radius of influence.

INFLUENCE FUNCTION
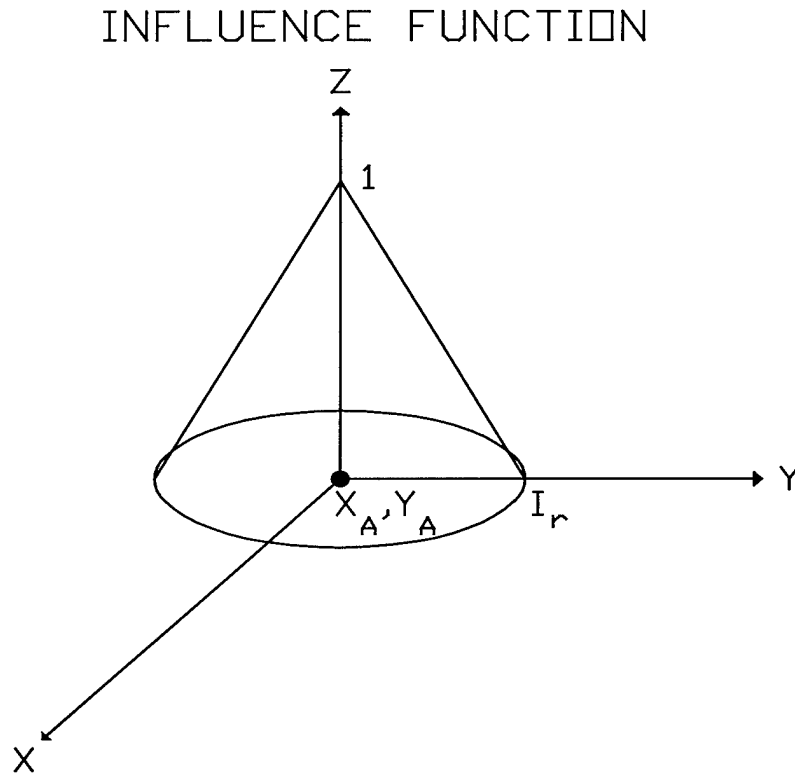
Figure 87. Influence function.

A functional description of the influence function is as follows:

$$I_k(X,Y,X_A,Y_A) = \left[1 - \frac{1}{I_r}\sqrt{(X-X_A)^2 + (Y-Y_A)^2}\right] u\left[I_r^2 - \left\{(X-X_A)^2 + (Y-Y_A)^2\right\}\right] \quad (246)$$

158

where X, Y = spatial location on the mirror, X_A, Y_A = spatial location of an actuator, and

u($\bullet$) is a step function which specifies the domain of each influence function.

In this work, I_r has been chosen equal to the actuator spacing, which implies that

the actuators are independent, i.e., the actuators only effect their particular mirror segment

and do not effect neighboring segments. An actuator map with numbered actuators is

shown in Figure 88. Actuators 1, 7, 43, and 49 are inert while all other actuators are

active.
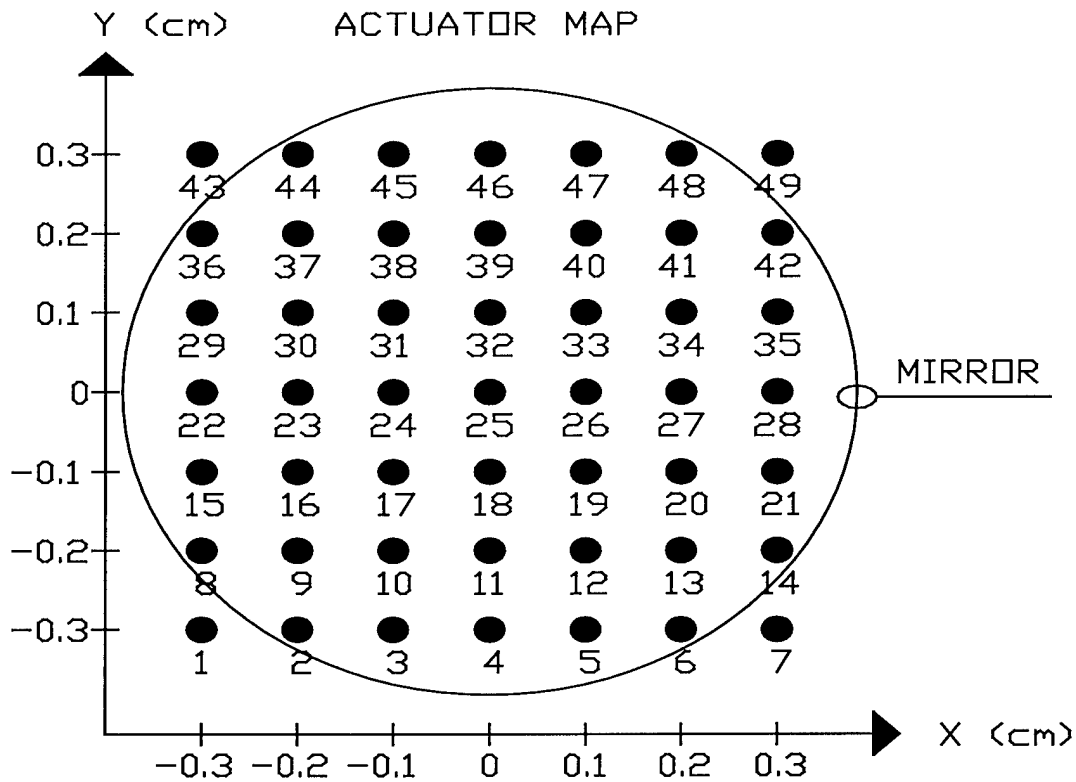
Figure 88. Actuator map.

Considering each term in the vector $\mathbf{m_2}^T$, the following integral is generated by substituting eq. (246) into eq. (245)

$$m_{2j} = \int_{l_y}^{u_y} \int_{l_x}^{u_x} \frac{2x}{\pi R} \left[1 - \frac{1}{I_r} \sqrt{(X - X_A)^2 + (Y - Y_A)^2} \right] dx \, dy \qquad (247)$$

where m_{2j} denotes the jth term in the vector $\mathbf{m_2}^T$ and l_y, u_y, l_x, u_x are the upper and lower limits for the y and x integrations and are determined by the step function in eq. (246). Performing the integration in eq. (247) yields

$$m_{2j} = \frac{1}{\pi R} \left[u_x^2 - l_x^2 \right] \left[u_y - l_y \right] + \frac{4 X_A}{3 R I_r} \left[3 X_A^2 I_r + 3 X_A I_r^2 + I_r^3 \right]. \qquad (248)$$

In the determination of eq. (248), the integrals in eq. (247) were converted to equivalent polar integrals. In doing so, the polar radius was allowed to vary with the spatial location X. Utilizing this fact along with the actuator map in Figure 88, it can be determined that all rows of actuators will have the same m_{2j} terms. Therefore, using an actuator spacing of 0.1 cm gives

$$\begin{aligned} \mathbf{m}_{2\,rep1}^T &= \begin{bmatrix} 0.08909 & 0.02339 & 0.00169 & 0 & -0.00569 & -0.03933 & -0.12509 \end{bmatrix} \\ \mathbf{m}_{2\,rep2}^T &= \begin{bmatrix} 0 & 0.02339 & 0.00169 & 0 & -0.00569 & -0.03933 & 0 \end{bmatrix} \end{aligned} \qquad (249)$$

$$\mathbf{m}_2^T = \frac{1}{R} \begin{bmatrix} \mathbf{m}_{2\,rep2}^T & \mathbf{m}_{2\,rep1}^T & \mathbf{m}_{2\,rep1}^T & \mathbf{m}_{2\,rep1}^T & \mathbf{m}_{2\,rep1}^T & \mathbf{m}_{2\,rep1}^T & \mathbf{m}_{2\,rep2}^T \end{bmatrix} \qquad (250)$$

where $\mathbf{m}_{2\,rep1}^T$ and $\mathbf{m}_{2\,rep2}^T$ represent the repeated entries in the $\mathbf{m_2}^T$ row vector. Using the same type of analysis, $\mathbf{m_3}^T$ becomes

$$
\mathbf{m}_{3\,\mathrm{rep1}} = \begin{bmatrix} 0 \\ 0.02339 \\ 0.00169 \\ 0 \\ -0.00569 \\ -0.03933 \\ 0 \end{bmatrix} \qquad \mathbf{m}_{3\,\mathrm{rep2}} = \begin{bmatrix} 0.08909 \\ 0.02339 \\ 0.00169 \\ 0 \\ -0.00569 \\ -0.03933 \\ -0.12509 \end{bmatrix} \qquad (251)
$$

$$
\mathbf{m}_3^T = \frac{1}{R}\begin{bmatrix} \mathbf{m}_{3\,\mathrm{rep1}}^T & \mathbf{m}_{3\,\mathrm{rep2}}^T & \mathbf{m}_{3\,\mathrm{rep2}}^T & \mathbf{m}_{3\,\mathrm{rep2}}^T & \mathbf{m}_{3\,\mathrm{rep2}}^T & \mathbf{m}_{3\,\mathrm{rep2}}^T & \mathbf{m}_{3\,\mathrm{rep1}}^T \end{bmatrix}. \qquad (252)
$$

B.3 Output Equation Matrix N

Recall from the work in Chapter 5 that $\mathbf{N} = \begin{bmatrix} \mathbf{p}_{x1}\,\mathbf{p}_{x2}\cdots\mathbf{p}_{xp}\,\mathbf{p}_{y1}\,\mathbf{p}_{y2}\cdots\mathbf{p}_{yp} \end{bmatrix}^T$.

Therefore, the vectors $\mathbf{p}_{xj}^T$, $\mathbf{p}_{yj}^T$, $j = 1, 2, \ldots, p$, must be determined, each of which

contain two entries, one for x-tilt and one for y-tilt. In the case of x- and y- tilts only, the

N matrix becomes

$$
\mathbf{N} = \begin{bmatrix} \mathbf{p}_{x1}^T(1) & \mathbf{p}_{x1}^T(2) \\ \mathbf{p}_{x2}^T(1) & \mathbf{p}_{x2}^T(2) \\ \vdots & \vdots \\ \mathbf{p}_{xp}^T(1) & \mathbf{p}_{xp}^T(2) \\ \mathbf{p}_{y1}^T(1) & \mathbf{p}_{y1}^T(2) \\ \mathbf{p}_{y2}^T(1) & \mathbf{p}_{y2}^T(2) \\ \vdots & \vdots \\ \mathbf{p}_{yp}^T(1) & \mathbf{p}_{yp}^T(2) \end{bmatrix} \qquad (253)
$$

where $\mathbf{p}_{xk}^T(1)$ and $\mathbf{p}_{xk}^T(2)$ are the first and second elements in the $\mathbf{p}_{xk}^T$ row vector. From

eq. (157),

$$
\mathbf{p}_x^T(n) = \left[\int_{Y_s-\frac{\sqrt{A}}{2}}^{Y_s+\frac{\sqrt{A}}{2}} \int_{X_s-\frac{\sqrt{A}}{2}}^{X_s+\frac{\sqrt{A}}{2}} W_x(X-X_s, Y-Y_s)\frac{\partial Z_{n+1}(\bar{x})}{\partial Y} \right] dX\,dY\,, n = 1, 2. \qquad (254)
$$

161

Taking the partial derivatives of the Zernike polynomials yields

$$Z_2 = \frac{2X}{R} \Rightarrow \frac{\partial Z_2}{\partial X} = \frac{2}{R}, \frac{\partial Z_2}{\partial Y} = 0$$

$$Z_3 = \frac{2Y}{R} \Rightarrow \frac{\partial Z_3}{\partial X} = 0, \frac{\partial Z_3}{\partial Y} = \frac{2}{R}.$$

(255)

Therefore, it is easily seen that the first entry in each $\mathbf{p}_{xj}^T$ row vector is zero, while the second entry in each $\mathbf{p}_{yj}^T$ is zero. In terms of the other entries, consider first the row vectors $\mathbf{p}_{xj}^T$. The integral in this case becomes

$$\mathbf{p}_x^T(2) = \iint \frac{1}{2\ln 2} \left[2\ln 2 - \left(1 - \frac{2(Y - Y_s)}{\sqrt{A}} \right) \ln \left(1 - \frac{2(Y - Y_s)}{\sqrt{A}} \right) \right.$$

$$\left. - \left(1 + \frac{2(Y - Y_s)}{\sqrt{A}} \right) \ln \left(1 + \frac{2(Y - Y_s)}{\sqrt{A}} \right) \right] \frac{2}{R} dXdY .$$

(256)

Performing the integrations in eq. (256) produces

$$\mathbf{p}_x^T(2) = \frac{2A}{R} \left[1 - \frac{(\ln 2 - 1)}{\ln 2} - \frac{1}{2\ln 2} \right].$$

(257)

It can also be seen that $\mathbf{p}_y^T(1)$ will be exactly the same as the expression in eq. (257).

Hence, the $\mathbf{N}$ matrix becomes

$$N = \begin{bmatrix} \left. \begin{array}{c} 0 \\ 0 \\ \vdots \\ 0 \end{array} \right\}\text{px1} & \left. \begin{array}{c} \dfrac{2A}{R}\left[1-\dfrac{(\ln 2-1)}{\ln 2}-\dfrac{1}{2\ln 2}\right] \\ \dfrac{2A}{R}\left[1-\dfrac{(\ln 2-1)}{\ln 2}-\dfrac{1}{2\ln 2}\right] \\ \vdots \\ \dfrac{2A}{R}\left[1-\dfrac{(\ln 2-1)}{\ln 2}-\dfrac{1}{2\ln 2}\right] \end{array} \right\}\text{px1} \\[2em] \left. \begin{array}{c} \dfrac{2A}{R}\left[1-\dfrac{(\ln 2-1)}{\ln 2}-\dfrac{1}{2\ln 2}\right] \\ \dfrac{2A}{R}\left[1-\dfrac{(\ln 2-1)}{\ln 2}-\dfrac{1}{2\ln 2}\right] \\ \vdots \\ \dfrac{2A}{R}\left[1-\dfrac{(\ln 2-1)}{\ln 2}-\dfrac{1}{2\ln 2}\right] \end{array} \right\}\text{px1} & \left. \begin{array}{c} 0 \\ 0 \\ \vdots \\ 0 \end{array} \right\}\text{px1} \end{bmatrix}. \tag{258}$$

B.4 Derivation of Corrected Wavefront RMS Phase Distortion

In this section, it is desired to derive the expression displayed in eq. (212). Recall that the RMS phase distortion can be expressed as

$$\Phi_{RMS}(t) = \sqrt{W(\bar{x})\Phi^2(\bar{x},t)d\bar{x}}\ . \tag{259}$$

For the corrected wavefront, the expression for the phase becomes

$$\Phi^{(\text{corrected})}(\bar{x},t) = \sum_{j=2}^{n+1} -a_j^{(o)}(t)Z_j(\bar{x}) + \sum_{k=2}^{3} a_k^{(m)}(t)Z_k(\bar{x}) \tag{260}$$

where the negative sign arises because the conjugate phase is being applied to the mirror. Note that both summations start at index two. This is because Zernike number one is piston and is not included in any calculations. Also, only modes two and three, i.e., x- and y-tilts, of the mirror coefficients are included. Even though an accurate

163

representation of the outbound wavefront requires n Zernike modes, only tilts are corrected. Substituting eq. (260) into eq. (259) gives

$$\Phi_{RMS}^{(corrected)}(t) = \sqrt{\int W(\vec{x}) \left[\sum_{j=2}^{n+1} -a_j^{(o)}(t)Z_j(\vec{x}) + \sum_{k=2}^{3} a_k^{(m)}(t)Z_k(\vec{x}) \right]^2 d\vec{x}} \quad . \qquad (261)$$

Expanding the summations produces

$$\Phi_{RMS}^{(corrected)}(t) = \sqrt{\int W(\vec{x}) \left[-a_2^{(o)}(t)Z_2(\vec{x}) - a_3^{(o)}(t)Z_3(\vec{x}) - \cdots - a_{n+1}^{(o)}(t)Z_{n+1}(\vec{x}) + a_2^{(m)}(t)Z_2(\vec{x}) + a_3^{(m)}(t)Z_3(\vec{x}) \right]^2 d\vec{x}} \quad .$$

$$(262)$$

Expanding the term in brackets in eq. (262) yields

$$[\bullet] = \left\{ a_2^{(o)} \right\}^2 Z_2 Z_2 + a_2^{(o)} a_3^{(o)} Z_2 Z_3 + \cdots + a_2^{(o)} a_{n+1}^{(o)} Z_2 Z_{n+1} - a_2^{(o)} a_2^{(m)} Z_2 Z_2 - a_2^{(o)} a_3^{(m)} Z_2 Z_3$$

$$+ a_3^{(o)} a_2^{(o)} Z_3 Z_2 + \left\{ a_3^{(o)} \right\}^2 Z_3 Z_3 + \cdots + a_3^{(o)} a_{n+1}^{(o)} Z_3 Z_{n+1} - a_3^{(o)} a_2^{(m)} Z_3 Z_2 - a_3^{(o)} a_3^{(m)} Z_3 Z_3$$

$$+ \cdots + a_{n+1}^{(o)} a_2^{(o)} Z_{n+1} Z_2 + a_{n+1}^{(o)} a_3^{(o)} Z_{n+1} Z_3 + \cdots + \left\{ a_{n+1}^{(o)} \right\}^2 Z_{n+1} Z_{n+1} - a_{n+1}^{(o)} a_2^{(m)} Z_{n+1} Z_2 - a_{n+1}^{(o)} a_3^{(m)} Z_{n+1} Z_3$$

$$- a_2^{(m)} a_2^{(o)} Z_2 Z_2 - a_2^{(m)} a_3^{(o)} Z_2 Z_3 - \cdots - a_2^{(m)} a_{n+1}^{(o)} Z_2 Z_{n+1} + \left\{ a_2^{(m)} \right\}^2 Z_2 Z_2 + a_2^{(m)} a_3^{(m)} Z_2 Z_3$$

$$- a_3^{(m)} a_2^{(o)} Z_3 Z_2 - a_3^{(m)} a_3^{(o)} Z_3 Z_3 - \cdots - a_3^{(m)} a_{n+1}^{(o)} Z_3 Z_{n+1} + a_3^{(m)} a_2^{(m)} Z_3 Z_2 + \left\{ a_3^{(m)} \right\}^2 Z_3 Z_3 \qquad (263)$$

where Z_j, $j = 2, 3, ..., n+1$ is $Z_j(\vec{x})$. The vector dependence has been dropped to simplify notation. Now, the orthonormality property of the Zernike polynomials can be used. Recall that

$$\int W(\vec{x}) Z_j(\vec{x}) Z_k(\vec{x}) d\vec{x} = \begin{cases} 1 & \text{if } j = k \\ 0 & \text{if } j \neq k. \end{cases} \qquad (264)$$

Substituting eq. (263) into eq. (262) and performing the integration using the property in eq. (264) gives

$$\Phi_{RMS}^{(corrected)}(t) = \sqrt{\left[-a_2^{(o)}(t) + a_2^{(m)}(t)\right]^2 + \left[-a_3^{(o)}(t) + a_3^{(m)}(t)\right]^2 + \left\{a_4^{(o)}(t)\right\}^2 + \cdots + \left\{a_{n+1}^{(o)}(t)\right\}^2} \quad (265)$$

which is the result shown in eq. (212) of Chapter 7.

Bibliography

1. Born, Max and Emil Wolf, *Principles of Optics*, Fourth Edition, New York, Pergamon Press, 1970.

2. Brown, Robert Grover and Patrick Y. C. Hwang, *Introduction to Random Signals and Applied Kalman Filtering*, Third Edition., John Wiley & Sons, 1997.

3. Davenport, Wilbur B. Jr., *Probability and Random Processes: An Introduction for Applied Scientists and Engineers*, McGraw-Hill Book Company, Inc. 1970.

4. Fried, David L., "Optical Resolution Through a Randomly Inhomogeneous Medium for Very Long and Very Short Exposures," *J. Opt. Soc. Am.*, Vol. 56, pp. 1372 - 1379, 1966.

5. Fried, David L., "Anisoplanatism in Adaptive Optics," *J. Opt. Soc. Am.*, Vol. 72, pp. 52 - 61, 1982.

6. Fried, David L., "Statistics of a Geometric Representation of Wavefront Distortion," *J. Opt. Soc. Am.*, Vol. 55, No. 11, pp. 1427 - 1435, November 1965.

7. Gaskill, Jack D., *Linear Systems, Fourier Transforms, and Optics*, John Wiley & Sons, 1978.

8. Goodman, J. W., *Statistical Optics*, New York, John Wiley and Sons, 1985.

9. Gradshteyn, I. S. and I. M. Ryzhik, *Tables of Integrals, Series, and Products*, Academic Press, Fifth Edition, 1994.

10. Greenwood, D. P., "Bandwidth Specifications for Adaptive Optics Systems," *J. Opt. Soc. Am.*, Vol. 67, pp. 390 - 392, 1977.

11. Hardy, J. W., "Active Optics: A new technology for the control of light," *Proc. IEEE*, Vol. 66, pp. 651 - 687, 1978.

12. Hogge, C. Barry and R. Russell Butts, "Frequency Spectra for the Geometric Representation of Wavefront Distortions Due to Atmospheric Turbulence," *IEEE Trans. on Antennas and Propagation*, Vol. AP-24, No. 2, pp. 144 - 154, March 1976.

13. Ishimaru, A., *Wave Propagation and Scattering in Random Media*, Vol. 2, New York, Academic Press, 1978.

14.   Kolmogorov, A. N., "The Local Structure of Turbulence in Incompressible Viscous Fluids for Very Large Reynolds' Numbers," in *Turbulence, Classic Papers on Statistical Theory*, New York: Wiley-Interscience, pp. 151 - 155, 1961.

15.   MathWorks, Inc., *MATLAB: High-Performance Numeric Computation and Visualization Software*, 1993.

16.   Maybeck, Peter S., *Stochastic Models, Estimation, and Control Volume 1*, Academic Press, 1979.

17.   Maybeck, Peter S., *Stochastic Models, Estimation, and Control Volume 3*, Academic Press, 1982.

18.   Noll, Robert J., "Zernike Polynomials and Atmospheric Turbulence," *J. Opt. Soc. Am.*, Vol. 66, No. 3, pp. 207 - 211, March 1976,

19.   Oppenheimer, Michael and Meir Pachter, "Algorithm Development for On-Line Control of the ABL," in *Proceedings of the SPIE*, Vol. 3706, pp. 349 - 360, April 1999.

20.   Oppenheimer, Michael and Meir Pachter, "Correlation Function Synthesis for On-Line Control of the AirBorne Laser," in *Proceedings of the SPIE*, Vol. 3381, pp. 88 - 97, April 1998.

21.   Parenti, R. R. and R. J. Sasiella, "Laser-Guide-Star Systems for Astronomical Applications," *J. Opt. Soc. Am. A*, Vol. 11, pp. 288 - 309, 1994.

22.   Peterson, Daniel P. and K. H. Cho, Sampling and Reconstruction of a Turbulence-Distorted Wave Front," *J. Opt. Soc. Am. A*, Vol. 3, pp. 816 - 825, June 1986.

23.   Roggeman, Michael C. and Byron Welsh, *Imaging Through Turbulence*, CRC Press, 1996.

24.   Southwell, W. H., "Wave-Front Estimation from Wave-Front Slope Measurements," *J. Opt. Soc. Am.*, Vol. 70, pp. 998 - 1006, August 1980.

25.   Strohbehn, John W., "Optical Propagation Through the Turbulent Atmosphere," in *Progress in Optics*, Vol. IX, North-Holland Publishing Company, pp. 75-122, 1971.

26.   Takato, Naruhisa and Ichirou Yamaguchi, "Spatial Correlation of Zernike Phase-Expansion Coefficients for Atmospheric Turbulence with Finite Outer Scale," *J. Opt. Soc. Am. A*, Vol. 12, No. 5, pp. 958 - 963, May 1995.

27.   Tatarski, V. I., *Wave Propagation in a Turbulent Medium*, McGraw-Hill Book Company, 1961.

28.   Tatarski, V. I. and V. U. Zavorotnyi, "Strong Fluctuations in Light Propagation in a Randomly Inhomogeneous Medium,"in *Progress in Optics*, Vol. XVIII, North-Holland Publishing Company, pp. 207 - 256, 1980.

29.   Troxel, S. E., B. M. Welsh, and M. C. Roggemann, "Off-Axis Optical Transfer Function Calculations in an Adaptive Optics System by Means of a Diffraction Calculation for Weak Index Fluctuations," *J. Opt. Soc. Am. A*, Vol. 11, pp. 2100 - 2111, 1994.

30.   Valley, George C. and Stephen M. Wandzura, "Spatial Correlation of Phase-Expansion Coefficients for Propagation through Atmospheric Turbulence," *J. Opt. Soc. Am.*, Vol. 69, No. 5, pp. 712 - 717, May 1979.

31.   Van Loan, C. F., "Computing Integrals Involving the Matrix Exponential," *IEEE Trans. on Automatic Control*, Vol. AC-23:3, pp. 395 - 404, June 1978.

32.   Von Bokern, Mark Alan, Randall N. Paschall, and Byron M. Welsh, "Modal Control for an Adaptive Optics System Using LQG Compensation," *Computers Elect. Engng.*, Vol. 18, No. 6, pp. 421 - 433, 1992.

33.   Von Bokern, Mark Alan, *Design of a Linear Quadratic Gaussian Control Law for an Adaptive Optics System*, MS Thesis, AFIT/GE/ENG/90D-65, School of Engineering, The Air Force Institute of Technology, Wright-Patterson AFB, OH, December 1990.

34.   Wang, J. Y. and J. K. Markey, "Modal Compensation of Atmospheric Turbulence Phase Distortion," *J. Opt. Soc. Am.*, Vol. 68, pp. 78 - 87, January 1978.

35.   Whiteley, Matthew R., Michael C. Roggemann, and Byron M. Welsh, "Temporal Properties of the Zernike Expansion Coefficients of Turbulence-Induced Phase Aberrations for Aperture and Source Motion," *J. Opt. Soc. Am. A*, Vol. 15, No. 4, April 1998.

36.   Whitely, Matthew R., Optimal Atmospheric Compensation for Anisoplanatism in Adaptive-Optical Systems, Dissertation, AFIT/DS/ENP/98-01, School of Engineering, The Air Force Institute of Technology, Wright-Patterson AFB, OH, September 1998.

37.   Young, A. T., "Seeing: Its Cause and Cure," *Astrophys. J.*, Vol. 189, pp. 587 - 604, 1974.

Vita

Michael W. Oppenheimer was born on August 30, 1971 in Warren, Ohio. He graduated from Howland High School in 1989. Oppenheimer then attended the University of Akron in Akron, Ohio where he received a B. S. in Electrical Engineering. Upon graduation, he enrolled in the graduate school of engineering at the University of Akron. In August 1996, Oppenheimer received a M. S. in Electrical Engineering. In September 1996, he accepted a DAGSI scholarship to attend AFIT. Oppenheimer will continue his engineering research in the private sector.

Permanent address: 1347 Lamplighter Lane
                     Fairborn, OH 45324

REPORT DOCUMENTATION PAGE		Form Approved OMB No. 074-0188

The public reporting burden for this collection of information is estimated to average 1 hour per response, including the time for reviewing instructions, searching existing data sources, gathering and maintaining the data needed, and completing and reviewing the collection of information. Send comments regarding this burden estimate or any other aspect of the collection of information, including suggestions for reducing this burden to Department of Defense, Washington Headquarters Services, Directorate for Information Operations and Reports (0704-0188), 1215 Jefferson Davis Highway, Suite 1204, Arlington, VA 22202-4302. Respondents should be aware that notwithstanding any other provision of law, no person shall be subject to an penalty for failing to comply with a collection of information if it does not display a currently valid OMB control number.
PLEASE DO NOT RETURN YOUR FORM TO THE ABOVE ADDRESS.

1. REPORT DATE (DD-MM-YYYY) 06-09-2000	2. REPORT TYPE Doctoral Dissertation	3. DATES COVERED (From – To) Jun 1998 – Sep 2000

4. TITLE AND SUBTITLE ALGORITHM DEVELOPMENT FOR ON-LINE CONTORL OF THE AIRBORNE LASER	5a. CONTRACT NUMBER DOC # 00-114
	5b. GRANT NUMBER MORD # ORCMORD00710175
	5c. PROGRAM ELEMENT NUMBER
6. AUTHOR(S) Oppenheimer, Michael W., DAGSI	5d. PROJECT NUMBER ENR # 00-36
	5e. TASK NUMBER
	5f. WORK UNIT NUMBER

7. PERFORMING ORGANIZATION NAMES(S) AND ADDRESS(S) Air Force Institute of Technology Graduate School of Engineering and Management (AFIT/EN) 2950 P Street, Building 640 WPAFB OH 45433-7765	8. PERFORMING ORGANIZATION REPORT NUMBER AFIT/DS/ENG/00-02

9. SPONSORING/MONITORING AGENCY NAME(S) AND ADDRESS(ES) AFRL/DEBA Attn: Ms. Judith Miller 3550 Aberdeen St. SE Kirtland AFB, NM 87117-5776 DSN: 246-1539	10. SPONSOR/MONITOR'S ACRONYM(S) AFRL/DE
	11. SPONSOR/MONITOR'S REPORT NUMBER(S) DOC # QAFRL 006202003

12. DISTRIBUTION/AVAILABILITY STATEMENT

APPROVED FOR PUBLIC RELEASE; DISTRIBUTION UNLIMITED.

13. SUPPLEMENTARY NOTES

14. ABSTRACT

The use of adaptive optics entails the design of a controller. This requires the development of a model of the plant to be controlled, which, in this case, consists of the atmosphere through which light is traveling. In optics, Zernike polynomials are used as a basis set for the expansion of wavefront phase distortions. Due to the turbulence induced stochastic nature of the underlying process involved, the spatial-temporal correlation functions of the Zernike polynomial phase expansion coefficients must be evaluated if a proper stochastic model of the plant is to be developed and adaptive optics is to be employed. In this work, these correlation functions are developed using a layered atmospheric model which takes into account wind effects and anisoplanatism. Calculations are provided for the first few low-order Zernike modes. Using these correlation functions, an underlying linear, stochastic, dynamical system, which represents the atmosphere and is adequate for control synthesis, is identified. Within an acceptable error bound, the correlation functions of this system are representative of the calculated functions. The deformable mirror is also modeled, output equations are specified, and the complete system is constructed. This system, in turn, provides the basis for the employment of advanced control and estimation concepts. The control objective is to apply the estimated conjugate phase to the deformable mirror so that, at the target, the outbound wavefront distortion is minimized and the Strehl ratio is maximized.

15. SUBJECT TERMS
AirBorne Laser, Adaptive Optics, Tilt Compensation, Zernike Polynomials, Kalman Filtering, Linear Quadratic Gaussian Control, Correlation, Layered Atmospheric Model, Atmospheric Turbulence, Anisoplanatism

16. SECURITY CLASSIFICATION OF:			17. LIMITATION OF ABSTRACT	18. NUMBER OF PAGES	19a. NAME OF RESPONSIBLE PERSON Prof. Meir Pachter, ENG
a. REPORT U	b. ABSTRACT U	c. THIS PAGE U	UU	195	19b. TELEPHONE NUMBER (Include area code) (937) 255-3636, ext 4593

Standard Form 298 (Rev. 8-98)
Prescribed by ANSI Std. Z39-18

	Form Approved OMB No. 074-0188